PSI TR-358

FINAL TECHNICAL REPORT

STUDIES OF A REPETITIVELY-PULSED LASER POWERED THRUSTER

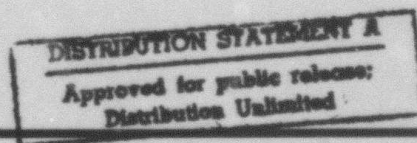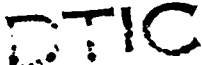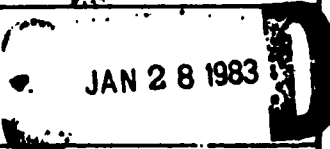|	
DARPA ORDER NO:	3176
CONTRACTOR:	PHYSICAL SCIENCES INC.
EFFECTIVE DATE OF CONTRACT:	18 January 1982
CONTRACT EXPIRATION DATE:	18 August 1982
REPORTING PERIOD:	18 January 1982 – 18 August 1982
CONTRACT NO:	N00014-82-C-0165
PRINCIPAL INVESTIGATOR:	Dr. David I. Rosen (617) 475-9030

DTIC

JAN 2 8 1983

H

PHYSICAL SCIENCES INC.

RESEARCH PARK, ANDOVER, MA 01810

83 01 28 035

DTIC FILE COPY

AD A123938

SECURITY CLASSIFICATION OF THIS PAGE (When Data Entered)

REPORT DOCUMENTATION PAGE	READ INSTRUCTIONS BEFORE COMPLETING FORM

1. REPORT NUMBER	2. GOVT ACCESSION NO. AD-A123938	3. RECIPIENT'S CATALOG NUMBER

4. TITLE (and Subtitle)	5. TYPE OF REPORT & PERIOD COVERED
Studies of a Repetitively-Pulsed Laser Powered Thruster	Final Technical Report 18 January 1982-18 Aug 1982
	6. PERFORMING ORG. REPORT NUMBER TR-358

7. AUTHOR(s)	8. CONTRACT OR GRANT NUMBER(s)
D. I. Rosen; N. H. Kemp; and M. Miller	N00014-82-C-0165

9. PERFORMING ORGANIZATION NAME AND ADDRESS	10. PROGRAM ELEMENT, PROJECT, TASK AREA & WORK UNIT NUMBERS
Physical Sciences Inc. Research Park, Andover, MA 01810	DARPA Order No 3176

11. CONTROLLING OFFICE NAME AND ADDRESS	12. REPORT DATE
Defense Advanced Research Projects Agency Directed Energy Office 1400 Wilson Blvd. Arlington, VA 22209	January 1982
	13. NUMBER OF PAGES 94

14. MONITORING AGENCY NAME & ADDRESS(If different from Controlling Office)	15. SECURITY CLASS. (of this report)
Office of Naval Research, Dept. of the Navy 800 N. Quincy Street Arlington, VA 22217	Unclassified
	15a. DECLASSIFICATION/DOWNGRADING SCHEDULE

16. DISTRIBUTION STATEMENT (of this Report)

Unlimited Distribution

17. DISTRIBUTION STATEMENT (of the abstract entered in Block 20, if different from Report)

DTIC

JAN 2 8 1983

H

18. SUPPLEMENTARY NOTES

19. KEY WORDS (Continue on reverse side if necessary and identify by block number)

Pulsed Laser Propulsion   Non-steady Nozzle Flow
Pulse-Jets   Specific Impulse
Laser-Supported Detonation Waves

20. ABSTRACT (Continue on reverse side if necessary and identify by block number)

In this report we present results of continuing analytical and experimental investigations carried out to evaluate the concept of pulsed laser propulsion. This advanced propulsion scheme, which has been the subject of several previous studies, involves supplying propellant energy by beaming short, repetitive laser pulses to a thruster from a remote laser power station. The concept offers the advantages of a remote power source, high specific impulse, high payload to total mass ratio (a consequence of the

DD FORM 1 JAN 73 1473   EDITION OF 1 NOV 65 IS OBSOLETE

i

first two features) and moderate to high thrust (limited primarily by the average laser power available). The present research addresses questions related to thruster performance and optical design.

In the thruster scheme under consideration, parabolic nozzle walls focus the incoming laser beam to yield breakdown in a propellant at the focal point of the parabola. The resulting high pressure plasma is characteristic of a detonation wave initiation by high power laser-induced breakdown. With a short laser pulse, the detonation wave quickly becomes a blast wave which propagates to the nozzle exit plane converting the high pressure of the gas behind it to a force on the nozzle wall. Propellant is fed to the focal region from a plenum chamber. The laser-induced blast wave stops the propellant flow through the throat until the pressure at the throat decays to the sonic pressure; then the propellant flow restarts. The process is repeated with each successive laser pulse.

A major part of the present work involved carrying out thruster performance experiments using a small scale conical nozzle, external focusing optics, and pulsed CO_2 ($\lambda=10.6$ μm) and pulsed XeF ($\lambda=0.35$ μm) lasers as the propellant heating sources. All experiments were performed in a vacuum environment. With the XeF laser ($E_p=2.7$ J, $\tau_p=0.6$ μs) and argon propellant, a maximum specific impulse of 500 seconds was achieved with a conversion efficiency of laser energy to propellant kinetic energy upwards of 50%. With the same propellant and the CO_2 TEA laser ($E_p\approx6.5$ J, $\tau_p\approx3$ μ μs), the maximum specific impulse was 700 seconds with a laser to kinetic energy conversion efficiency $\approx$ 20%. Finally, using hydrogen propellant and the CO_2 laser as the heating source, the experimental data indicate specific impulse up to 3000 seconds with corresponding energy conversion efficiencies upwards of $\approx$ 70%.

In support of the thruster performance experiments, a detailed computer model that was developed previously was modified and used to simulate the nozzle fluid dynamics in the conical thruster. The model treats non-steady nozzle flow of a real gas with laser heat addition. Major emphasis in the present work was directed toward simulating the fluid dynamics appropriate for repetitively-pulsed operation, i.e., the situation in which the nozzle has only partly refilled with fresh gas between successive laser pulses and the remaining downstream section of the nozzle contains the low pressure tail of the previous blast wave. For a given initial propellant mass distribution and laser input, the computer program calculates such quantities as the exhaust gas momentum, kinetic energy, and specific impulse.

Finally, an assessment has been made of optical design criteria for a self-focusing paraboloidal nozzle. The primary conclusions reached are: (1) the mission requirements for off-axis performance allow the surface to be of only very modest optical quality, (2) for off-axis angles $\gtrsim 10°$, only very modest magnifications ($\lesssim 25$) can be anticipated, (3) optimum optical and fluid dynamic performance appear to be mutually inclusive, consequently, a compromise is required, and (4) the impact of off-axis focusing and breakdown on thruster performance should be evaluated.

ABSTRACT

In this report we present results of continuing analytical and experimental investigations carried out to evaluate the concept of pulsed laser propulsion. This advanced propulsion scheme, which has been the subject of several previous studies, involves supplying propellant energy by beaming short, repetitive laser pulses to a thruster from a remote laser power station. The concept offers the advantages of a remote power source, high specific impulse, high payload to total mass ratio (a consequence of the first two features) and moderate to high thrust (limited primarily by the average laser power available). The present research addresses questions related to thruster performance and optical design.

In the thruster scheme under consideration, parabolic nozzle walls focus the incoming laser beam to yield breakdown in a propellant at the focal point of the parabola. The resulting high pressure plasma is characteristic of a detonation wave initiation by high power laser-induced breakdown. With a short laser pulse, the detonation wave quickly becomes a blast wave which propagates to the nozzle exit plane converting the high pressure of the gas behind it to a force on the nozzle wall. Propellant is fed to the focal region from a plenum chamber. The laser-induced blast wave stops the propellant flow through the throat until the pressure at the throat decays to the sonic pressure; then the propellant flow restarts. The process is repeated with each successive laser pulse.

A major part of the present work involved carrying out thruster performance experiments using a small scale conical nozzle, external focusing optics, and pulsed CO_2 ($\lambda=10.6$ μm) and pulsed XeF ($\lambda=0.35$ μm) lasers as the propellant heating sources. All experiments were performed in a vacuum environment. With the XeF laser ($E_p=2.7$ J, $\tau_p=0.6$ μs) and argon propellant, a maximum specific impulse of 500 seconds was achieved with a conversion efficiency of laser energy to propellant kinetic energy upwards of 50%. With the same propellant and the CO_2 TEA laser ($E_p \approx 6.5$ J, $\tau_p \approx 3$ μs), the maximum specific impulse was 700 seconds with a laser to kinetic energy conversion efficiency $\approx 20\%$. Finally, using hydrogen propellant and the CO_2 laser as the heating

source, the experimental data indicate specific impulse up to 3000 seconds with corresponding energy conversion efficiencies upwards of ≈ 70%.

In support of the thruster performance experiments, a detailed computer model that was developed previously was modified and used to simulate the nozzle fluid dynamics in the conical thruster. The model treats non-steady nozzle flow of a real gas with laser heat addition. Major emphasis in the present work was directed toward simulating the fluid dynamics appropriate for repetitively-pulsed operation, i.e., the situation in which the nozzle has only partly refilled with fresh gas between successive laser pulses and the remaining downstream section of the nozzle contains the low pressure tail of the previous blast wave. For a given initial propellant mass distribution and laser input, the computer program calculates such quantities as the exhaust gas momentum, kinetic energy, and specific impulse.

Finally, an assessment has been made of optical design criteria for a self-focusing paraboloidal nozzle. The primary conclusions reached are: (1) the mission requirements for off-axis performance allow the surface to be of only very modest optical quality, (2) for off-axis angles $\gtrsim 10°$, only very modest magnifications ($\lesssim 25$) can be anticipated, (3) optimum optical and fluid dynamic performance appear to be mutually inclusive, consequently, a compromise is required, and (4) the impact of off-axis focusing and breakdown on thruster performance should be evaluated.

TABLE OF CONTENTS

LIST OF ILLUSTRATIONS

LIST OF ILLUSTRATIONS (CONT.)

LIST OF TABLES

1. INTRODUCTION AND EXECUTIVE SUMMARY

Repetitively-pulsed (RP) laser propulsion is a pulsed jet propulsion concept in which the propellant energy is supplied by the absorption of short, repetitive laser pulses beamed to the thruster from a remote laser power station. This advanced propulsion concept offers the advantages of a remote power source, high specific impulse, high payload to total mass ratio (a consequence of the first two features), and moderate to high thrust (limited primarily by the average laser power available).

In the RP thruster concept shown in Fig. 1.1, parabolic nozzle walls focus the incoming beam to yield breakdown in a propellant at the focal point of the parabola. The resulting high pressure plasma is characteristic of detonation wave intiation by high power laser-induced breakdown. With a short laser pulse, the detonation wave quickly becomes a blast wave, which propagates to the nozzle exit plane converting the high pressure of the propellant gas behind it into a force on the nozzle wall. Propellant is fed to the focal region from a plenum chamber. The laser-induced blast wave stops the propellant flow through the throat until the pressure at the throat decays to the sonic pressure; then, the propellant flow restarts. The process is repeated with each successive laser pulse.

Physical Sciences Inc. (PSI) has been developing the technology of pulsed laser propulsion under DARPA support.[1.1-1.4] Previous experiments and supporting theoretical studies have shown that repetitively pulsed 10.6 μm laser radiation can be utilized to heat simple propellants to high stagnation temperatures; the result is rocket propulsion at high specific impulse (I_{sp}). Using a simple thruster concept (similar to the one shown in Fig. 1.1) with a variety of propellants, we obtained specific impulses of up to 1000 s with an energy conversion efficiency of 40%. PSI has since been engaged in utilizing the knowledge and experience obtained from this program to advance laser propulsion technology for DARPA space applications. Since laser propulsion activities are driven by advances in laser technology for other applications in space, it has been proposed that pulsed laser propulsion systems utilize visible/UV pulsed lasers. Therefore, the recent program objectives have been to

1

ALUMINUM PARABOLIC SHELL
OF REVOLUTION

LASER
BEAM

POLISHED
SURFACE

BLAST WAVE

FOCAL
POINT

LASER
INDUCED
BREAKDOWN

PROPELLANT
PLENUM

COLD
PROPELLANT
FLOW
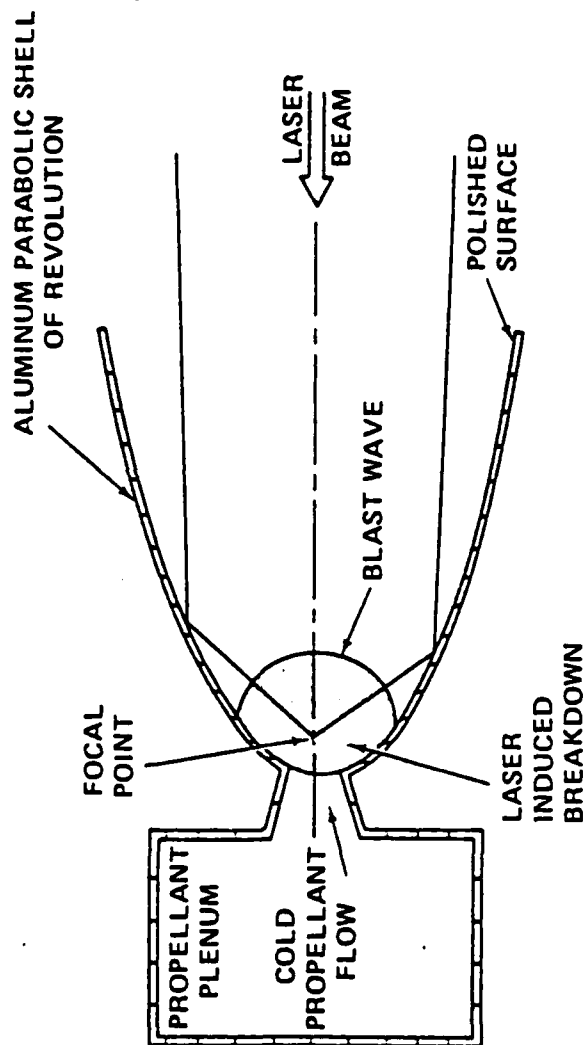
● PROPULSION SEQUENCE

– COLD PROPELLANT FLOWS THROUGH THROAT

– LASER ENERGY ABSORBED VIA INVERSE BREMSSTRAHLUNG
DOWNSTREAM AT FOCUS

– SHOCKED GAS EXPANDS OUT NOZZLE

– SEQUENCE REPEATS: PROPELLANT USE CONTROLLED BY MASS FLOW
AND LASER REPETITION RATE

Fig. 1.1   Schematic of repetitively pulsed laser-powered thruster.

2

1) establish missions and associated laser requirements for a ground based laser propulsion system, 2) establish a thruster design capability for efficient performance as a function of desired specific impulse and laser wavelength, 3) develop scaling laws for laser propulsion with pulsed visible lasers, and 4) identify the technology issues for laser propulsion with visible lasers.

The technical approach for the previous program phase[14] involved performing theoretical modeling and systems analysis along with supporting experimental studies using a commercially built pulsed XeF laser. Although it has not been established that XeF (0.35 μm) is indeed the desirable wavelength, the advanced nature of excimer laser technology has led to the availability of commercially built lasers with sufficient energy and the proper pulse time to perform meaningful scaling experiments. The analytical aspects of this program were divided into studies of propulsion physics wavelength scaling and mission analysis to identify DOD applications of laser propulsion systems. The propulsion physics studies were carried out at PSI, and the mission analysis was performed both at PSI and the Lockheed Missiles and Space Company under subcontract to PSI. The experimental program was performed at PSI using in-house pulsed lasers.

As a result of the mission analysis, several attractive missions were identified with perhaps the most attractive near term one being the orbital repositioning of satellites. In addition, the absorption physics scaling experiments served to establish the wavelength scaling of breakdown and absorption in several gases of interest. For argon, the experimental measurements were also supported by corresponding theoretical model calculations of the plasma formation process. Finally, preliminary single pulse 0.35 μm thruster performance data were acquired and compared with numerical code simulations of the experiments that model the laser absorption physics, equilibrium gas chemistry (including multiple ionization) and gas dynamics expansion. The latter data indicated that laser to blast wave energy conversion efficiencies in excess of 50% are possible at this wavelength.

For the present program, work was carried out in three areas: 1) experimental thruster performance experiments to extend the previous single-

pulse 0.35 μm data to multiple pulse operation, 2) modification of the numer-
ical flow code to simulate the fluid dynamics appropriate to repetitively-
pulsed operation, i.e., a nozzle that has only partly refilled with fresh gas
prior to each laser pulse, and 3) an analytical assessment of the optical per-
formance of a self-focusing paraboloidal nozzle.

The thruster performance experiments were carried out using a small
scale conical nozzle, external focusing optics, and pulsed CO_2 ($\lambda=10.6$ μm) and
pulsed XeF ($\lambda=0.35$ μm) lasers as the propellant heating sources. All experi-
ments were performed in a vacuum environment. With the XeF laser ($E_p=2.7$ J,
$\tau_p=0.6$ μs) and argon propellant, a maximum specific impulse of 500 seconds was
achieved with a conversion efficiency of laser energy to propellant kinetic
energy upwards of 50%. With the same propellant and the CO_2 TEA laser
($E_p\approx6.5$ J, $\tau_p\approx3$ μs), the maximum specific impulse was 700 seconds with a laser
to kinetic energy conversion efficiency ≈ 20%. Finally, using hydrogen pro-
pellant and the CO_2 laser as the heating source, the experimental data indi-
cate specific impulse up to 3000 seconds with corresponding energy conversion
efficiencies upwards of ≈ 70%. The experimental results are presented in Sec-
tion 3.

In support of the thruster performance experiments, the detailed com-
puter model that was developed previously was modified and used to simulate
the nozzle fluid dynamics in the conical thruster. The model treats non-
steady nozzle flow of a real gas with laser heat addition. Major emphasis in
the present work was directed toward simulating the fluid dynamics appropriate
for repetitively-pulsed operation, i.e., the situation in which the nozzle has
only partly refilled with fresh gas between successive laser pulses and the
remaining downstream section of the nozzle contains the low pressure tail of
the previous blast wave. For a given initial propellant mass distribution and
laser input, the computer program calculates such quantities as the exhaust
gas momentum, kinetic energy, and specific impulse. The model calculations
are described in Section 2.

Finally, an assessment has been made of optical design criteria for a
self-focusing paraboloidal nozzle. The primary conclusions reached are:
1) the mission requirements for off-axis performance allow the surface to be

4

of only very modest optical quality, 2) for off-axis angles $\geq 10^{\circ}$, only very modest magnifications (≤ 25) can be anticipated, 3) optimum optical and fluid dynamic performance appear to be mutually exclusive, consequently a compromise is required, and 4) the impact of off-axis focusing and breakdown on thruster performance should be evaluated. The details of the optical assessment task are presented in Section 4.

1.1 REFERENCES

1.1. Pirri, A. N., Simons, G. A., and Nebolsine, P. E., "The Fluid Mechanics of Pulsed Laser Propulsion," PSI TR-60, Physical Sciences Inc., July 1976.

1.2. Nebolsine, P. E., Pirri, A. N., Goela, J. S., and Simons, G. A., "Pulsed Laser Propulsion - Final Report," PSI TR-108, Physical Sciences Inc., February 1978.

1.3. Nebolsine, P. E., Pirri, A. N., Goela, J. S., and Simons, G. A., "Pulsed Laser Propulsion," Paper VI-2, AIAA Conference on Fluid Dynamics of High Power Lasers, Cambridge, MA, October 1978.

1.4. Rosen, D. I., Kemp, N. H., Weyl, G., Nebolsine, P. E., and Kothanda-raman, G., "Pulsed Laser Propulsion Studies, Vol. I: Thruster Physics and Performance," PSI TR-184, Physical Sciences Inc., Andover, MA, October 1982.

2. MODELING OF A PULSED LASER-HEATED THRUSTER - SINGLE PULSE AND MULTIPLE PULSE OPERATION

2.1   Introduction

The main purpose of the modeling effort was to calculate the flow in a nozzle which was only partly filled with fresh gas. This simulates the case in which the time between laser pulses is short enough so that the nozzle does not refill completely after the flow from the stagnation chamber restarts. The region of the nozzle near the throat contains the fresh gas which has entered through the throat. However, the rest of the nozzle contains heated gas left over from the previous pulse, which is at much lower density.

An estimate of the time necessary to fill the nozzle can be obtained from the ratio of the nozzle length to the limiting velocity of the incoming gas. For 300 K argon the limiting velocity is 5.59×10^4 cm/s, so for a 10 cm nozzle length it takes 180 µs to fill the nozzle. The time for the laser-generated blast wave to traverse 10 cm might be another 10 µs. So if the inter-pulse time is less than 200 µs (more than 5000 pulses per second) the tail of the previous pulse will still be in a 10 cm nozzle when the next pulse occurs. Such conditions were explored in the experiments (see Section 3).

The purpose of having a pulse repetition rate higher than the rate which permits complete refilling is to increase the average specific impulse. It is clear that the fluid mechanics will be different if part of the nozzle is filled with the lower density gas representative of the tail of the previous pulse, instead of the fresh gas which has come in through the throat.

An early study of the fluid mechanics of pulsed laser propulsion by Simons and Pirri (Ref. 2.1) dealt with the multi-pulse problem. However, the valuable analytical modelling in that paper was restricted to a perfect gas, and utilized blast wave theory, in which the shock wave is always hypersonic relative to the gas in the nozzle. In the work described in Ref. 2.2 these two restrictions were removed. A computer model of the non-steady nozzle flow of a real gas with laser heat addition was constructed, and used to perform single pulse calculations.

7

During the course of the present work, this computer program, described in Ref. 2.2, was modified to simulate the flow in the partially-filled nozzle and some runs were made to compare the filled and partially filled cases. This part of the work is described in the next section.

The program was also used to aid the experimental diagnostics by providing shock wave position vs. time (trajectories) as well as shock peak pressure vs. shock position, for some early experiments in quiescent air. The correlations resulting from these calculations are presented in the second section below.

2.2   <u>Second Pulse Simulation</u>

Some additional output of the LSDNS computer program was developed in order to aid the interpretation of the results of the calculations. To motivate the additional output, the quasi-one-dimensional conservation equations which are solved are restated here:

Mass: $\dfrac{\partial \rho A}{\partial t} + \dfrac{\partial \rho u A}{\partial x} = 0$

Momentum: $\dfrac{\partial \rho u A}{\partial t} + \dfrac{\partial}{\partial x} [A(p+\rho u^2)] = p \dfrac{dA}{dx}$

Energy: $\dfrac{\partial}{\partial t} [\rho A(e+u^2/2)] + \dfrac{\partial}{\partial x} [\rho u A(h+u^2/2)] = 0$

The equations are written in conservation form. The quantities in the time derivative terms are usually called the conserved quantities, while those in the space derivative terms are the fluxes of mass, momentum and total enthalpy.

The computer program was modified to print and plot the x-distributions of ρA, $\rho u A$, $\rho A(e+u^2/2)$, and the x-distributions of the time integrals of $\rho u A$, $\rho A u^2$, and $\rho u A(h+u^2/2)$. The latter three flux integrals might be called the mass, momentum and energy fluences.

The average exhaust velocity for a pulsed propulsion device can be defined in terms of a mass-averaged exhaust velocity and the mass fluence as

$$u_{avg} = \int_0^t \rho A u^2 \, dt / \int_0^t \rho A u \, dt \qquad (2.1)$$

8

where the integrals are evaluated at the exhaust plane. The denominator is the expelled mass, the numerator the exhaust momentum.

To simulate the presence of the tail of the previous pulse in the nozzle, a reduced density region is required. The computer program initially fills the nozzle with steady supersonic flow from given stagnation conditions, assuming a perfect gas. A simple way to introduce a reduced density region into this flow is to merely divide the density by some given factor in the region downstream of the desired nozzle station. However, it is not desirable to introduce a pressure discontinuity, since the calculation scheme will treat that as an interface to be resolved by another shock wave, which is not the intent. To avoid a pressure discontinuity wherever the density is reduced, the internal energy can be increased by the same factor (equivalent for a perfect gas to increasing the temperature). This will keep the variation of pressure continuous.

This idea was implemented in the computer program by introducing as new input quantities a station at which the density and internal energy change, and the factor by which the former decreases and the latter increases.

A number of runs were made in real argon, using the thermodynamic table for triply-ionized argon described in Ref. 2.2 which is valid for densities above 10^{-7} g/cm^3 and internal energies up to 2.5×10^{12} erg/g. Below 10^{-7} g/cm^3 the program uses the perfect gas law for argon.

The nozzle geometry was the conical shape, with a 10° half angle and a throat diameter of 0.1016 cm.

The location of the density and internal energy changes was taken at 2 cm from the nozzle throat. For a stagnation temperature of 300 K, which yields a limiting velocity of 5.59×10^4 cm/s, 2 cm is traversed in 36 µs. This condition was one chosen for the second pulse experiments, and was used in the calculations to simulate those experiments.

The stagnation conditions used were 10 atm and 300 K. The runs were made in the blast wave mode of the program. A given amount of laser energy is put into a

small region of the nozzle near the throat to determine the initial thermodynamic conditions there, and then the calculation proceeds to resolve the resulting discontinuity, much like a shock tube flow. For these runs, 1 J was put into the region extending from the throat to 0.1 cm downstream. This is a volume of 1.125×10^{-3} cm^3. The density there was taken to be uniform at the value in the perfect gas nozzle flow at 0.1 cm, which is 3.66×10^{-3} g/cm^3. The resulting internal energy for 1 J is 2.429×10^{12} erg/g, leading to a temperature of 73,000 K and a pressure of 2.0×10^9 dynes/cm^2 (1950 atm).

The density reduction factor was taken as unity (no reduction), 100 and 1000 in three runs, to compare the effects of having the tail of the previous pulse in the nozzle. In order to see which density reduction factor is most realistic, the density at 2 cm from the throat was plotted vs. time for each of these three runs, as shown in Fig. 2.1. The density at that location when the nozzle is filled with gas from the stagnation chamber is 8.48×10^{-5} g/cm^3, shown by the line at the top. The open squares are for the run with no density reduction, the open circles for a factor of 100 reduction and the filled circles a factor of 1000 reduction. Figure A shows that there is not much difference in the density history for the reductions of 100 and 1000. They both reach 8.5×10^{-7} g/cm^3 at about 21 μs, and extrapolation indicates they would reach 8.5×10^{-8} g/cm^3 at about 40 μs. For the no-reduction run, the densities are slightly higher, reaching these values at 24 μs and 55 μs, respectively. At 36 μs, which it takes to traverse 2 cm at the limiting velocity, the density at two centimeters is nearer to the factor of 1000 reduction than the factor of 100, which indicates that the former is perhaps a more realistic simulation.

Of course, in the actual case, the properties of the gas in the tail have a distribution which is different from that obtained by merely changing the nozzle flow state by some factor. The present calculations should be looked upon as a qualitative indication of the effect of having the previous pulse tail in the nozzle, not a precise numerical simulation.

In order to evaluate the effect of the density reduction we will compare the results of the computer calculations for the no-density-reduction and factor-of-1000 reduction cases.

Fig. 2.1 Density at 2 cm in real argon, for stagnation conditions of 300 K and 10 atm, with 1 J deposited between the throat and 0.1 cm. Density reduced by factors of 1, 100 and 1000 at 2 cm before starting the computation.

Figure 2.2 shows u_{avg} vs. x distributions at various times, where x is centimeters downstream of the throat, u_{avg} is measured in units of 1.8625×10^5 cm/s, and the times of the various distributions are in μs. Figure 2.2a is for no density reduction, while Fig. 2.2b is for the factor of 1000 reduction at 2 cm. The reduced density case shows considerably higher values. To convert u_{avg} to specific impulse in seconds, one multiplies u_{avg} by 190.

Recall from Eq. (2.1) that at any x and t, the value of u_{avg} is the ratio of momentum flux passing that x, integrated up to t, to the same integral for the mass flux. Thus, u_{avg} depends on both x and t. Until the shock arrives at any station, the density is fixed and the velocity is approximately the limiting velocity, which is 5.5875×10^4 cm/s for 300 K. This is, in fact, the value that u_{avg} takes on in front of the shock, as Fig. 2.2a shows. When the shock passes, the gas is accelerated, and u_{avg} increases.

In the no-density-reduction case, the shock keeps swallowing significant amounts of mass as it moves, and this mass must be accelerated. In fact, the mass per unit length the shock swallows is nearly constant, since it is the mass flow in the nozzle divided by the undisturbed gas velocity, which is nearly the limiting speed for most of the nozzle. As a result, the average velocity decreases with x at any given time, and also decreases with time at a fixed x, after the shock passes. Figure 2.2a shows that at 10 cm, shortly after the shock passes (32.6 μs) the I_{sp} is 190 s. At 16 cm and 61.6 μs, the I_{sp} has dropped to 170 s.

When there is a density reduction, the shock swallows only one-thousandth as much gas per unit length, after the reduction, and so can move faster and accelerate the gas to a higher speed. Figure 2.2b shows that at 10 cm and 13.8 μs, the shock has passed and the I_{sp} is 722 s. At 17 cm and 21.8 μs, the I_{sp} is down to 646 s.

The increase in I_{sp} with density reduction is brought on by the considerable reduction in mass fluence. This effect can be seen in the distributions of mass fluence presented in Fig. 2.3. The curves for no density reduction are shown in Fig. 2.3a, where the top of the ordinate scale is 1.5×10^{-1} in units of 3.14×10^{-3} g. At 10 cm and 32.6 μs, 1.82×10^{-4} g has passed, while at 16 cm and 61.6 μs, 1.48×10^{-4} g has passed. The station of maximum mass fluence at a given time is some distance behind the shock wave. For a factor of 1000 density

12

Fig. 2.2a Mass averaged velocity distributions at various times. No density
reduction. Real argon for stagnation conditions of 300 K and 10 atm,
with 1 J deposited between the throat and 0.1 cm.

Fig. 2.2b Mass averaged velocity distributions at various times. Density re-
duced by a factor of 1000 downstream of 2 cm. Real argon for stagna-
tion conditions of 300 K and 10 atm, with 1 J deposited between the
throat and 0.1 cm.

14
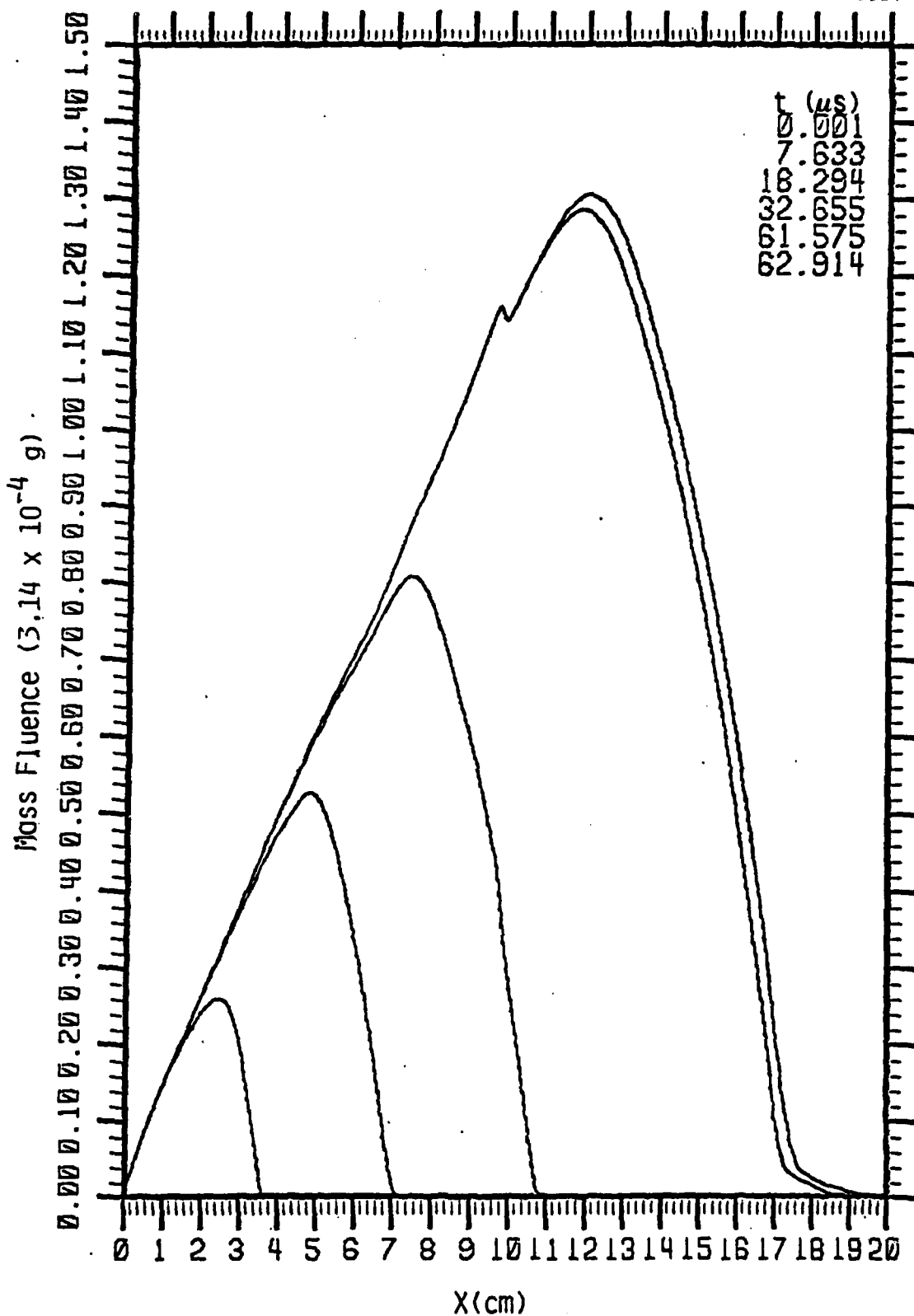
Fig. 2.3a Mass fluence distribution at various times. No density reduction.
Real argon for stagnation conditions of 300 K and 10 atm, with 1 J
deposited between the throat and 0.1 cm.
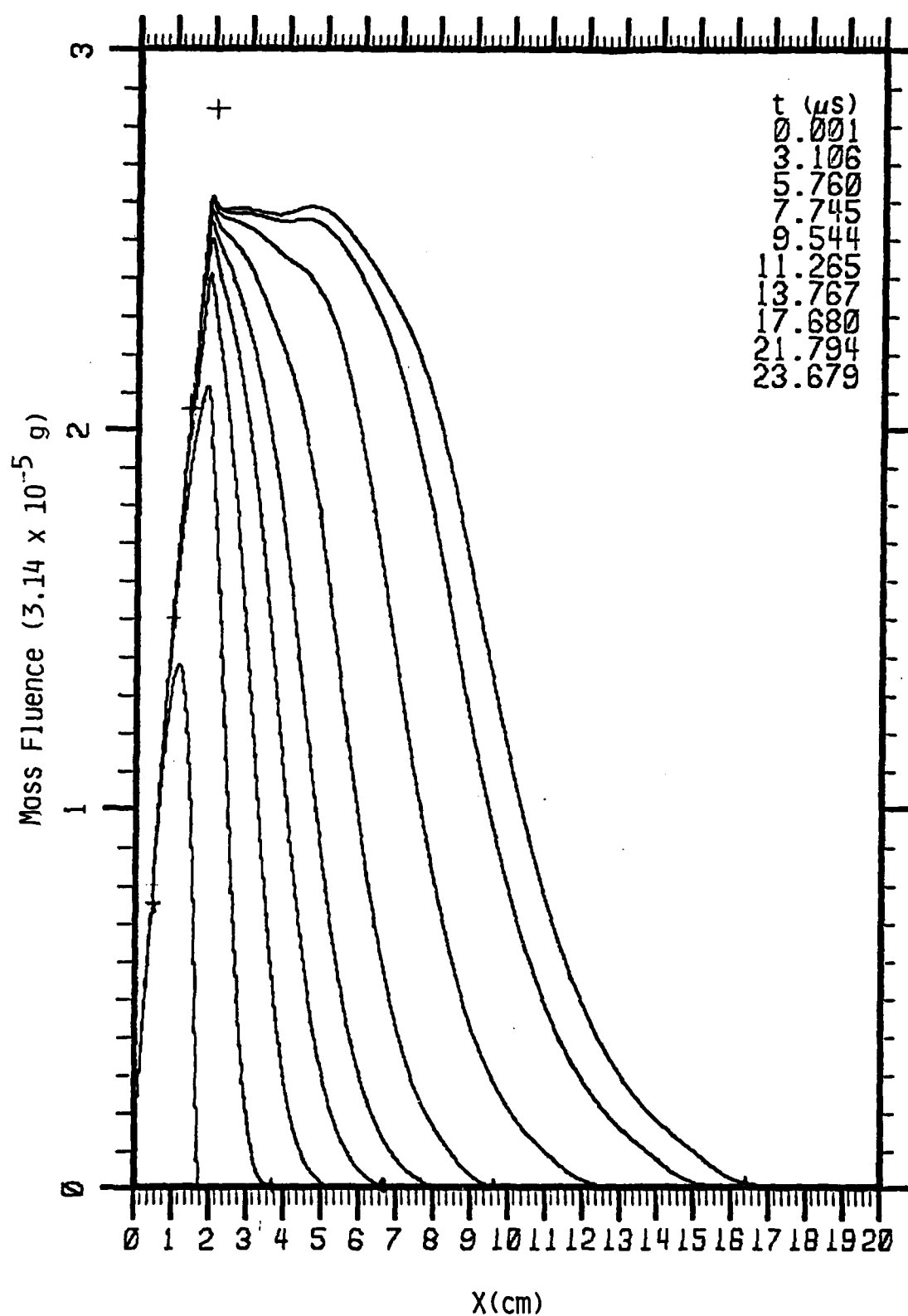
Fig. 2.3b Mass fluence distributions at various times. Density reduced by 1000 at downstream of 2 cm. Real argon for stagnation conditions of 300 K and 10 atm, with 1 J deposited between the throat and 0.1 cm.

16

reduction the corresponding curves are shown in Fig. 2.3b where the top of the ordinate scale is 3×10^{-2} in units of 3.14×10^{-3} g (which is one-fifth the value in Fig. 2.3a). Here the shape of the mass fluence curves is much different than in Fig. 2.3a reflecting the fact that nearly all the mass started out between $x=0$ and $x=2$. This amount of mass, 8.98×10^{-5} g, has the value 2.86×10^{-2} on the ordinate of Fig. 2.3b, and the figure shows that at 23.8 μs, when the shock is nearly at 20 cm, only 90% of that amount of mass, at most, has passed any station. Some of the remaining 10% is still in the initial part of the nozzle, while some may represent numerical error, since the time integrations at each station were done rather crudely. The amounts of mass which have passed 10 cm at 13.8 μs, or 17 cm at 21.8 μs are lost at the bottom of the ordinate, but are less than 3×10^{-6} g. It is these small values which are the denominator of u_{avg} at the corresponding points in Fig. 2.2b.

The numerator of u_{avg}, the momentum fluence, is presented in Fig. 2.4. For no density reduction, Fig. 2.4a, the top of the ordinate is 0.15 in units of 5.85×10^2 dyne-s, while the top of the ordinate in Fig. 2.4b is 0.1 in the same units. Again, the values for the no-density-reduction case are higher than those for the factor-of-1000 reduction. However, this reduction is not as large as for the mass fluence, so the momentum to mass fluence ratio, u_{avg}, is higher in the density-reduced case, as we have already seen in Fig. 2.2.

Figure 2.5 shows that the density-reduced case accelerates the gas to higher speeds than the no-reduction case. The gas speed for the no-reduction case is presented in Fig. 2.5a where the top of the ordinate scale is 2 in units of 1.8625×10^5 cm/s. The rapid oscillations up to 5 cm go with the 61.6 and 62.9 μs distributions. They are caused by the discontinuity in the gas law at a density of 10^{-7} g/cm^3 mentioned above, where real argon is used above 10^{-7} and perfect argon below 10^{-7}. Unfortunately, from $x=1$ to 5 cm the density is very close to 10^{-7} at those times, which produces the large oscillations in the velocity as well as all the thermodynamic variables. However, Fig. 2.5a nevertheless shows gas speeds after the shock in the range of 0.9 to 1.6. The corresponding curves for the density-reduced case are shown in Fig. 2.5b, where the top of the ordinate scale is 5 in units of 1.8625×10^5 cm/s (which is 2.5 times the value in Fig. 2.5a. The gas speeds after the shock are in the range of 3.3 to 4.5, about three times as high as for the no-reduction case.
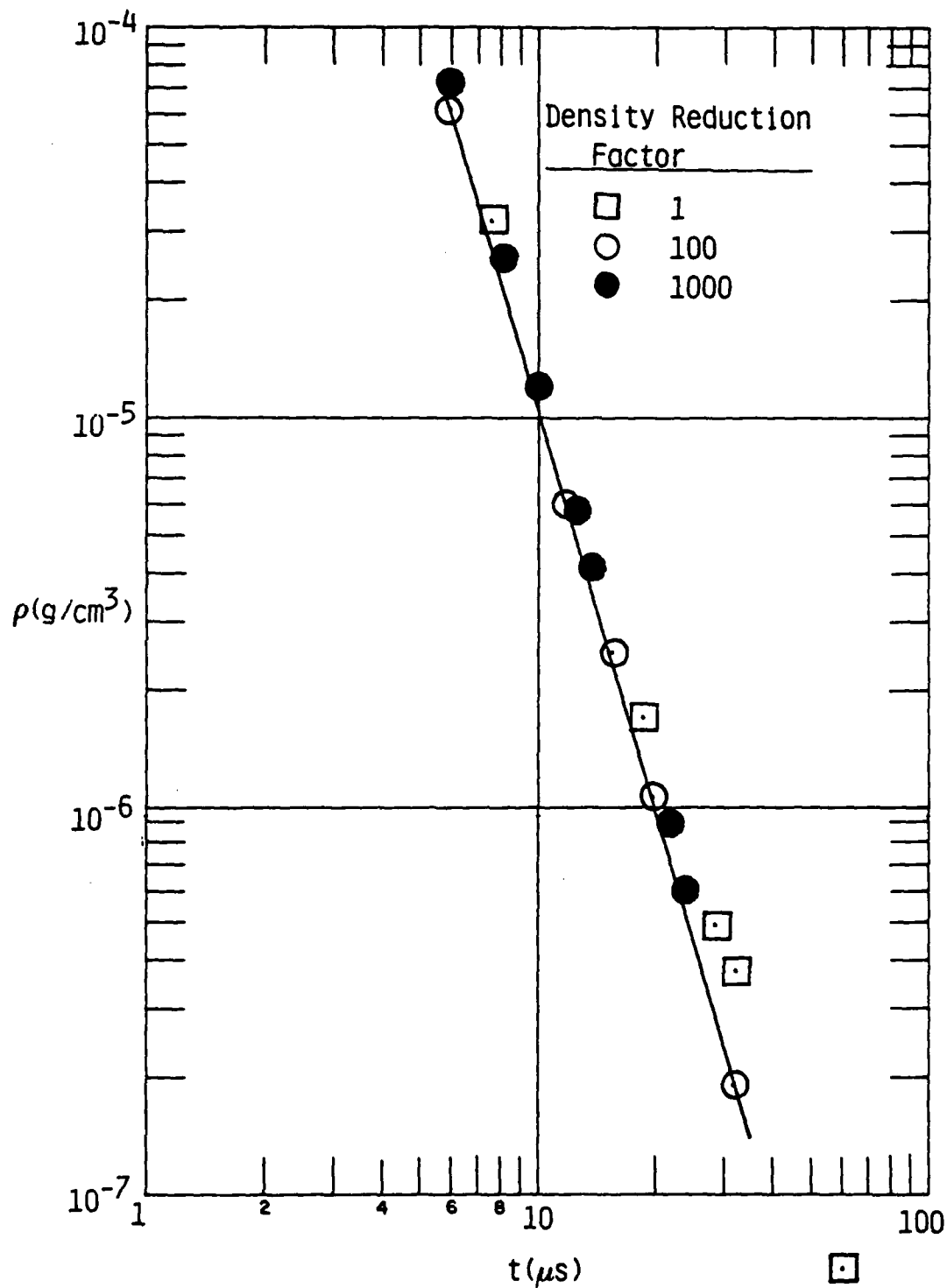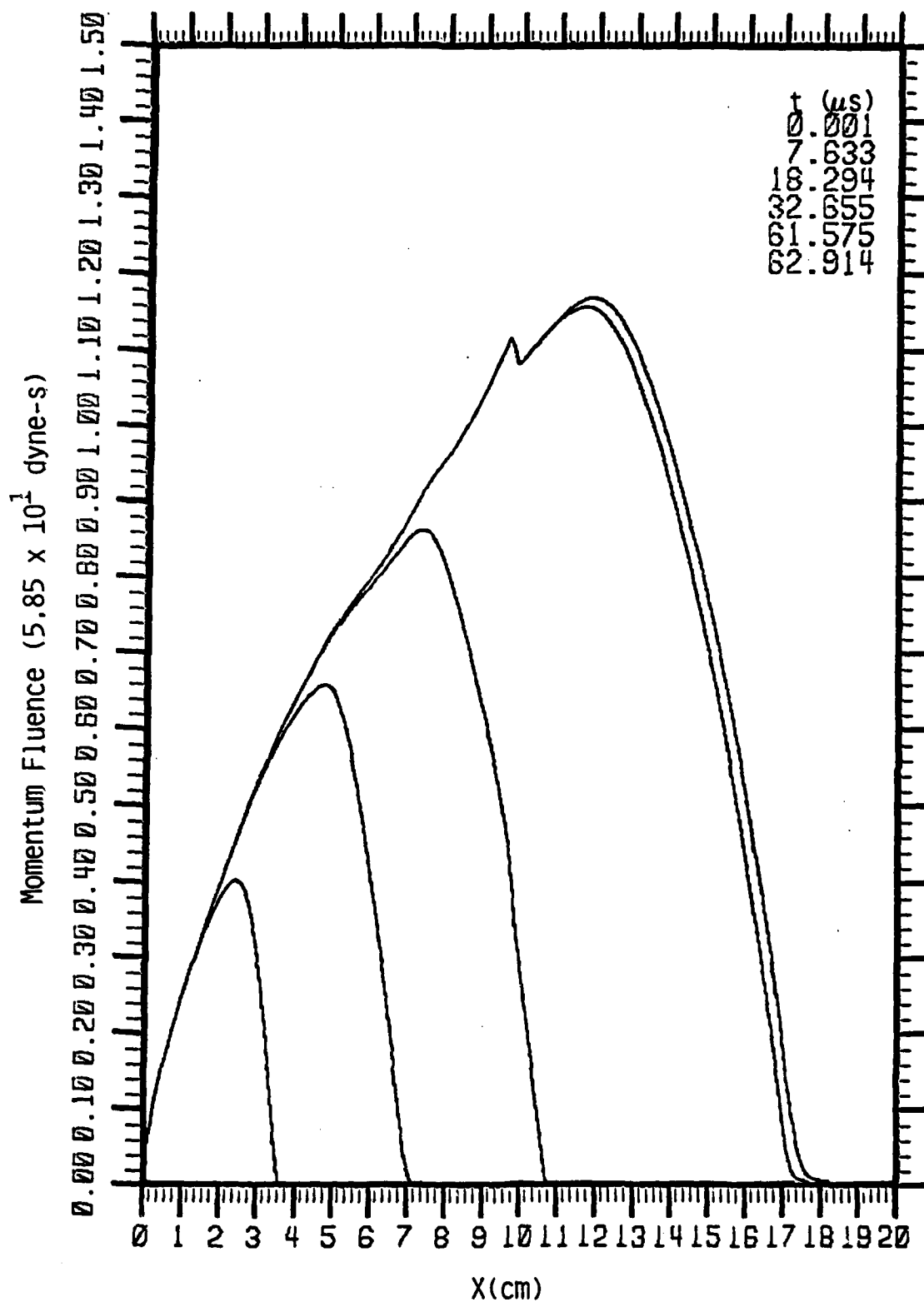
Fig. 2.4a Momentum fluence distributions at various times. No density reduction. Real argon for stagnation conditions of 300 K and 10 atm, with 1 J deposited between the throat and 0.1 cm.

Fig. 2.4b Momentum fluence distributions at various times. Density reduced by
a factor of 1000 downstream of 2 cm. Real argon for stagnation con-
ditions of 300 K and 10 atm, with 1 J deposited between the throat
and 0.1 cm.

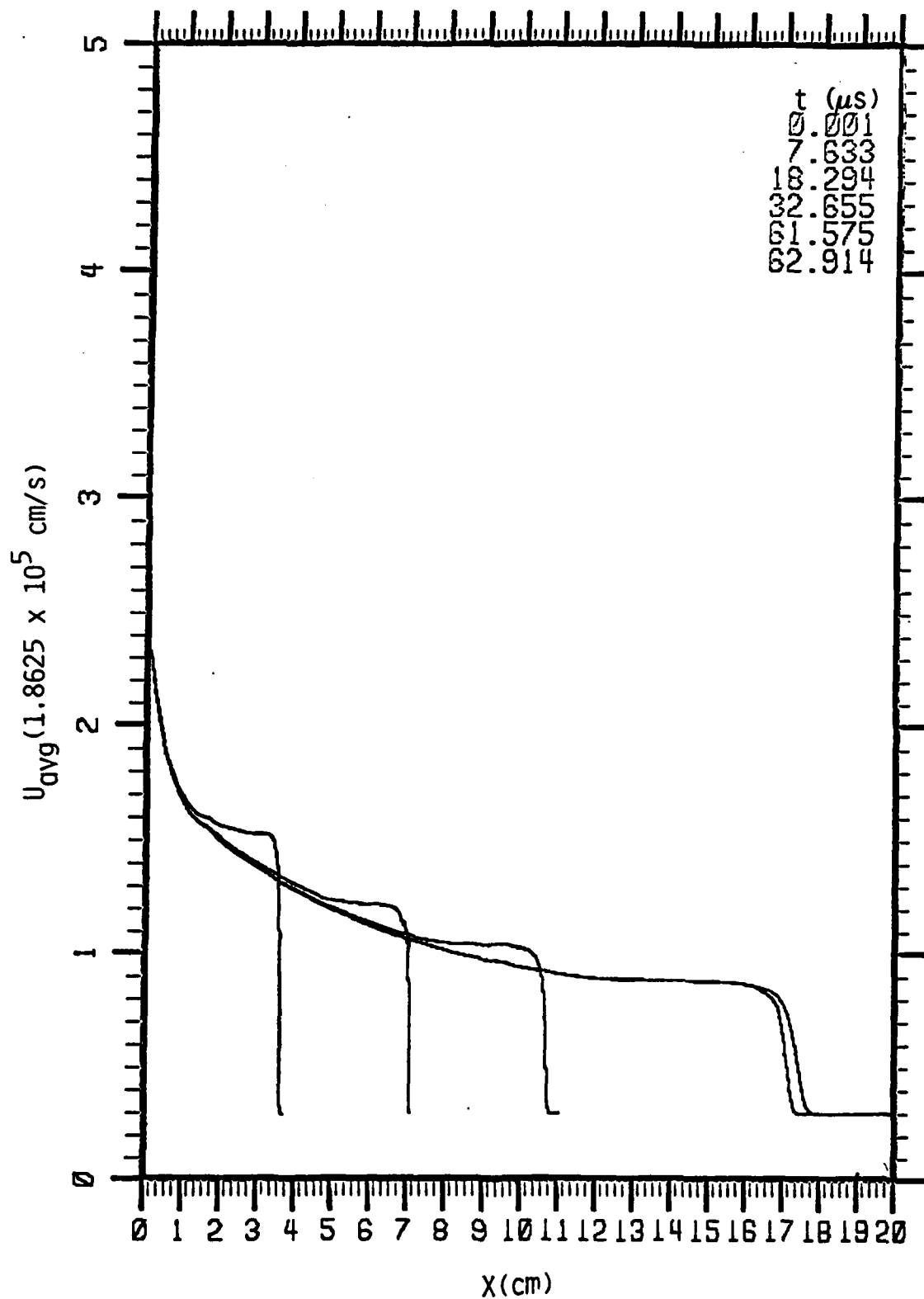Fig. 2.5a Gas velocity distributions at various times. No density reduction.
Real argon for stagnation conditions of 300 K and 10 atm, with 1 J
deposited between the throat and 0.1 cm.
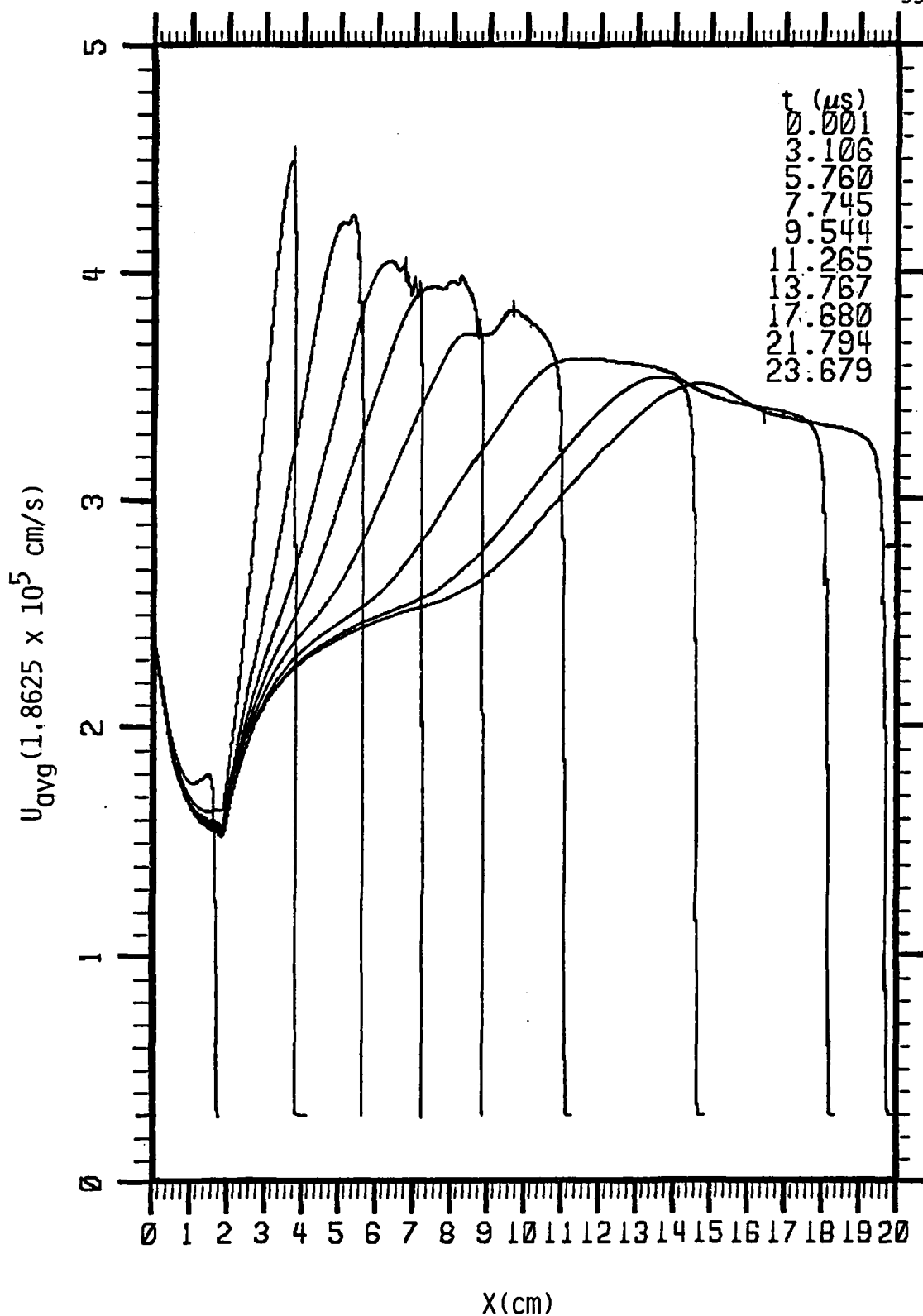
20

Fig. 2.5b Gas velocity distributions at various times. Density reduced by a factor of 1000 downstream of 2 cm. Real argon for stagnation conditions of 300 K and 10 atm, with 1 J deposited between the throat and 0.1 cm.

21

The tick marks on the curves in Fig. 2.5b give the location at which the mass, integrated from the throat, equals the mass originally located from x=0 to 2 cm, namely 8.98×10^{-5} g. This is the gas which represents the new gas injected from the stagnation chamber for the current pulse. The gas from the tick marks to the corresponding shock fronts was the reduced-mass gas originally downstream of 2 cm, meant to represent the gas remaining from the previous pulse. The figure shows that both the residual gas and the newly injected gas have been accelerated to high speeds.

This simulation shows that if we fill the nozzle only partially with fresh gas, and fire the laser while the tail of the gas from the previous pulse is still in the nozzle, we can impart a higher momentum per unit mass to the gas, and thus a higher specific impulse.

As an aid to the experimental diagnostics, plots were also made of the pressure vs. time at two stations in the nozzle where pressure transducers were installed, namely 4.4 cm and 9.4 cm. These plots are shown in Fig. 2.6, where Fig. 2.6a is for the no-reduction case, and Fig. 2.6b for the factor of 1000 density reduction. In the former case, we see that the pressure jumps to its highest value when the shock arrives, and then decays, for both stations. For the reduction case, Fig. 2.6b, the pressure behavior is somewhat different. The pressure at 4.4 cm jumps when the shock arrives, but after a small wiggle, continues to rise for some time before decaying. The pressure at 9.4 cm also jumps upon shock arrival, then decays, but reaches a minimum and rises again. (The dashed part of the curve is an interpolation necessitated by an error in specifying the location of the pressure station during part of the calculation, so the depth of the reduction is not known. However, the right end is defined by two correctly calculated points, so there is no doubt the curve rises.)

The behavior of the pressure shown in Fig. 2.6b has some implications for the interpretation of the pressure transducer data obtained in the double pulse experiments (see, for example, Fig. 3.3). In those experiments, the pressure peak that is observed at each transducer following the second laser pulse is taken to indicate the arrival of the slug of propellant gas heated by that pulse. The propellant exhaust velocity is then inferred from the transit time of this "wave" between the two pressure stations. It appears from Fig. 2.6b that this interpretation may have to be examined more closely.

22
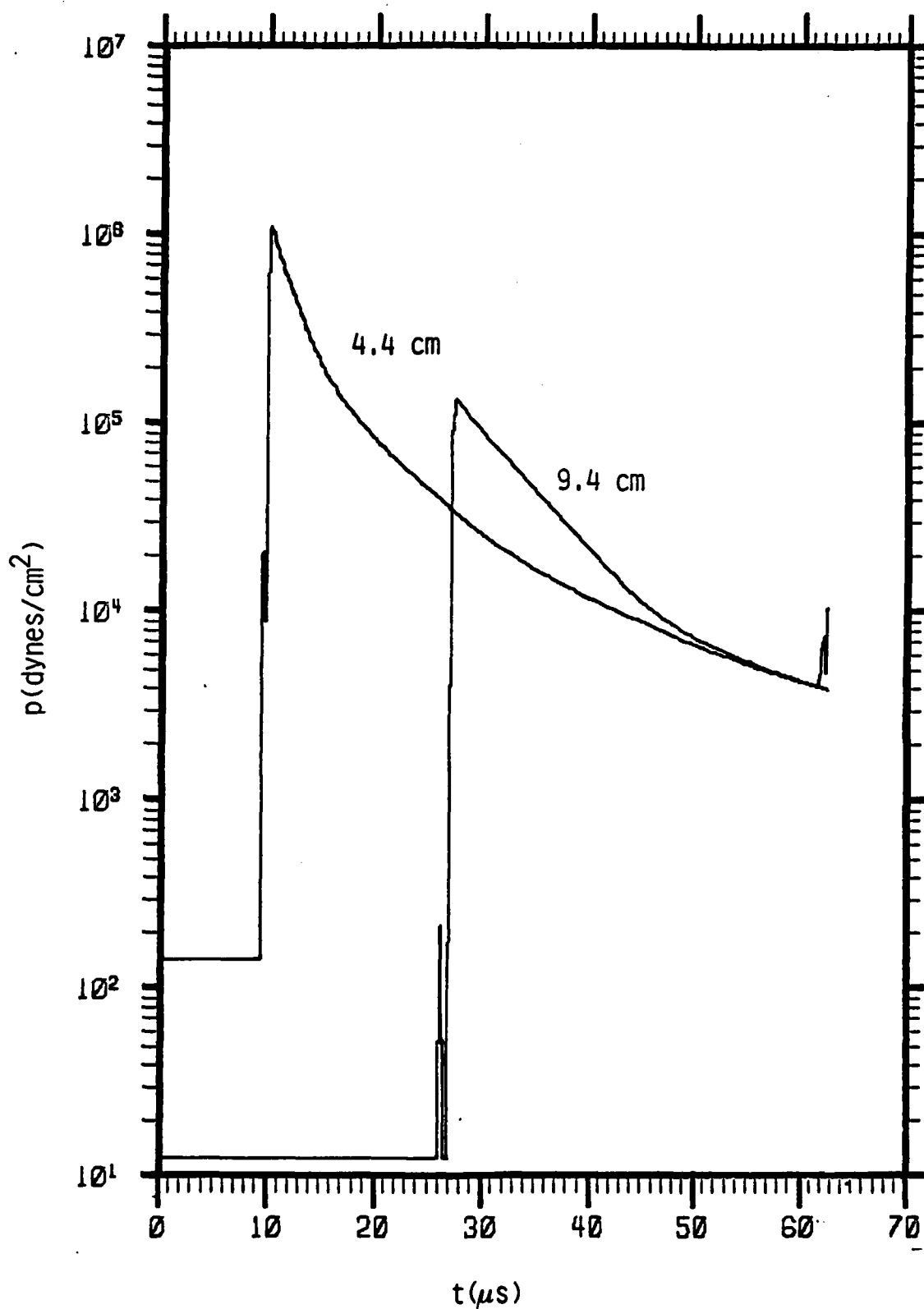
Fig. 2.6a Pressure history at pressure transducer locations. No density reduc-
tion. Real argon for stagnation conditions of 300 K and 10 atm, with
1 J deposited between the throat and 0.1 cm.
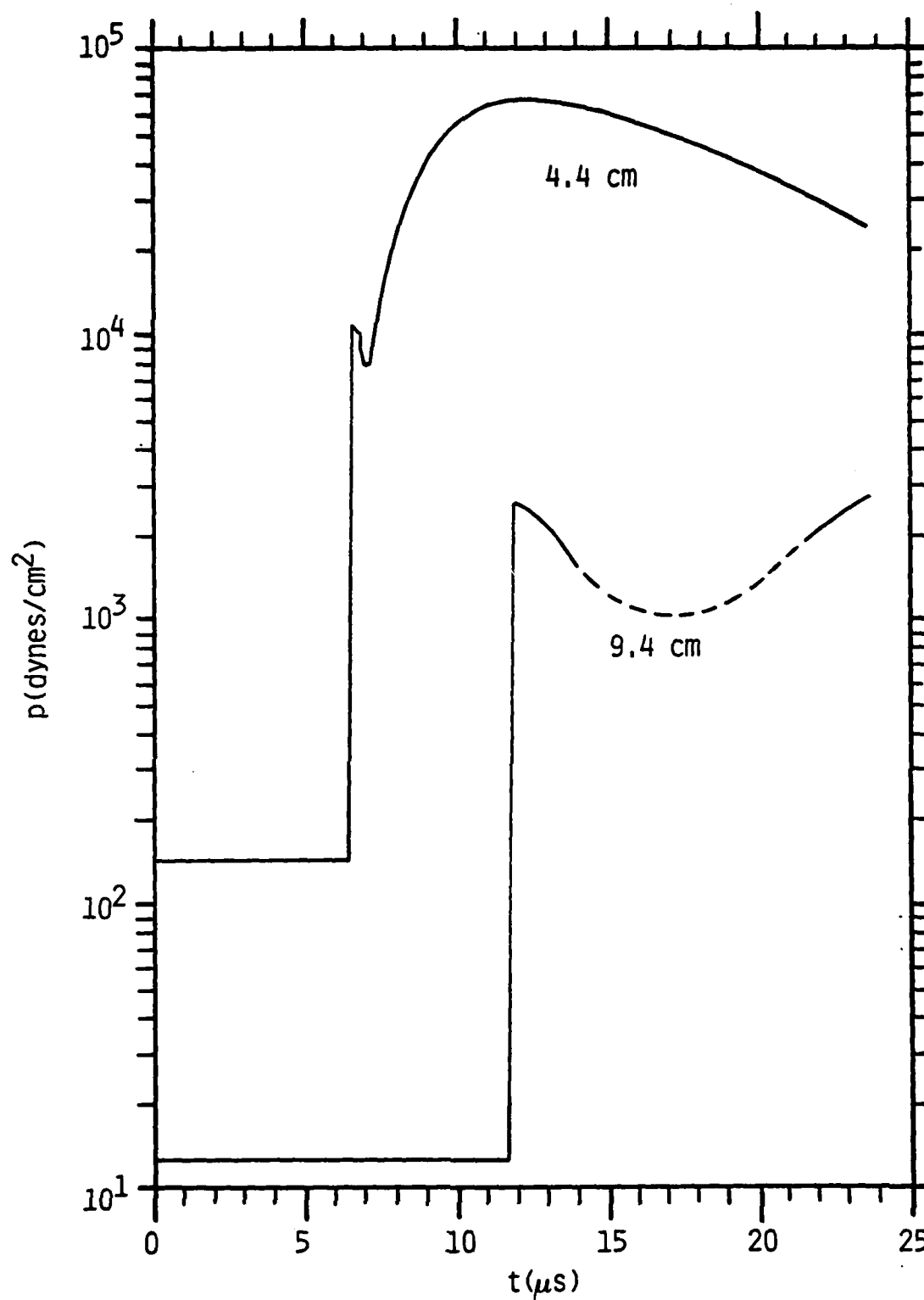
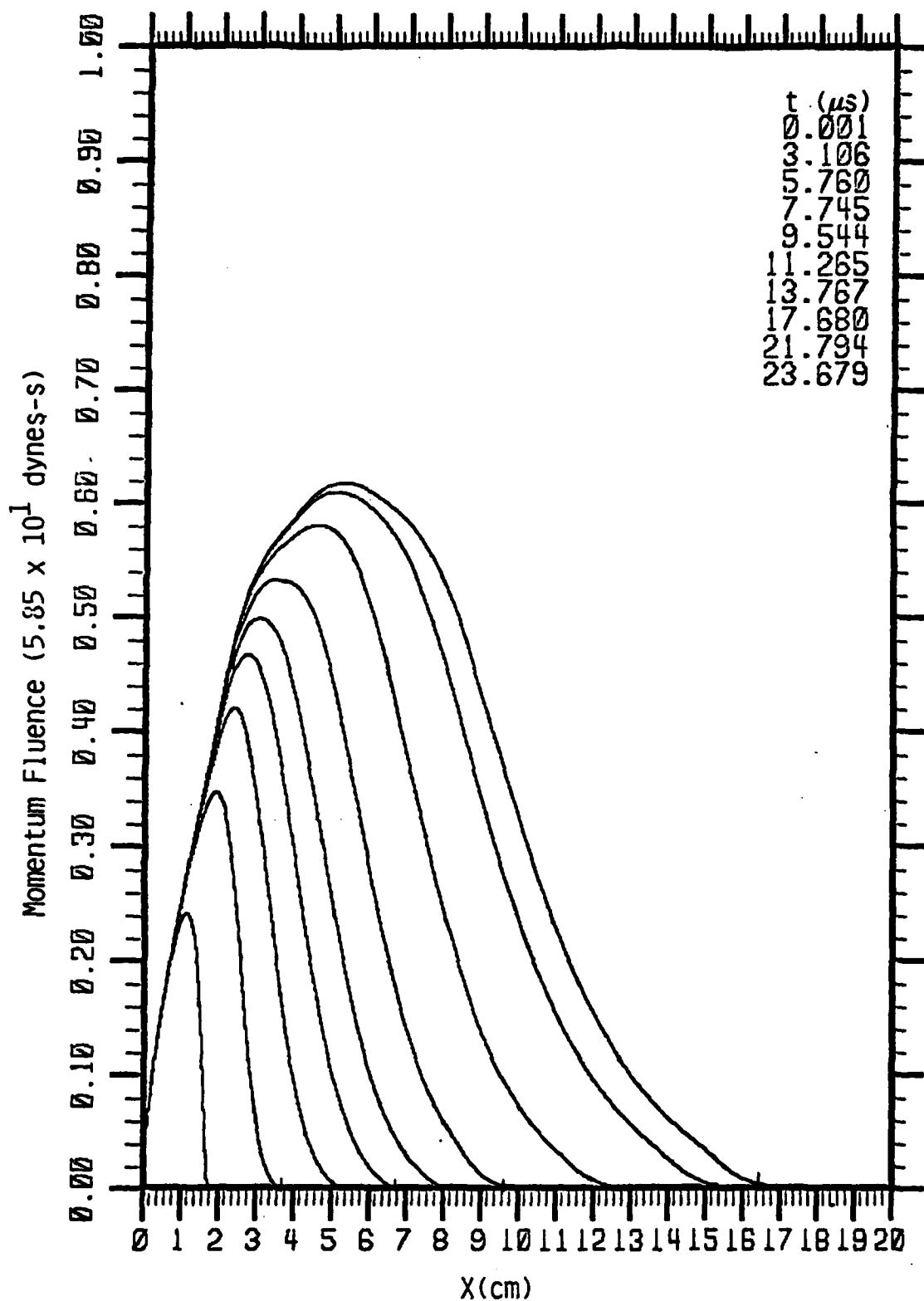Fig. 2.6b Pressure history at pressure transducer locations. Density reduced
by a factor of 1000 downstream of 2 cm. Real argon for stagnation
conditions of 300 K and 10 atm, with 1 J deposited between the throat
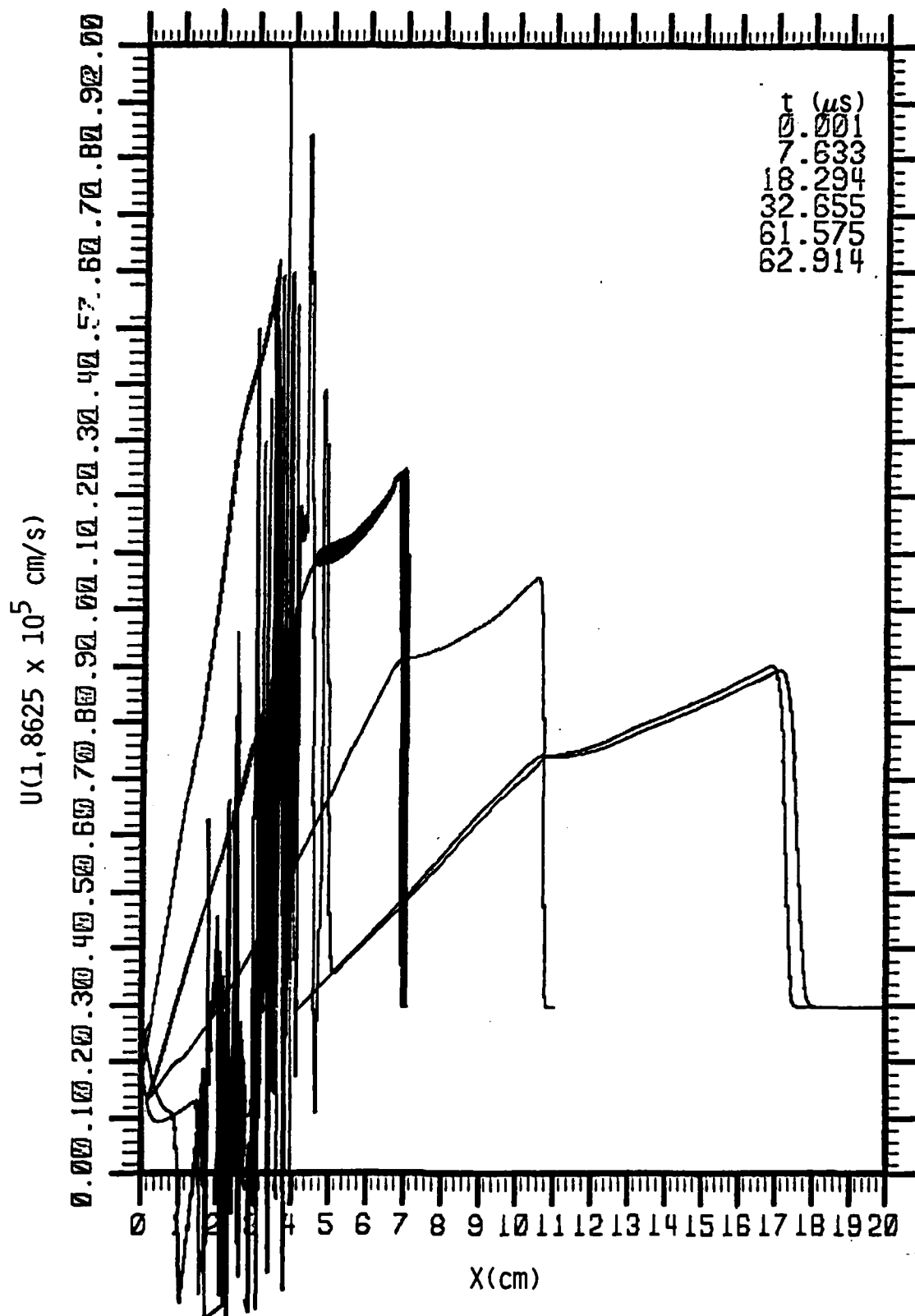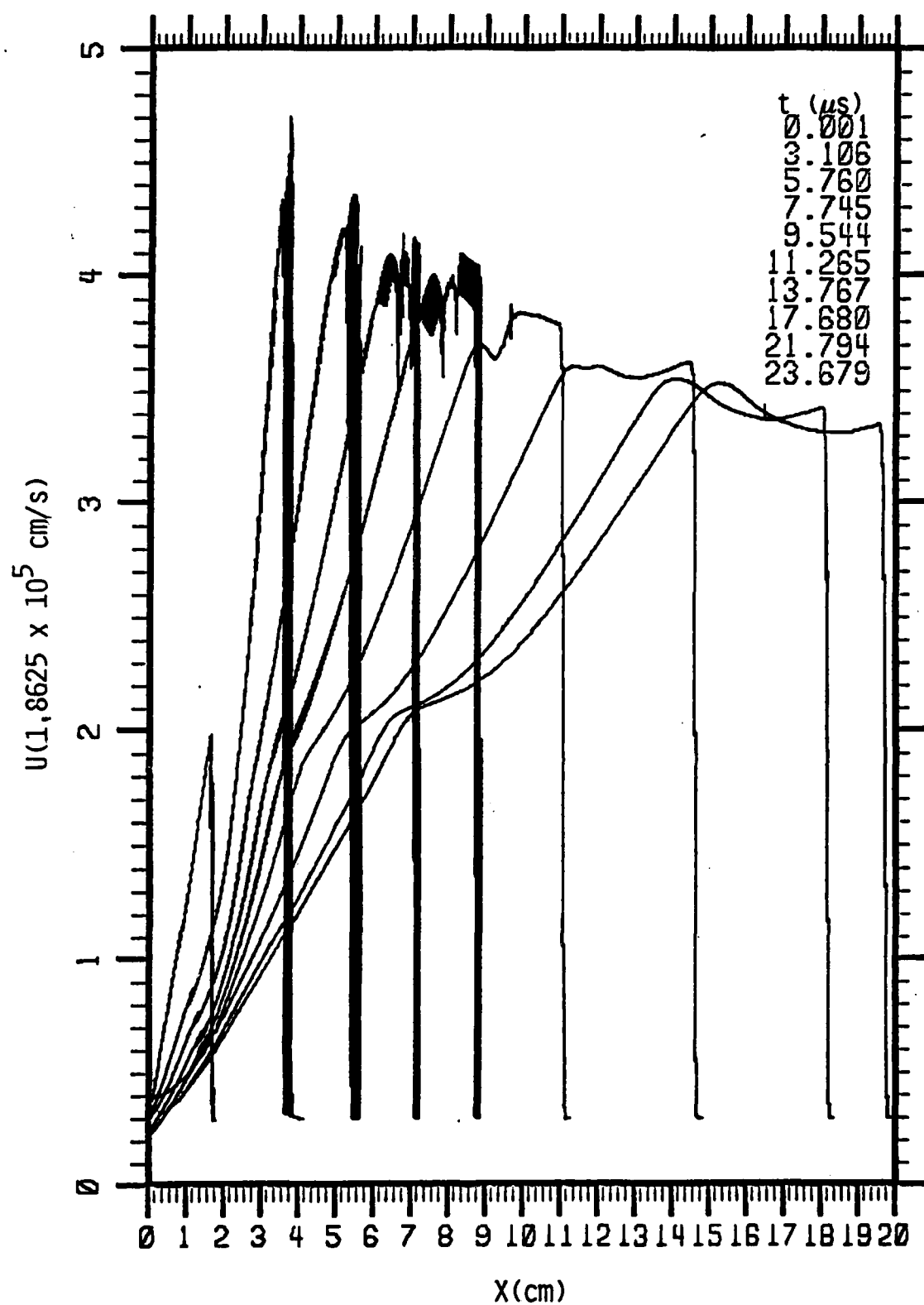and 0.1 cm.

24

2.3   Calculations for Blast Waves in Quiescent Air

As an aid to the interpretation of some experiments in quiescent air, three calculations were performed. In all cases, the initial state of the gas in the nozzle was 1 atm, 300 K, with zero velocity. Energy was deposited into the zone near the conical nozzle throat. The gas there was taken to be at the same density as the nozzle gas, 1.1719×10^{-3} g/cm^3, but at 4000 K. The size of the energy deposition zone was varied to allow different amounts of energy to be deposited. In one run, the region from the throat to 3 cm was taken as hot, corresponding to a deposition of 4 J. In a second run, the region to 1.8 cm was hot, corresponding to a deposition of 1 J. In both cases, perfect air, γ=1.4, was used.

The information desired from these runs was the trajectory of the shock wave, and its peak pressure. Correlation formulas for these quantities were obtained in a manner similar to that described in Section 3.14 of Ref. 2.2, using the appropriate similarity theory of blast waves into quiescent air. The length scale is $(E/\rho_o a_o^2)^{1/3}$ where E is the energy deposited, and ρ_o and a_o are the density and sound speed in the quiescent air. (The latter two for the present case are 1.1719×10^{-3} g/cm^3 and 3.479×10^4 cm/s.) The time scale is this length divided by a_o. Therefore, the similarity variables are

$$\xi = x/(E/\rho_o a_o^2)^{1/3} \qquad \tau = t/(E/\rho_o a_o^5)^{1/3} \qquad (2.2)$$

for length and time.

The shock trajectory in these variables was calculated for each run. The location of the shock at each time was defined by the maximum pressure point, and the corresponding value of ξ was denoted as ξ_p. A plot of ξ_p vs. τ for the 4 J and 1 J cases are shown as the circles and triangles in Fig. 2.7. It can be seen that the scaling represented by Eq. (2.2) reduces the two trajectories to the same curve, in spite of the factor of 4 difference in energy.

In the experiments to be described later, probes were at x=4 and 9 cm, which translate to a pair of values of ξ for each of the two energies. These values are denoted by horizontal ticks on Fig. 2.7. Only the values of ξ between these marks are interesting in using the data from the two probes.
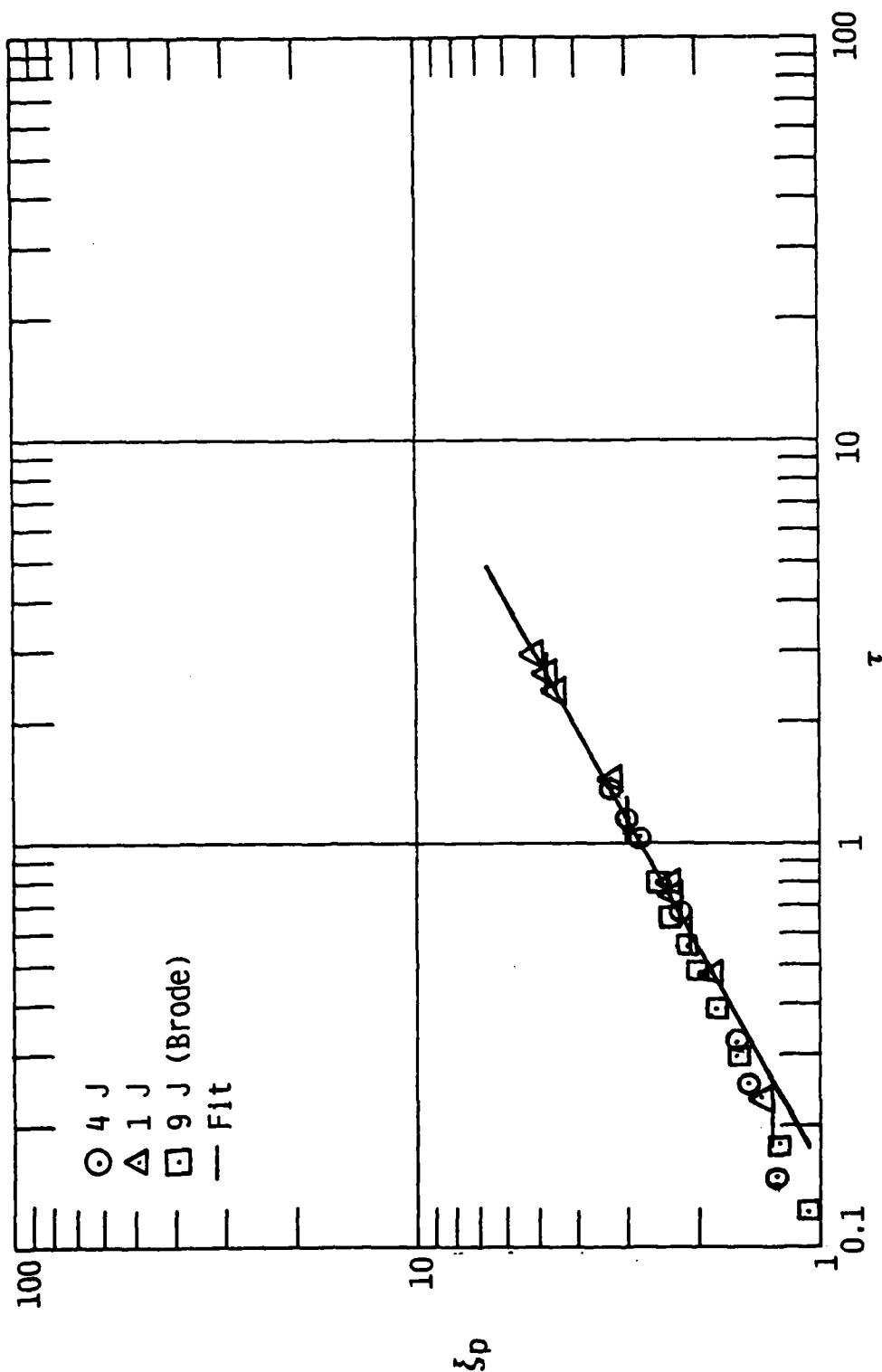
Fig. 2.7 Shock trajectory in quiescent air, expressed in similarity variables, Eq. (2.2). Perfect air, γ=1.4, with ambient conditions of 1 atm and 300 K. Hot gas initial state 4000 K, ambient density, except for squares, where initial state is ambient density, 121 atm pressure.

To correlate these points, a straight line in the log-log plot of Fig. 2.7 was fitted to the points by least squares, excluding the three lowest circle points and the one lowest triangle. This portion of the plot is in the region where the calculation is just starting, at early times, and shows some deviation from a straight line. The equation of the line is

$$\xi_p = 2.76 \ \tau^{0.55926} \tag{2.3}$$

When we revert to physical variables, using Eq. (2.2), and solve for E, we find

$$E = 7.16 \times 10^{-15} \ x_p^{6.807}/t^{3.807} \tag{2.4}$$

in cgs units. This relation expresses the energy in terms of the time of shock arrival at the station x_p, and can be used to infer the energy from the measurement of pressure peak arrival time.

A similar relation between the peak pressure and the location of this peak can be obtained. For the pressure, blast wave theory suggests that the similarity variable is

$$\Pi_p = (p_p - p_o)/\rho_o a_o^2 \tag{2.5}$$

where p_o is the pressure in the quiescent gas, which is 1 atm in the present case. A plot of Π_p vs. ξ for the 4 and 1 J runs is presented as the circles and triangles in Fig. 2.8. Again the two runs fall on a single curve except at low values of ξ_p, which correspond to early times. The vertical ticks again are the locations of the two probes for the two runs.

A straight line was fitted to the circles and triangles, deleting the three circles and two triangles at the upper end. The fit is

$$\Pi_p = 6.6103 \ \xi_p^{-1.918} \tag{2.6}$$

which translates to

$$E = \frac{(p_p - p_o)^{1.5144} \ x_p^3}{2.55 \times 10^4} \tag{2.7}$$
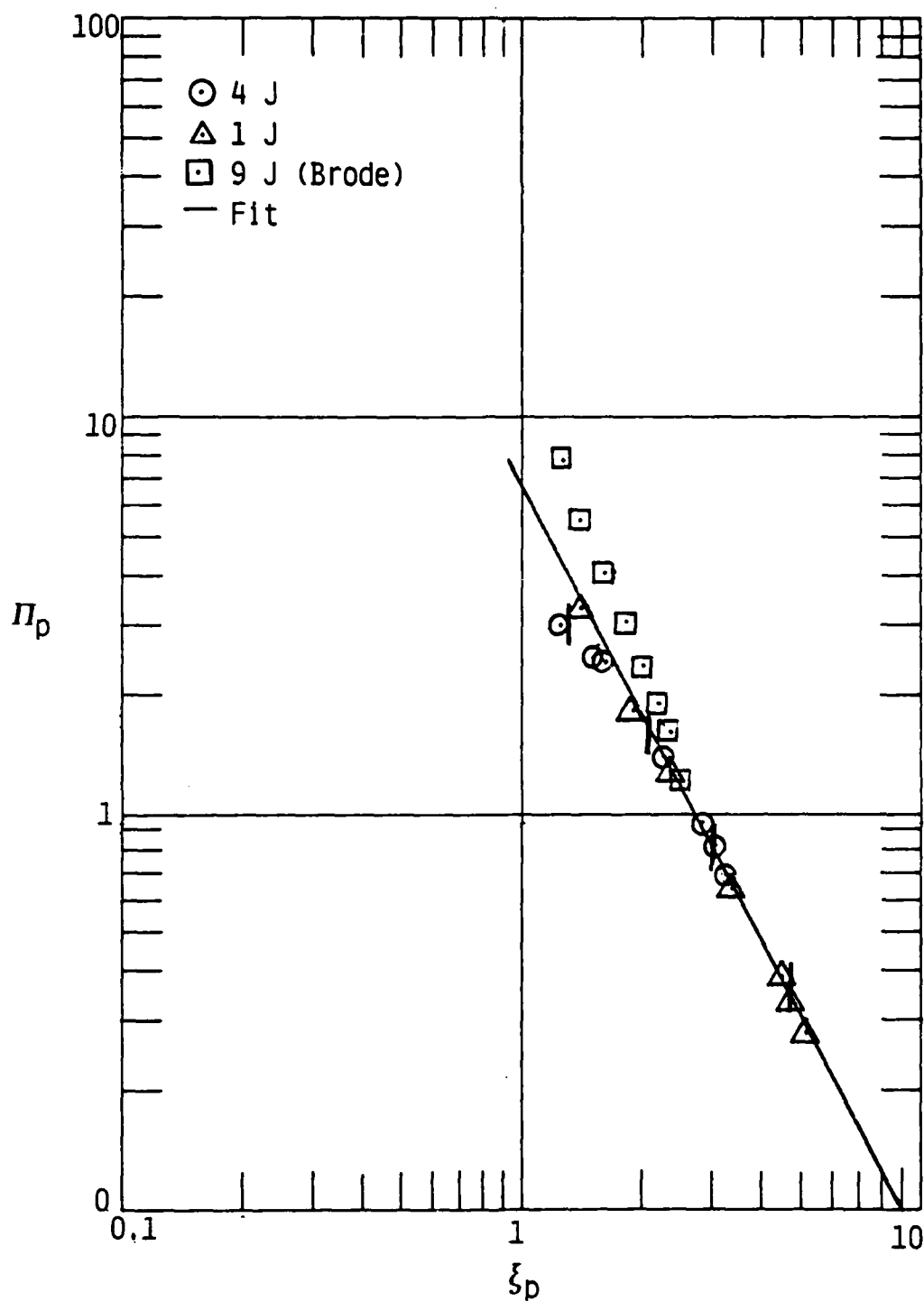
Fig. 2.8 Peak shock pressure as a function of distance, expressed in similarity
variables, Eqs. (2.2) and (2.5). Perfect air, γ=1.4, with ambient
conditions of 1 atm and 300 K. Hot gas initial state 4000 K, ambient
density, except for squares, where initial state is ambient density,
121 atm pressure.

in cgs units. This relation can be used to infer the energy from a measurement of peak shock pressure.

A third run into quiescent air was made as a check case, to compare with a run made by Brode in the early days of the use of computers for fluid mechanics calculations, Ref. 2.3. He calculated the blast wave resulting from the explosion of a sphere of air ($\gamma=1.4$) at ambient density but a pressure of 121 atm, into an ambient gas at 1 atm. He used Lagrangian coordinates and a calculation algorithm introducing artificial viscosity, in contrast to the Eulerian coordinates and Lax calculation algorithm used here.

This case has an energy deposition which corresponds to approximately 9 J in the 10° nozzle used for the present calculations. The results of this calculation, in similarity variables, are shown as the squares on Figs. 2.7 and 2.8. On the former, the squares deviate only slightly from the curve defined by the circles and triangles. In Fig. 2.8, the deviation is larger. However, it must be remembered that the initial pressure in the 4 and 1 J runs was only 13.3 atm, compared to 121 in the Brode run. It also appears from Fig. 2.8 that the squares are merging with the circles and triangles as the pressure drops.

The results of the present calculation for the Brode case were compared with a small-scale plot of peak pressure vs. distance in Ref. 2.3. The agreement seemed to be satisfactory, lending additional confidence to the results of the present computer program.

REFERENCES

2.1   Simons, G. A. and Pirri, A. N., "The Fluid Mechanics of Pulsed Laser Propulsion," AIAA J. 15, 835 (1977).

2.2   Rosen, D. I., Kemp, N. H., Weyl, G., Nebolsine, P. E., and Kothandaraman, G., "Final Technical Report Pulsed Laser Propulsion Studies, Vol. I: Thruster Physics and Performance," PSI TR-184, Physical Sciences Inc., Andover, MA, October 1982.

2.3   Brode, H. L., "Numerical Solution of Spherical Blast Waves," J. Applied Physics, Vol. 26, No. 6, June 1955, pp. 766-775.

3. EXPERIMENTS

This section describes the experimental measurements that were made to assess the performance of a pulsed laser-heated thruster. For the most part, the experiments that were carried out were very similar to those performed previously[3.1] – both in measurement technique and method of analysis. The experiments were performed using a small scale conical rocket nozzle and either argon or hydrogen propellant. The propellant gases were heated by pulses of a TEA CO_2 laser ($\lambda = 10.6$ μm, $E_p \approx 10$ J) and/or an e-beam pumped XeF laser ($\lambda \approx 0.35$ μm, $E_p \approx 4$ J). The laser radiation was focussed into the nozzle using external focussing mirrors and concentrated to sufficient intensity to achieve propellant breakdown just downstream of the throat. The resulting dynamics of the laser-generated propellant shock waves were monitored using high speed piezoelectric pressure transducers mounted in the nozzle wall. Using the numerical code simulations described in the previous section, the pressure transducer data were analyzed to infer estimates of rocket performance. The performance parameters evaluated include conversion efficiency of laser energy to blast wave energy, laser energy to exhaust kinetic energy, and specific impulse, i.e., mass averaged exhaust velocity. All experiments were performed with the nozzle in a vacuum background ($P < 10^{-4}$ atm).

The following subsections describe the experimental apparatus and technique, the rocket performance data and its analysis, and, finally, the conclusions that can be drawn from the experimental results.

3.1 Experimental Apparatus

A schematic diagram of the overall experimental apparatus is shown in Fig. 3.1. In the following subsections, each major component of the apparatus will be described.

3.1.1 Lasers

The Lumonics K-103 pulsed CO_2 TEA laser was installed in a carefully designed and electrically shielded metal box in order to minimize EMI noise pickup by the electronic diagnostics. Attention was paid to shielding against rf radiation, avoiding ground loop problems, and filtering the power line
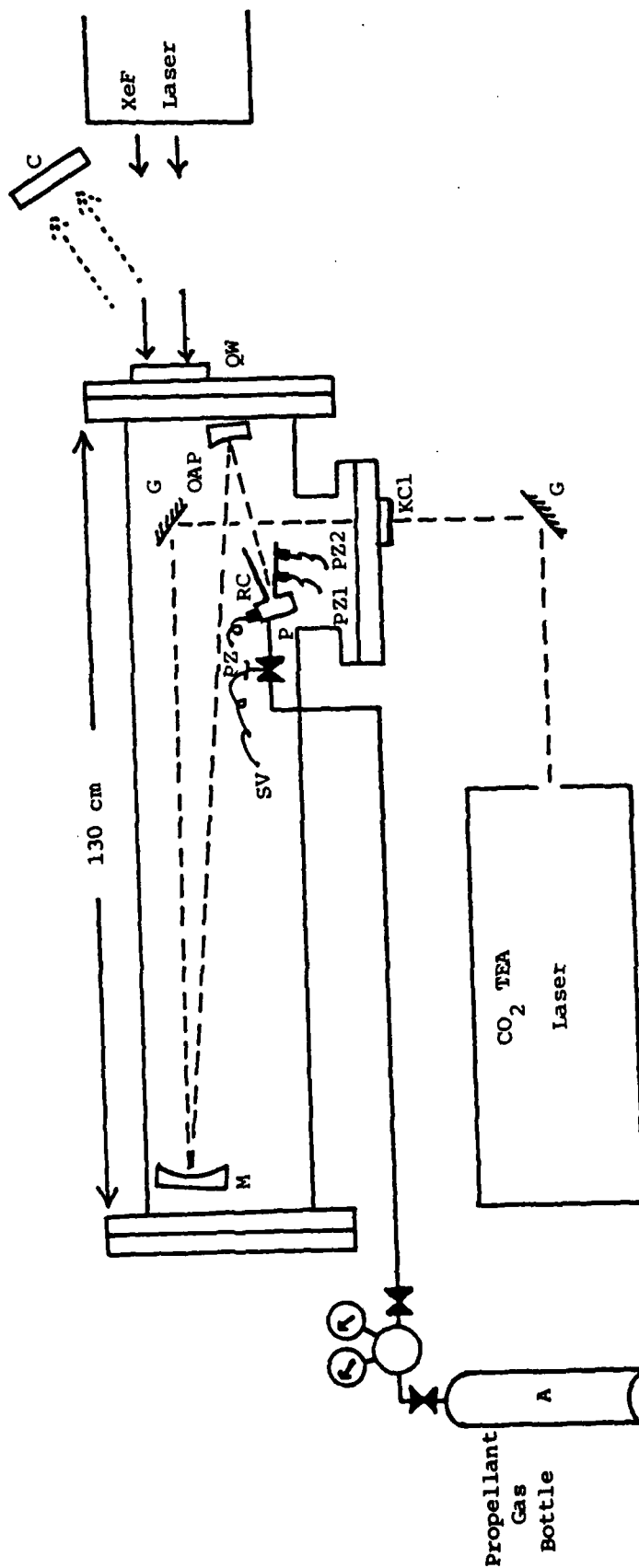
Fig. 3.1 Schematic diagram of laser propulsion experiment:
C - Lumonics 50D calorimeter; QW - quartz window;
M - aluminum coated concave surface mirror (f=160 cm);
OAP - off-axis parabola concave mirror (f=15 cm);
RC - rocket cone; P - plenum, G - gold surface mirror;
KCl - KCl window; PZ - Piezo pressure transducer;
SV - Solenoid valve.

inputs. The CO_2 laser was placed as close to the laser propulsion test chamber as space allowed, thus minimizing the spreading of the beam as it travelled along the optical train and obviating the need for any beam reducing optics.

The details of the pulsed XeF laser (0.35 μm) have been described previously.[3.1]

3.1.2 Test Chamber and Optical Train

The vacuum test chamber used was the same as that described previously.[3.1] As shown in Fig. 3.1, a KCl window (2" diameter and 1/8" thickness) was placed on the plexi-glass flange to allow transmission of the CO_2 laser pulse (10.6 μm) into the vacuum test chamber. The CO_2 laser beam was then turned 90° by a two-by-two inch gold surface mirror and directed to an 8" aluminum coated concave surface mirror (f = 160 cm). The two-by-two inch folding mirror was placed in such a way that it fit inside the hole of the square annular XeF laser beam.

The XeF laser was directed, as shown in Fig. 3.1, to the 8" mirror described in the above. The two laser beams were then directed onto the 3" aluminum coated off-axis parabola. This off-axis parabola mirror focused the two laser beams approximately 21 cm from the mirror. The focal location of the CO_2 laser pulse was carefully identified by observing breakdown sparks in air. For the XeF laser a He-Ne laser beam precisely adjusted to match the profile and propagation axis of the XeF beam, was used to determine the focal point by observing the He-Ne image. It was found that the focal plane of the CO_2 laser beam was approximately 2.5 cm beyond that of the XeF laser. This was the result of the finite wavefront curvature of the CO_2 beam. Nevertheless, when the apex of the rocket cone was placed 0.6 cm beyond the focal point of the XeF laser, the CO_2 laser was powerful enough to induce breakdown. As a result, this configuration was used throughout the experiments. ·

To assess how much optical energy was entering in the rocket, it was necessary to evaluate the reflectance and transmittance of the various mirrors and windows in the optical train. For the optical train associated with the

XeF laser beam, the following values were used: quartz window - 0.92 transmittance and 0.08 reflectance; aluminum coated surface mirrors - 0.88 reflectance. The resulting transmission was 0.655. For the CO_2 laser optical train, the following values were used: gold mirror, $R = 0.97$; KCl window, $T = 0.92$; aluminum coated surface mirrors, $R = 0.95$. Resulting transmission was 0.78.

3.1.3 Rocket Nozzle Design and Propellant Feed System

A schematic diagram of the rocket exhaust cone and the nozzle is shown in Fig. 3.2. The rocket was made of aluminum and the inside surfaces were polished using conventional polishing and buffing techniques. The throat diameter was 1 mm. Piezoelectric pressure transducers mounted flush with the inside wall surface were at 4.3 cm and at 9.3 cm from the apex of the cone, respectively.

For most of the runs, argon gas was used as the propellant and gas flow was controlled by a fast acting electrically activated solenoid valve. The solenoid valve maintained gas flow for approximately 25 ms after it was activated, thus minimizing the pressure rise in the time vacuum chamber. A piezo pressure transducer was also mounted on the rocket plenum to monitor the pressure history as well as the establishment of steady state gas flow through the rocket nozzle. This piezo pressure transducer was calibrated against a conventional gas regulator pressure gauge. The calibration was accomplished by installing the same solenoid valve and plenum assembly (without nozzle) just after the regulator, and then pulsing the gas into the plenum. In this way, pressure drop between the regulator and plenum was minimal. For the actual rocket experiments, in which 5 feet of 6 mm i.d. tubing was required between the regulator and solenoid valve, the maximum plenum pressure was found to be approximately 90% of the regulator delivery pressure.

3.2 Experimental Diagnostics

3.2.1 Piezo Pressure Transducer

Two Kistler pressure transducers were used to monitor the laser-induced shock wave arrival time to calculate shock wave parameters and the

SCHEMATIC OF ROCKET DESIGN

PRESSURE TRANSDUCERS

XeF LASER BEAM

$d^* = 0.1$ CM

20°

BREAKDOWN REGION

PLENUM
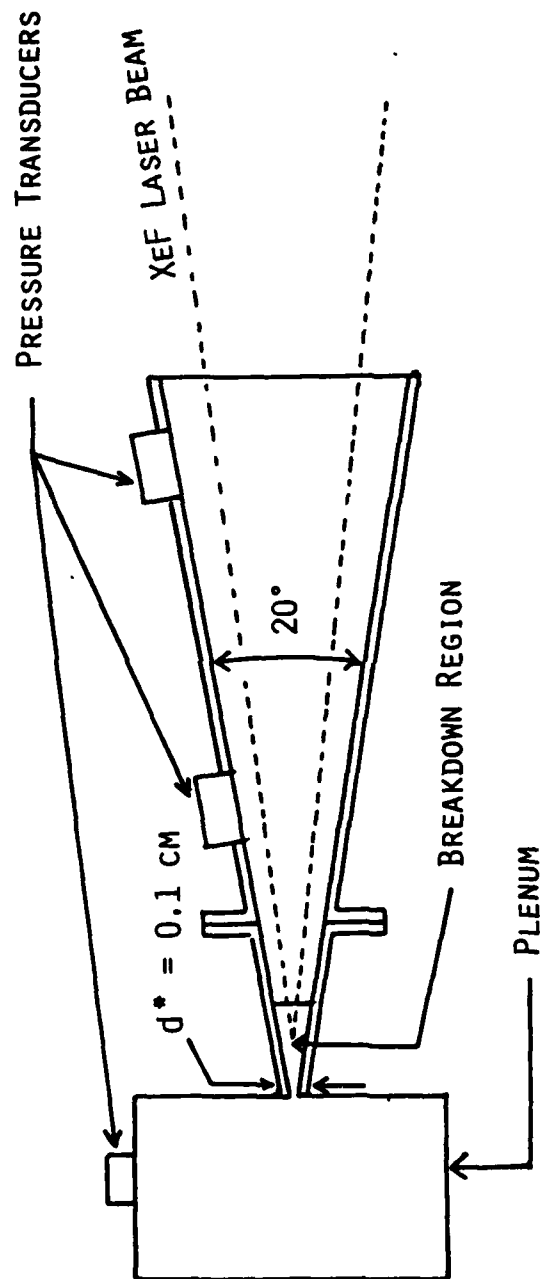
Fig. 3.2 Schematic of nozzle configuration for laser propulsion experiment.

post shock pressure history. The piezo pressure transducers were mounted in Teflon® plugs to minimize mechanical vibrations, and they were mounted flush with the inside surface of the conical rocket wall. The two piezo pressure transducers were installed at 4.3 cm and at 9.3 cm from the apex of the cone. The response time was nominally 1 µs and the responsivity was 25 mV/psi.

3.2.2 Laser Energy Measurement

The XeF laser energy output was monitored by a Lumonics 50D calorimeter measuring the reflected beam from the quartz entrance window (total reflectivity of 8%) as shown in Fig. 3.1.

Energy measurements were carried out always simultaneously with the laser-induced shock transit time measurements, since the energy ouput of the XeF laser varied from run to run. This allowed the evaluation of blast wave energy or kinetic energy conversion efficiency of the XeF laser energy.

CO_2 TEA laser (10.6 µm) energy output was monitored using the same calorimeter, in a separate measurement from the transit time measurement, since the CO_2 laser energy output was very consistent from run to run.

The CO_2 laser beam was directed to the calorimeter through an 8.75% transmittance beam attenuator. The observed energy output was found to be consistently 11.9 J.

3.3 Experimental Technique and Procedure

The test chamber was evacuated to approximately 2×10^{-3} torr. For most of the experiments, argon gas was used as the propellant and was pulsed by a fast solenoid valve to establish steady state flow conditions in the rocket nozzle. 17 ms was required to reach the steady state condition over the delivery pressure range of from 50 psig to 150 psig. The CO_2 TEA laser was then pulsed to create a breakdown in the argon gas and to expand the gas outside of the rocket cone. The breakdown near the apex was of sufficient pressure to temporarily stop the argon gas flow through the nozzle. After a predetermined time delay, the XeF laser was fired into the rocket. The pre-

determined time between laser pulses was chosen to be short enough so that propellant gas refilled only a small portion of the nozzle. As the XeF laser was fired, a simultaneous measurement of energy was carried out as described in the previous section. Pressure wave transit times, and pressure history in the plenum and in the rocket cone were recorded by photographing oscilloscope traces of the transducer outputs.

In the double pulse experiments, the purpose of the first laser pulse is simply to generate a nozzle flow field for the second pulse that simulates what would be encountered in an RP thruster. As described above, the breakdown due to the first pulse creates an overpressure downstream of the throat which temporarily stops the flow from the stagnation chamber. Then, as the blast wave expands down the nozzle and the pressure decays sufficiently, the flow restarts and the nozzle refills. The extent to which the nozzle refills depends on the delay time to the subsequent laser pulse. Thus, at the time the second (or N^{th}) laser pulse enters the rocket, the region of the nozzle near the throat contains fresh, cold gas which has entered through the throat. However, the rest of the nozzle contains heated, low density gas left over from the previous pulse. It is this flow field situation which is modeled in Sec. 2. In the subsequent data analysis, experimental values of specific impulse and laser to propellant kinetic energy conversion efficiencies are derived from second pulse pressure transducer data.

Other experiments were carried out to determine the conversion efficiency of laser energy to blast wave energy. For these, only one laser was fired, either the XeF or the CO_2 laser, and the same measurement procedures were performed.

The experimental test matrix is given in Table 3.1. The time between laser pulses was varied from 30 to 100 μs. For the shortest time interval, the shock due to the deposition of CO_2 laser energy was still in the nozzle. The longest time delay was limited by signal to noise and the lower efficiency of converting deposited energy to directed kinetic energy. The time interval between laser pulses was controlled by a California Avionics digital time delay generator.

TABLE 3.1

Test Matrix of Laser Propulsion Experiments

$\Delta t(\mu s)$ / P (psig)	$\Delta t(\mu s)$ / $\dot{m}(g\text{-}s^{-1})$	30	40	60	80	100
50	0.96	2.88 E-5	3.84 E-5	5.76 E-5	7.68 E-5	9.60 E-5
75	1.32	3.96 E-5	5.28 E-5	7.92 E-5	10.6 E-5	13.2 E-5
100	1.55	4.65 E-5	6.20 E-5	9.30 E-5	12.4 E-5	15.5 E-5
125	1.89	5.67 E-5	7.56 E-5	11.3 E-5	15.1 E-5	18.9 E-5
150	2.22	6.66 E-5	8.80 E-5	13.3 E-5	17.8 E-5	22.2 E-5

Footnote: Numbers in the test matrix indicate mass of propellant (in grams) heated by the XeF laser pulse. The propellant used for the above experiment was argon.

3.4   Experimental Results and Data Reduction

3.4.1 Data Reduction and Error Analysis

Representative oscilloscope records for the measurements of the XeF laser energy, pressure in the plenum, and shocks in the nozzle are shown in Figs. 3.3a, b, and c.

Peak-voltage shown in Fig. 3.3a is proportional to the XeF energy output reflected from the quartz window. The sensitivity of Lumonics 50D calorimeter is 0.39 volt/J and 20% of the XeF laser beam fell outside of the calorimeter, thus the XeF energy output is given by

$$E(J) = 12.5 \times \frac{V}{0.39} \times 1.25 , \qquad (3.4.1)$$

where V is the observed peak-voltage shown in Fig. 3.3.

Pressure history in the plenum shown in Fig. 3.3b indicates that after the solenoid valve opened, the pressure reaches steady state; a large spike which appeared at 17 ms shows the time that the CO_2 and the XeF lasers were fired. The steady state pressure in the plenum determines the argon mass flow rate through the 1 mm diameter throat, which is given by

$$\dot{m} = \rho^* u^* A^* \qquad (3.4.2)$$

$$= P(atm)(0.2387)$$

where ρ^* is the propellant density in the throat, u^* is the sonic velocity of argon, and A^* is the nozzle throat area. Mass introduced into the nozzle between the laser pulses, Δm is given by

$$\Delta m = \dot{m} \cdot \Delta t , \qquad (3.4.3)$$

where Δt is the time between the two laser pulses. Equation (3.4.3) is an upper limit to the expelled mass since it assumes that the propellant flow restarts to the steady state value immediately after the CO_2 laser was fired. Calculations carried out using the flow simulation code described in Sec. 2.2 suggest that, in fact, for the conditions of the experiment, flow from the plenum may not restart for approximately 3 microseconds. Thus, for laser interpulse times $\gtrsim$ 30 microseconds, the error inherent in using Eq. (3.4.3) is less than 10%.
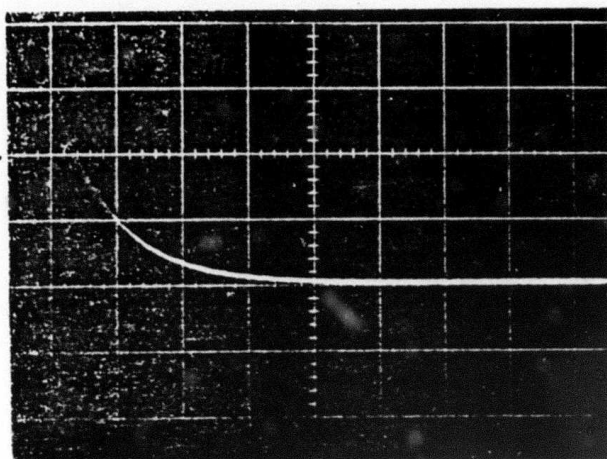
(a)
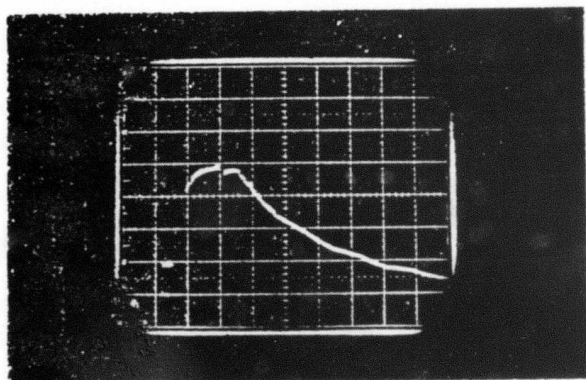
(b)
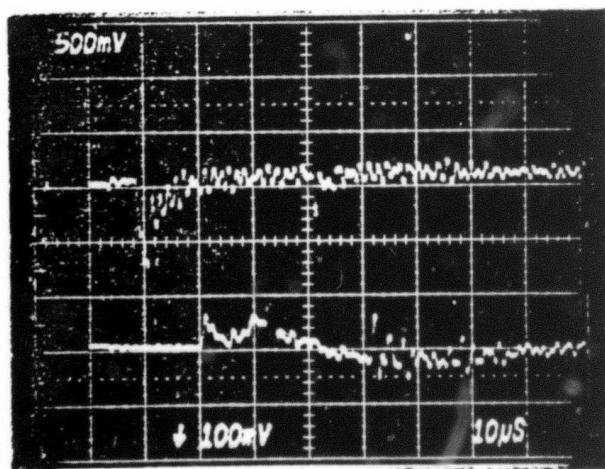
(c)
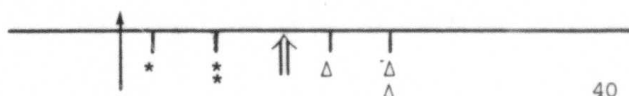
Fig. 3.3 Representative oscilloscope records of the XeF laser energy measurement (-a), the pressure history in the plenum (-b), and the laser-induced shock wave measurement (-c). (a) 50 ms/div, 50 mV/div: (b) 10 ms/div 100 mV/div; discontinuity on the plateau region indicates the time when the CO_2 and the XeF lasers were fired: (c) 10 μs/div, upper 500 mV, lower 100 mV/div, respectively; ↑ indicates the CO_2 laser firing; * and ** indicate the arrival of the CO_2 laser-induced blast wave at the first and second pressure transducer station, respectively; ⇑ indicates the XeF laser firing; Δ and Δ̿ indicate the arrival of the XeF laser-induced shock wave at the first and second pressure transducer station, respectively.

40

In Fig. 3.3c, the following events were identified as shown with signs:
(1) the time the CO_2 laser was fired (↑); (2) the arrival of the CO_2 laser-induced blast wave at the first station (*) and at the second station (⁑);
(3) the time the XeF laser was fired (30 μs after (1))(⇑); (4) the arrival of
the XeF laser-induced shock wave at the first (Δ) and second stations (Δ̂).

The CO_2 (or XeF) laser energy deposited in the steady state flow of
argon is given by

$$E(J) = \frac{0.4142 * P(atm) * \{X(cm)\}^{4.38}}{\{t(\mu s)\}^{3.38}} \qquad (3.4.4)$$

where P(atm) is the pressure in the plenum, x(cm) is the distance between the
breakdown point and the piezo pressure transducer stations, and t(μs) is the
transit time from the end of the breakdown to the arrival of the blast wave at
each pressure transducer station. The derivation of formula 3.4.4 is in Ref.
3.1. Also, for experiments carried out in stationary air, the laser energy de-
posited in the rocket cone is given in terms of pressure by

$$E(erg) = 2.41 \times 10^{-3} \times P^{1.5144} \qquad \text{at the first piezo pressure} \qquad (3.4.5)$$
$$\text{transducer station}$$

or

$$E(erg) = 2.83 \times 10^{-2} \times P^{1.5144} \qquad \text{at the second piezo pressure} \qquad (3.4.6)$$
$$\text{transducer station}$$

where P is the observed pressure jump from the pre-shock condition (in dyne
cm^{-2}). The derivation of these equations is given in Sec. 2.2.

The laser-induced propellant exhaust velocity, averaged over the two
piezo pressure transducer stations, was obtained by measuring a transit time
between the two pressure spikes as shown with Δ and Δ̂ in Fig. 3.3c. This anal-
ysis was only applied to the second laser heating pulse.

Similarly the exhaust kinetic energy of the propellant was taken to be

$$K.E. = \frac{1}{2} \Delta m \cdot v^2 \qquad (3.4.7)$$

where v is the average propellant exhaust velocity (as described above) and Δm is the mass expelled between the first and second laser pulses. Specific impulse is taken to be V/g where g is the gravitational constant.

Since the events of interest in the rocket cone take place on a time scale comparable to the response time of the piezo pressure transducers, and over distances comparable to the transducer diameters and uncertainties in the breakdown location, it is important to estimate the maximum errors incurred in the experiments. A sample error analysis of the data in Fig. 3.3c is given below.

Using Eq. (3.4.4) the maximum error in determining the CO_2 laser-induced blast wave energy is given by

$$\Delta E_{max} = 0.4142 \times \left\{ \frac{4.38 \, Px^{3.38}}{t^{3.38}} \; \Delta x + \frac{3.38 \, Px^{4.38}}{t^{4.38}} \; \Delta t + \frac{x^{4.38}}{t^{3.38}} \cdot \Delta P \right\}$$

$$= 0.4142 \times \{2.12 + 3.17 + 0.74\} \qquad (3.4.8)$$

where P = 10.1 atm, t = 16 μs, and x = 9.3 cm and Δx, Δt, and ΔP are taken to be 0.3 cm, 1.0 μs, and 0.5 atm. Then, the absolute value of ΔE is given by 2.5 J, which corresponds to a $\pm$ 40% error. As seen in Eq. (3.4.8), the accuracy of measuring the laser energy deposited in the propellant was limited primarily by the response time of the piezo pressure transducer and the uncertainty of the precise breakdown location in the rocket cone. Similarly the maximum error in the determination of the propellant kinetic energy resulting from the second laser pulse is given by

$$\Delta E_{MAX}^{K.E.} = \frac{0.2387}{2} \left\{ 2P*t^{delay}*\frac{x}{t^2} \cdot \Delta x + t^{delay}*\frac{x^2}{t^2} \cdot \Delta P + 2P*t^{delay}*\frac{x^2}{t^3} \cdot \Delta t \right.$$

$$\left. + P \frac{x^2}{t^2} \cdot \Delta t^{delay} \right\} \qquad (3.4.9)$$

$$= \frac{0.2387}{2} \left\{ 8.38 \times 10^6 + 3.51 \times 10^6 + 2.23 \times 10^7 + 2.36 \times 10^6 \right\}$$

where x = 5.08 cm, P = 10.1 atm, t = 10.5 μs, and t^{delay} = 30 μs and Δt^{delay} = 1 μs, Λx = 0.3 cm, ΔP = 0.5 atm, and Δt = 1.5 μs. Then, the absolute value of ΔE is given by 0.43 J, which corresponds to ± 50%. As seen in Eq. (3.4.9), the biggest errors arise from the finite dimension of the piezo pressure transducer head and uncertainties in the transit time measurements. As is illustrated above, the systematic errors associated with the present measurements are significant, i.e., ± 40% for the blast wave energy, ± 50% for the exhaust kinetic energy, and ± 20% for the specific impulse (average propellant exhaust velocity). To reduce these errors, improved diagnostic techniques are needed that have improved spatial and temporal resolution.

3.4.2 Data for Energy Conversion of Laser Energy to Blast Wave Energy

Typical oscilloscope records of the blast wave measurement in stationary 1 atm air using the CO_2 and the XeF lasers are shown in Figs. 3.4a and b, respectively. For these experiments, the conversion of laser energy to blast wave energy was obtained by measuring the elapsed time from breakdown to the arrival of the blast wave at each station and measuring the pressure jump at each station. Equations (3.4.5), and (3.4.6) were used for the derivation of the blast wave energy. The experimental results are shown in Table 3.2.

Figures 3.5a and b show typical oscilloscope traces used to determine the conversion efficiency of XeF laser energy into blast wave energy in an argon flow. In these experiments, only the transit time from breakdown to the arrival of the blast wave at the second station was employed for the calculation of the conversion efficiency. The conversion efficiencies achieved using the CO_2 and the XeF lasers are plotted as a function of mass flow rate in Figs. 3.6 and 3.7. It is seen that for the range of mass flow rates investigated the coupling of the CO_2 laser (10.6 μm) beam with argon gas is relatively independent of the flow rate while the coupling of the XeF laser (0.35 μm) beam appears to increase with flow rate. Nevertheless, for mass flow rates ≳ 1.0 g/s, both lasers appear to be converted to propellant blast wave energy with an efficiency ≈ 50 ± 20%.

(b)

(a)
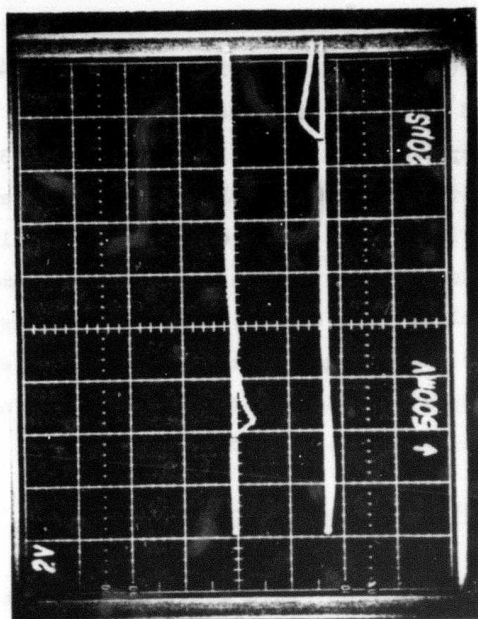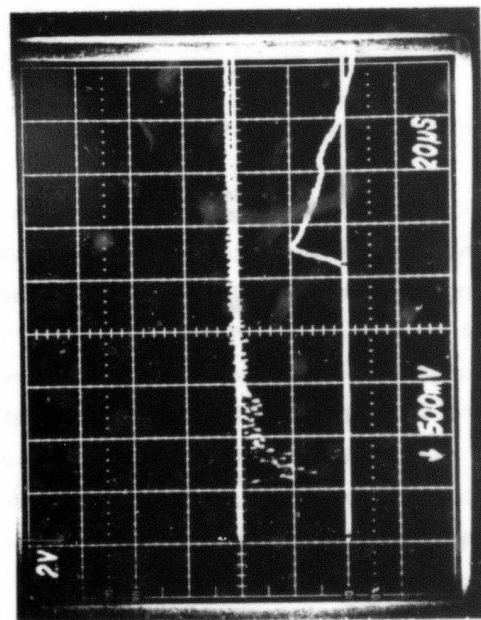
Fig. 3.4 Blast wave measurement in 1 atm air using the CO_2 TEA laser (a) and the XeF laser (b). (a) Pressure profiles at the first and the second pressure transducer stations, respectively. Beginning of oscilloscope trace corresponds to firing of the laser: 20 µs/div; upper trace - 2 V/div; lower trace - 500 mV/div. (b) The XeF laser-induced blast wave measurement: 20 µs/div; upper trace - 2 V/div; lower trace - 500 mV/div.

TABLE 3.2

Comparison of Two Different Types of Blast Wave Energy Conversion
Measurements Using the CO_2 and the XeF Lasers (in Stationary Air)

	Observed Energy (J) and Conversion Efficiency (%) of the CO_2 Laser			
	From Transit Time		From Pressure Jump	
x = 4.3 cm	4.41 J	48%	6.49 J	70%
x = 9.3 cm	3.42 J	37%	5.19 J	56%

	Observed Energy (J) and Conversion Efficiency (%) of the XeF Laser			
	From Transit Time		From Pressure Jump	
x = 4.3 cm	0.677 J	38%	0.974 J	55%
x = 9.3 cm	0.832 J	47%	1.27 J	72%
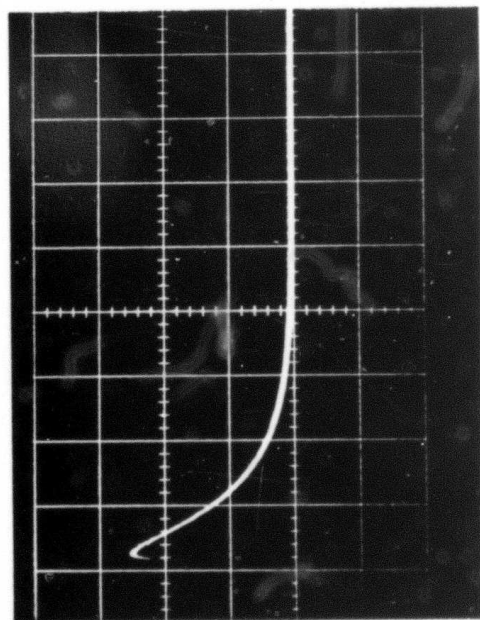
(a)
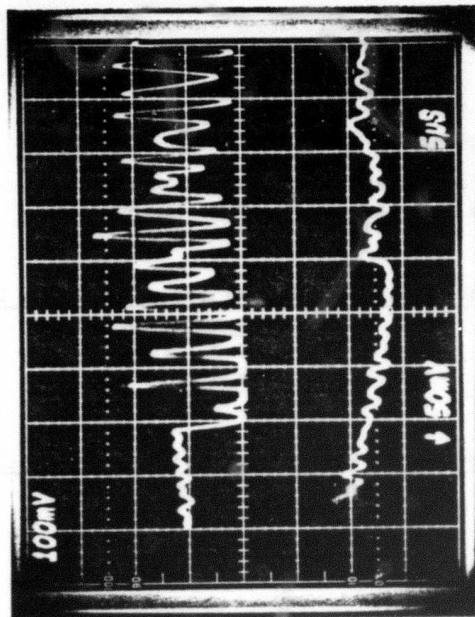
(b)

Fig. 3.5 Blast wave energy measurement in argon using the XeF laser. (a) XeF laser output energy measurement: 10 ms/div; 50 mV/div. (b) Transit time measurement of the XeF laser-induced blast wave; 5 μs/div; upper trace – 100 mV/div; lower trace – 50 mV/div, * and * indicate the arrival of blast wave at the first and second stations, respectively.
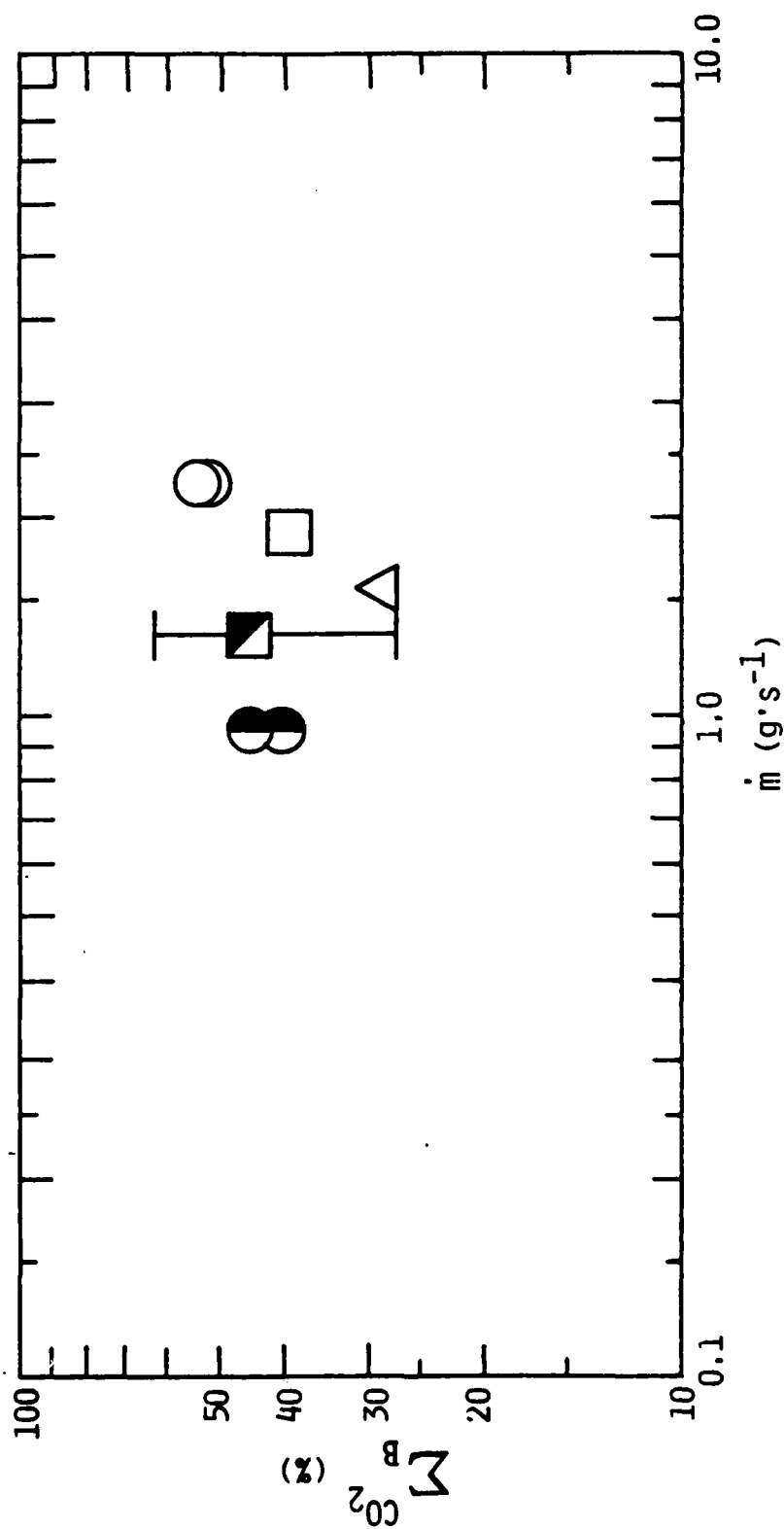
Fig. 3.6 Conversion efficiency of the CO$_2$ laser (10.6 μm) energy to blast wave energy versus argon mass flow rate through the nozzle. Error bar indicates the maximum error incurred in experiments, evaluated using equation (3.4.6).
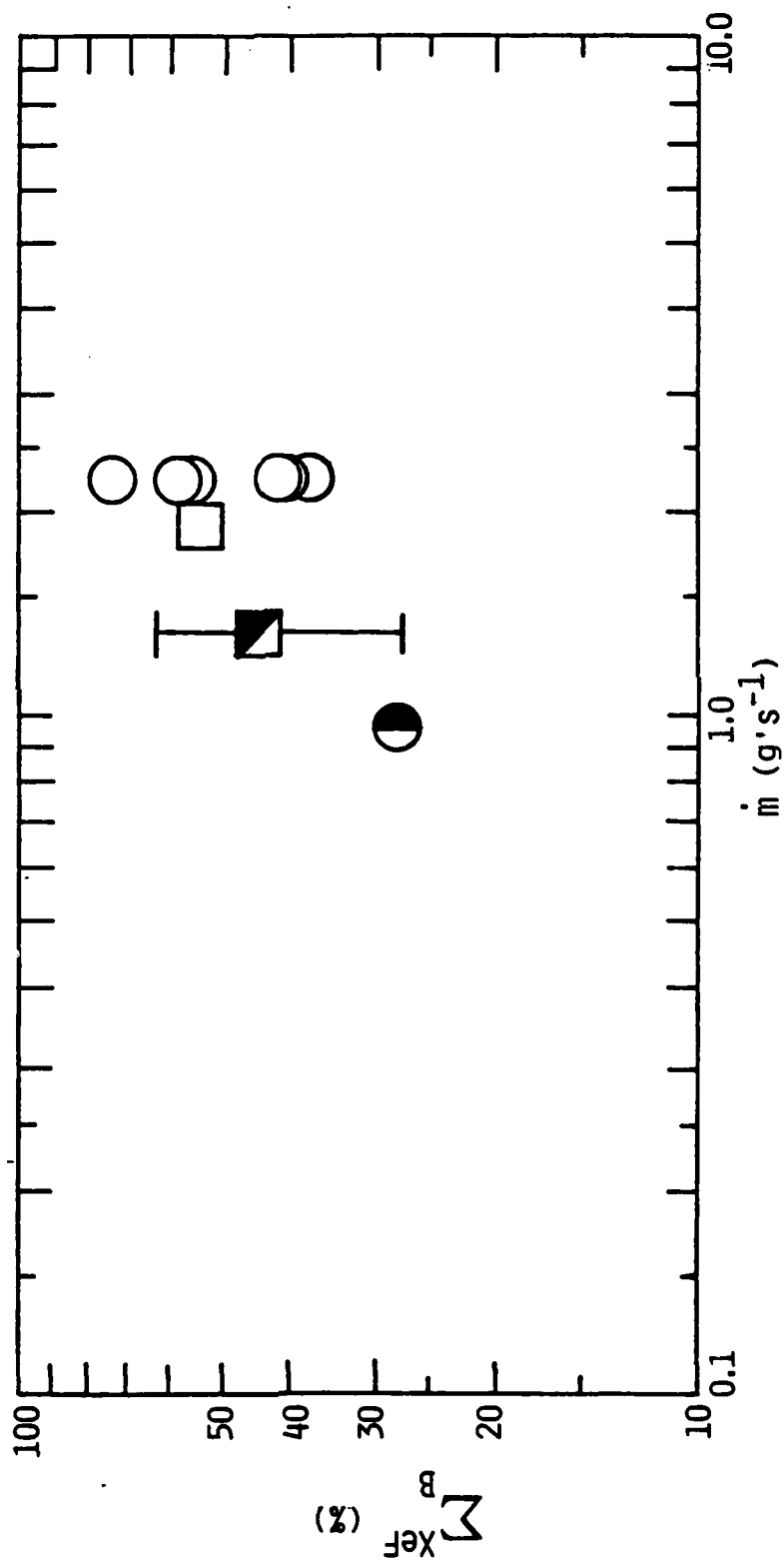
Fig. 3.7 Conversion efficiency of the XeF laser (0.35 μm) energy to blast wave energy versus argon flow rate through the nozzle. Error bar indicates the maximum error incurred in experiments, evaluated using Eq. (3.4.3).

3.4.3 Data for Conversion Efficiency of Laser Energy to Gas Kinetic Energy Using Two Laser Pulses - Determination of Specific Impulse

Typical oscilloscope records of the measurements used to determine propellant kinetic energy were shown in Figs. 3.3a, b and c. The propellant kinetic energy appearing in the exhaust is calculated using Eq. 3.4.7 with the propellant exhaust velocity determined from transit time measurements of the propellant pressure wave induced by the second laser pulse (XeF laser). The reduced data are plotted in Figs. 3.8-3.12 as the conversion efficiency of laser energy to propellant kinetic energy vs. propellant mass. The propellant mass plotted is the mass expelled between the first and second laser pulses, i.e., $\dot{m} \Delta t$, where Δt is the laser interpulse time. For these experiments, the XeF laser energy entering the rocket was typically 2.6 J.

In Fig. 3.13, we plot the average conversion efficiency achieved vs. argon mass flow rate. For each mass flow rate, the conversion efficiency plotted represents an average for the various laser interpulse times studied. As can be seen, for mass flow rates $\gtrsim$ 1.6 g/s, the conversion efficiency is relatively independent of mass flow rate and appears to take on an average value of 25 to 30%.

From Figs. 3.8 through 3.12 it can be seen that specific impulse of up to 500 s was achieved in argon propellants heated by the pulsed XeF (0.35 μm) laser. Furthermore, this specific impulse was obtained with conversion efficiencies of laser energy to propellant kinetic energy of up to 30 to 50%. These results compare favorably with similar results that were presented in Ref. 3.1 for argon propellants processed by two successive 10.6 μm laser pulses. In the latter studies, maximum specific impulses of 500 s in argon and 1000 s in hydrogen were achieved with conversion efficiencies of laser energy to exhaust kinetic energy of up to 40 to 50%.

Since in both the previous studies[3.1] and the present work, the maximum specific impulse achieved in argon was 500 seconds, the question arose as to whether this represents a fundamental physical limit in argon. However,
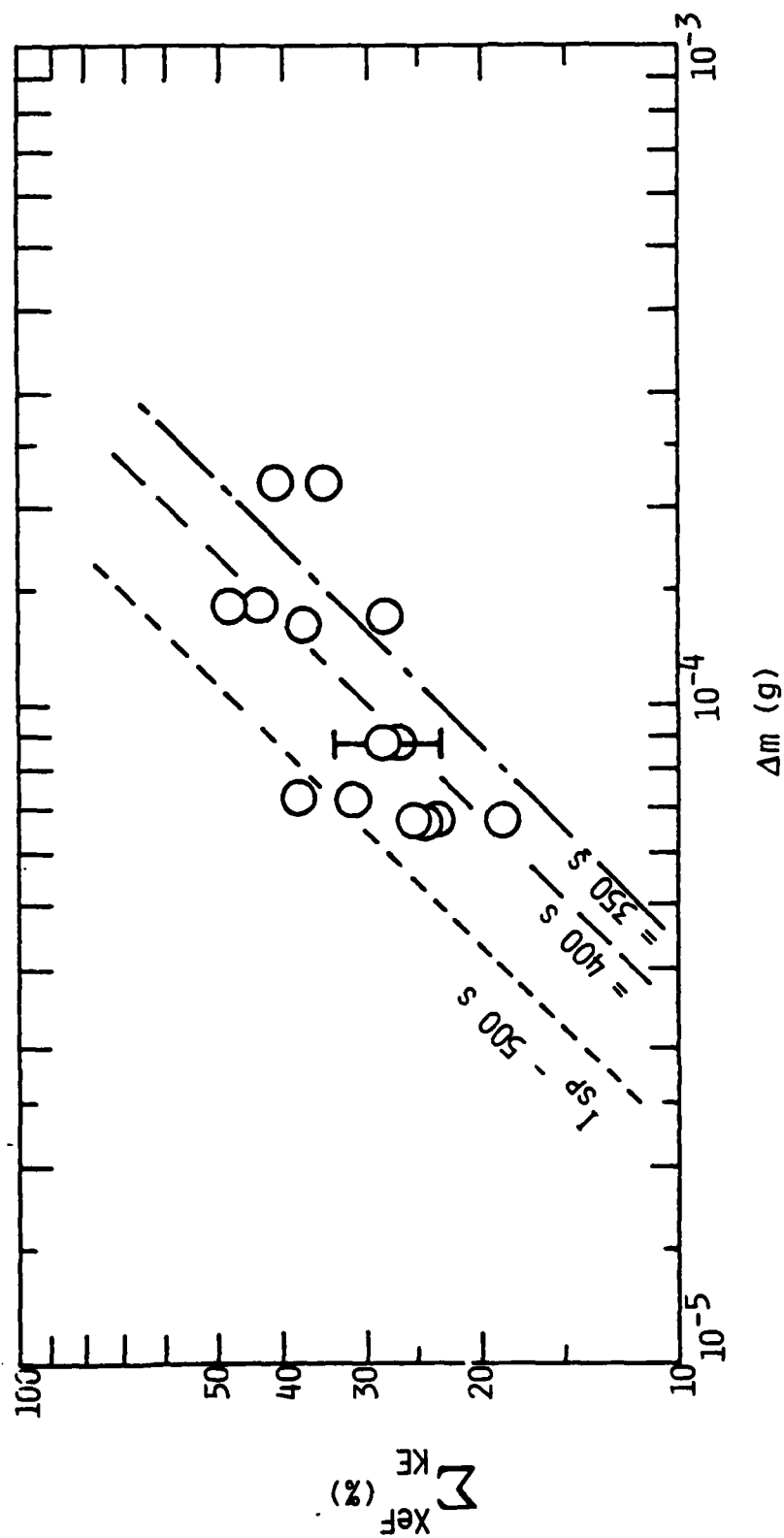
Fig. 3.8 Gas kinetic energy conversion efficiency versus mass with argon mass flow rate of 2.22 g/s. Dashed lines correspond to $I_{sp}(s)$ = 500 (———), 400 (— —), 350 (— · —) with XeF energy of 2.6 J. Error bar indicates the maximum error incurred in experiment, which was evaluated using Eq. (3.4.9).

50
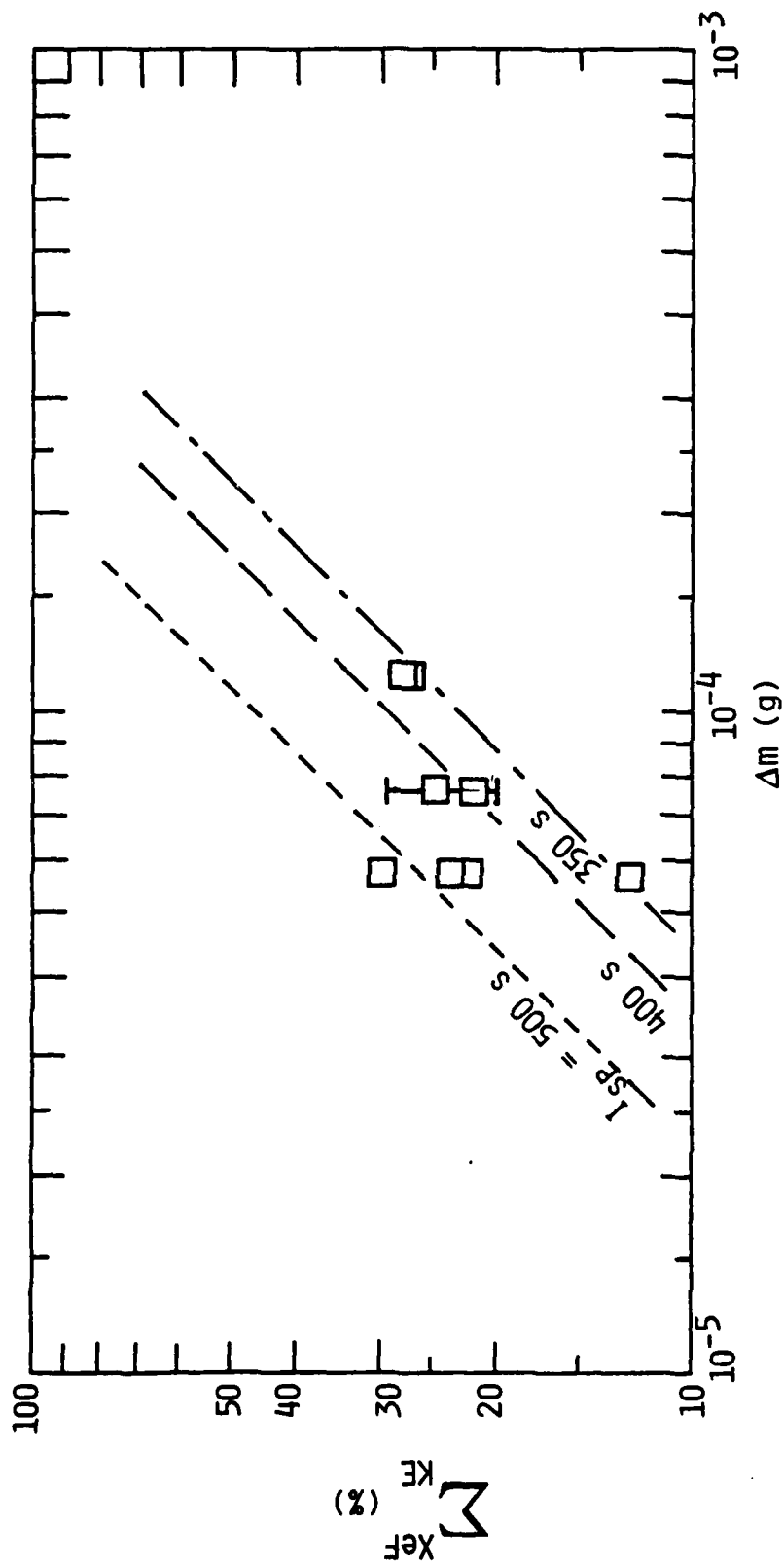
Fig. 3.9 Gas kinetic energy conversion efficiency versus mass with argon mass flow rate of 1.89 g/s. Dashed lines correspond to $I_{sp}(s) = 500$ (—--), 400 (— —), 350 (—·—) with the XeF energy of 2.6 J. Error bars indicate the maximum error incurred in experiment, which was evaluated using Eq. (3.4.9).

51

5514-10
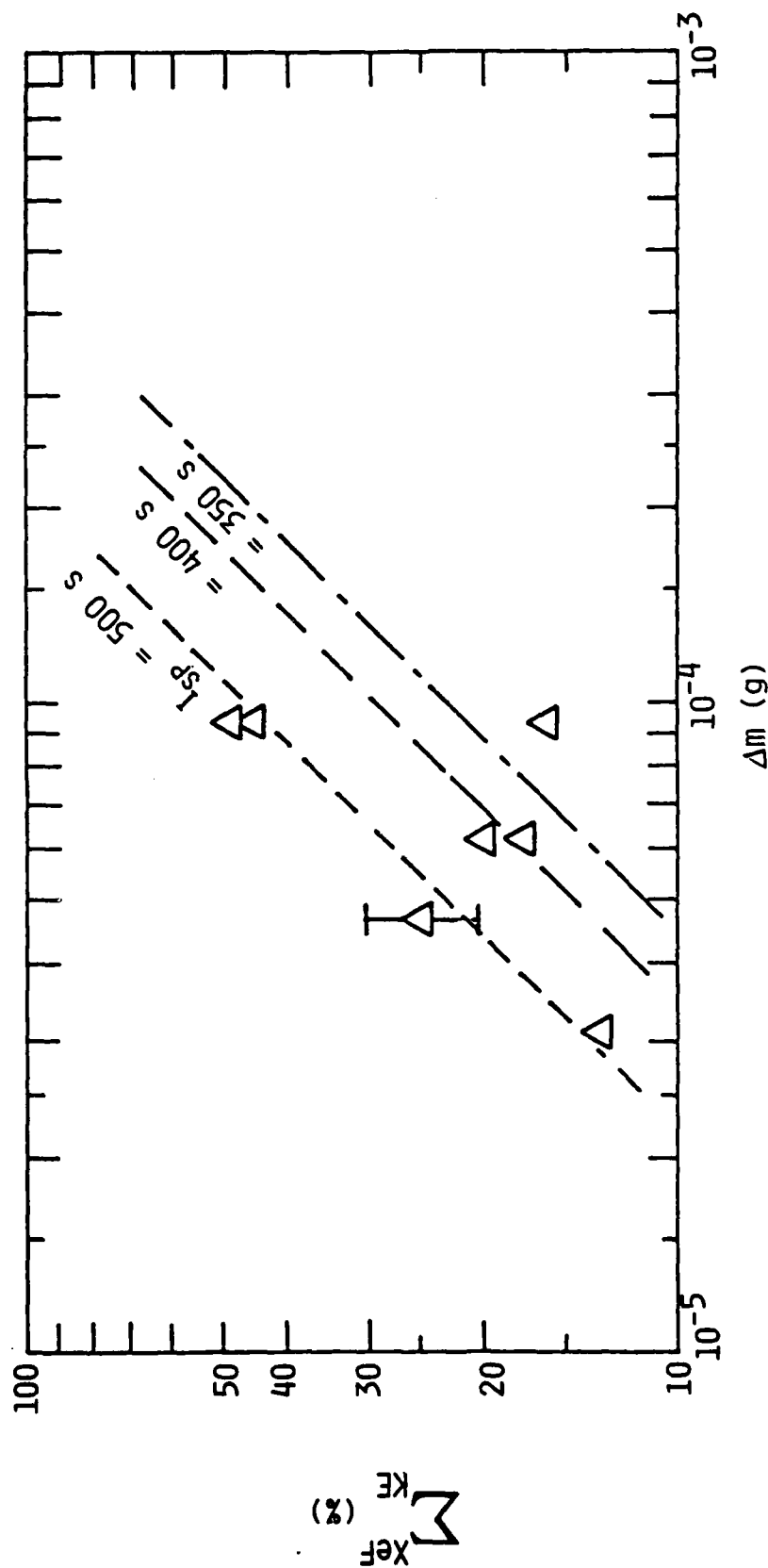
Fig. 3.10 Gas kinetic energy conversion efficiency versus mass with argon mass flow rate of 1.55 g/s. Dashed lines correspond to $I_{sp}(s) = 500$ (–––), 400 (— —), 350 (—·—) with the XeF energy of 2.6 J. Error bar indicates the maximum error incurred in experiment, which was evaluated using Eq. (3.4.9).

52
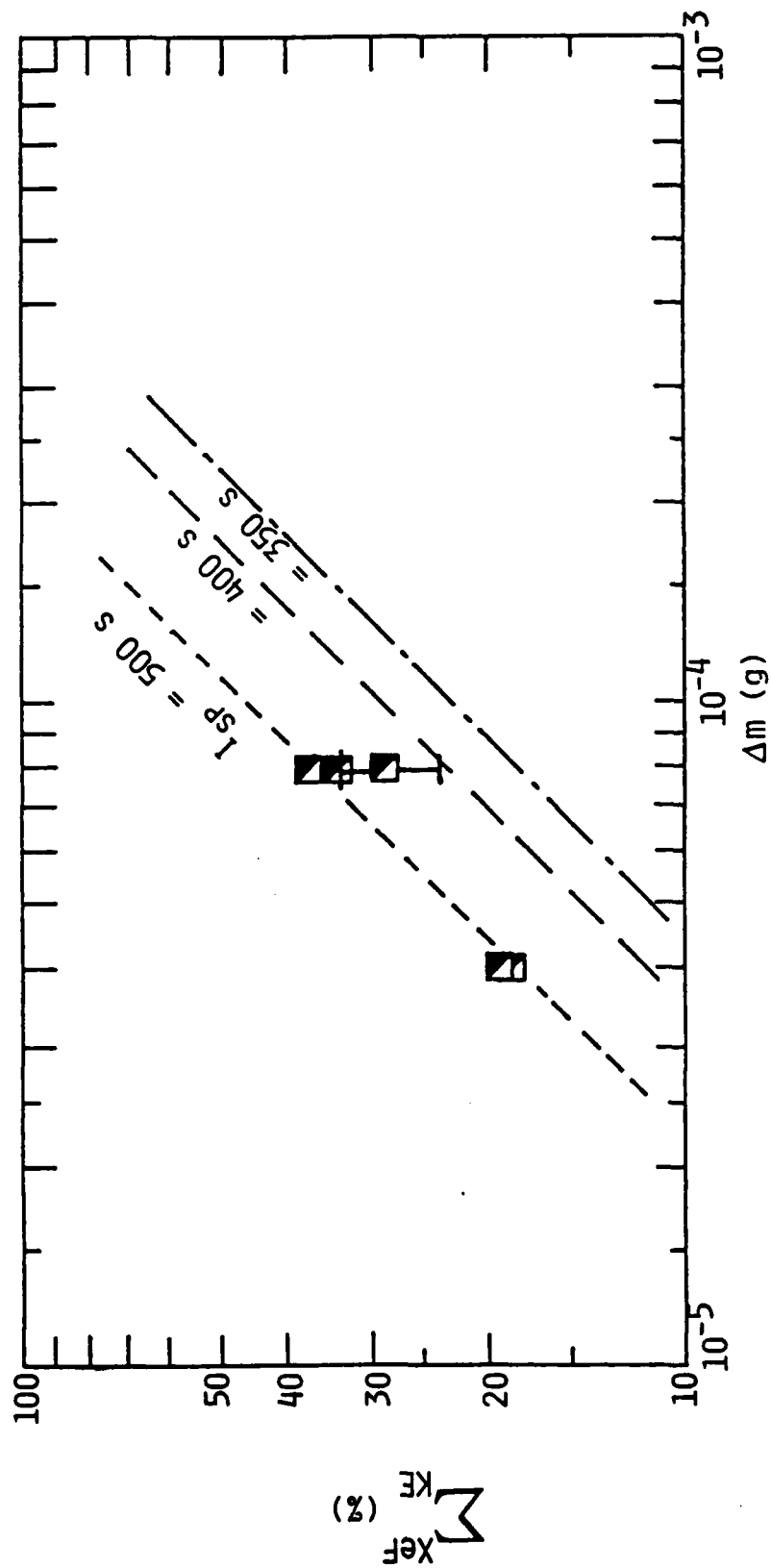
Fig. 3.11 Gas kinetic energy conversion efficiency versus mass with argon mass flow rate of 1.32 g/s. Dashed lines correspond to $I_{sp}(s)$ = 500 (———), 400 (———), 350 (—·—) with XeF energy of 2.6 J. Error bar indicates the maximum error incurred in experiment, which was evaluated using Eq. (3.4.9).
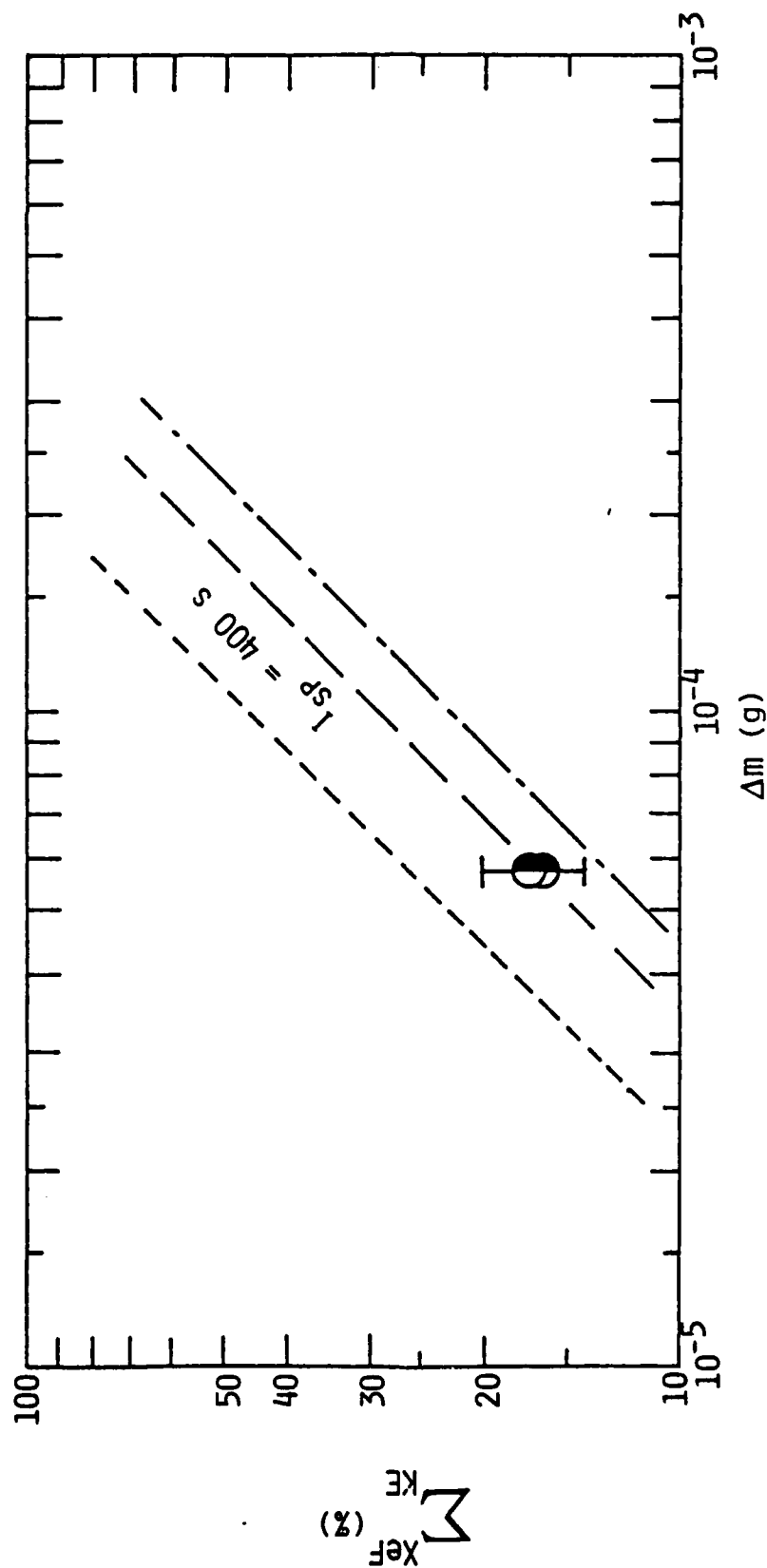
Fig. 3.12 Gas kinetic energy conversion efficiency versus mass with argon mass flow rate of 0.96 g/s. Dashed lines correspond to $I_{sp}(s) = 500$ (—–—), 400, (——), 350 (—·—) with the XeF energy of 2.6 J. Error bar indicates the maximum error incurred in experiment, which was evaluated using Eq. (3.4.9).
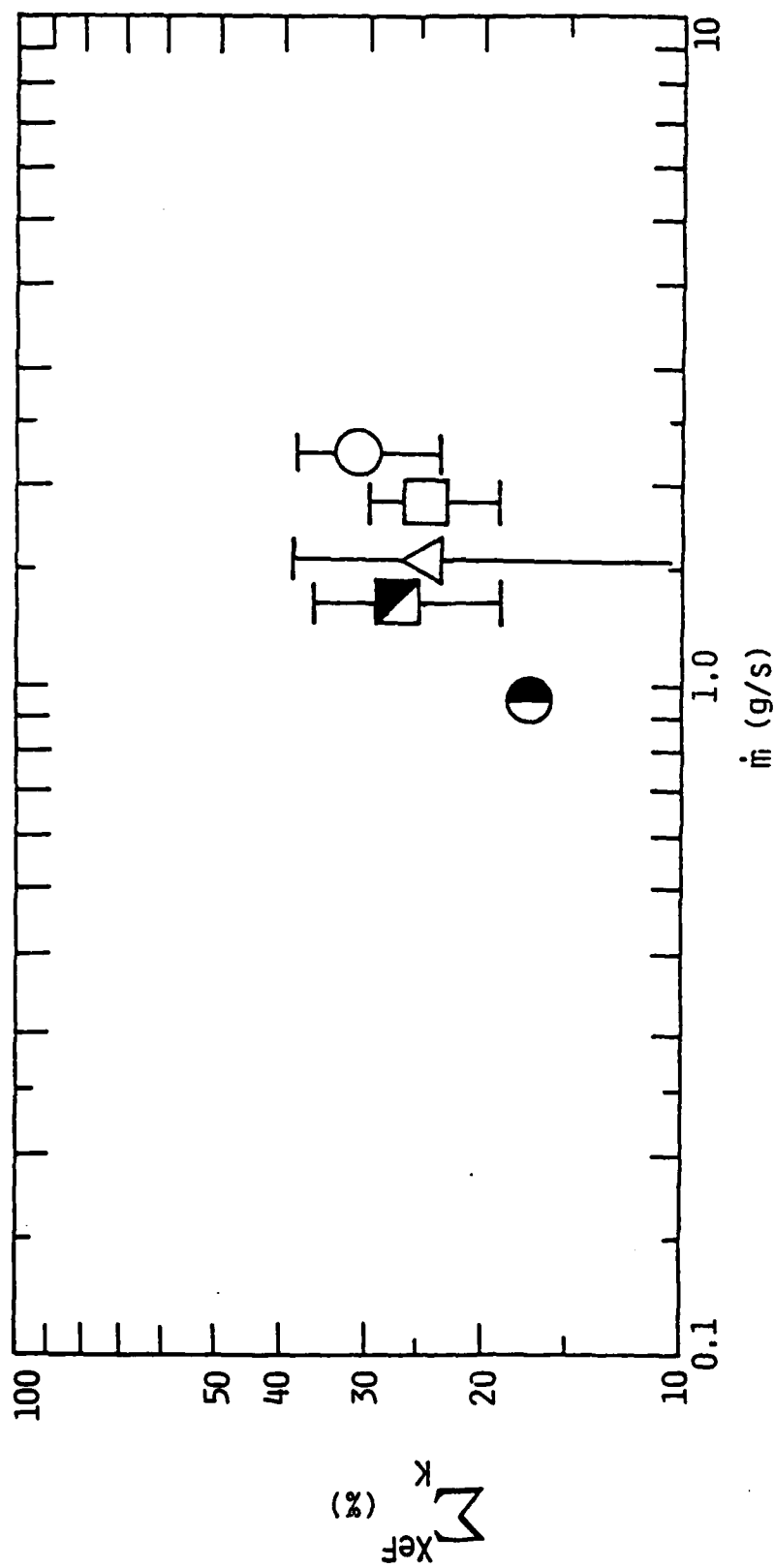
Fig. 3.13 Summary of efficiencies achieved for conversion of XeF laser energy into kinetic energy of argon propellant. Results are plotted as a function of propellant mass flow rate. Error bars correspond to 1 σ of standard deviation.

because the earlier experiments were performed with a nozzle geometry signifi-
cantly different from the present one, i.e., a rapidly expanding paraboloid
vs. the present 10° cone, it was difficult to draw any strong conclusions.
Thus, it was decided to perform two pulse experiments in the conical nozzle in
which both the first and second pulses were CO_2 laser pulses. In principle
this would allow direct comparison of 0.35 μm and 10.6 μm performance under
the same nozzle conditions, as well as comparisons of the performance of the
parabolic and conical nozzles under the same conditions.

In Fig. 3.14 we plot the specific impulse data obtained for two 10.6
μm laser pulses heating argon propellant in the conical nozzle. As was de-
scribed above, the specific impulse is determined from transit time measure-
ments of the nozzle pressure waves induced by the second laser pulse. The
data of Fig. 3.14 are plotted as the specific impulse observed vs. Δm, the
propellant mass heated by the second CO_2 laser pulse. As before, we have
taken Δm to be equal to $\dot{m}\Delta t$, where Δt is the time delay used between laser
pulses. The diagonal lines plotted with the data represent loci for different
values of exhaust kinetic energy, i.e., $E_K = 1/2 \, \Delta m V^2 = 1/2 \, \Delta m (g I_{sp})^2$. As can
be seen, the maximum specific impulse achieved in these experiments was ap-
proximately 700 s. For a propellant mass of ≈ 5×10^{-5} grams, this value of
specific impulse indicates a maximum exhaust kinetic energy of ≈ 1.2 J. With
the total CO_2 laser energy entering the rocket being approximately 6.5 J, this
corresponds to a kinetic energy conversion efficiency of 18.5%. It is inter-
esting to note that a specific impulse of 700 s in argon is 40% higher than
any of the previous results. Comparing conical nozzle results only, this im-
proved performance is probably due to the higher laser energy available at
10.6 μm vs. 0.35 μm, i.e., 6.5 J vs. 2.7 J. Presumably similar results could
be obtained with an XeF laser if the laser energy were increased.

Based upon the most simple arguments, the specific impulse is expected
to scale as ~ $\sqrt{E_{laser}}$. We see that this is not quite the case when we compare
the specific impulse obtained using the CO_2 laser and that achieved with the
XeF laser. From the ratio of the available laser energies, ~ 6.5/2.7, the

56

Fig. 3.14 Specific impulse data obtained for argon propellant heated by two CO_2 TEA laser pulses. Specific impulse is determined from transit time measurements of pressure wave induced by 2nd laser pulse. Dashed lines plotted with data indicate loci of constant propellant kinetic energy ($\frac{1}{2} \Delta m (g\, I_{sp})^2$). Δm is the mass expelled through throat between first and second laser pulses.

above argument would lead us to predict a specific impulse improvement of 55%. The observed improvement was only 40%. It is clear that in future studies it would be worthwhile to investigate how the achievable specific impulse varies with input laser energy.

It is also interesting to note the higher specific impulse achieved with the present conical nozzle compared to the previous parabolic nozzle. We believe the improved performance results from conditions in the conical nozzle being more conducive for efficient laser energy deposition. Apparently, at the lower mass flow rates, the very rapid initial divergence of the parabolic nozzle leads to downstream gas densities that are too low to support strong LSD wave absorption.

Finally, measurements similar to those presented for argon in Fig. 3.14 were also obtained for hydrogen propellants. The results are given in Fig. 3.15. Note the significant increase in specific impulse that occurs when hydrogen is used, i.e., up to 3000 seconds in hydrogen vs. a maximum of 700 seconds in argon. Qualitatively, this result is not surprising in light of the much lower molecular weight of hydrogen. In fact, for specific impulse scaling as the inverse square root of molecular weight (assuming constant stagnation temperature), an increase of $\sqrt{40/2} \approx 4.5$ is expected. The observed improvement is a factor of ~ 4.3.

Comparing the results in Figs. 3.14 and 3.15 we also note that the conversion efficiency of laser energy to propellant kinetic energy is considerably higher in hydrogen than in argon. In fact, at maximum specific impulse, the conversion efficiency achieved in hydrogen appears to be approximately four times greater than in argon, i.e., $\sim 74\%$ vs. $\sim 19\%$ in argon. Because the data in Fig. 3.6 indicate CO_2 laser energy deposition efficiencies in argon of 40 to 50%, it would appear that the low overall conversion to exhaust kinetic energy in this propellant is limited primarily by loss mechanisms other than imperfect absorption. Energy loss channels that are likely to be important are plasma radiation losses and losses to residual enthalpy of the exhaust gas.

58

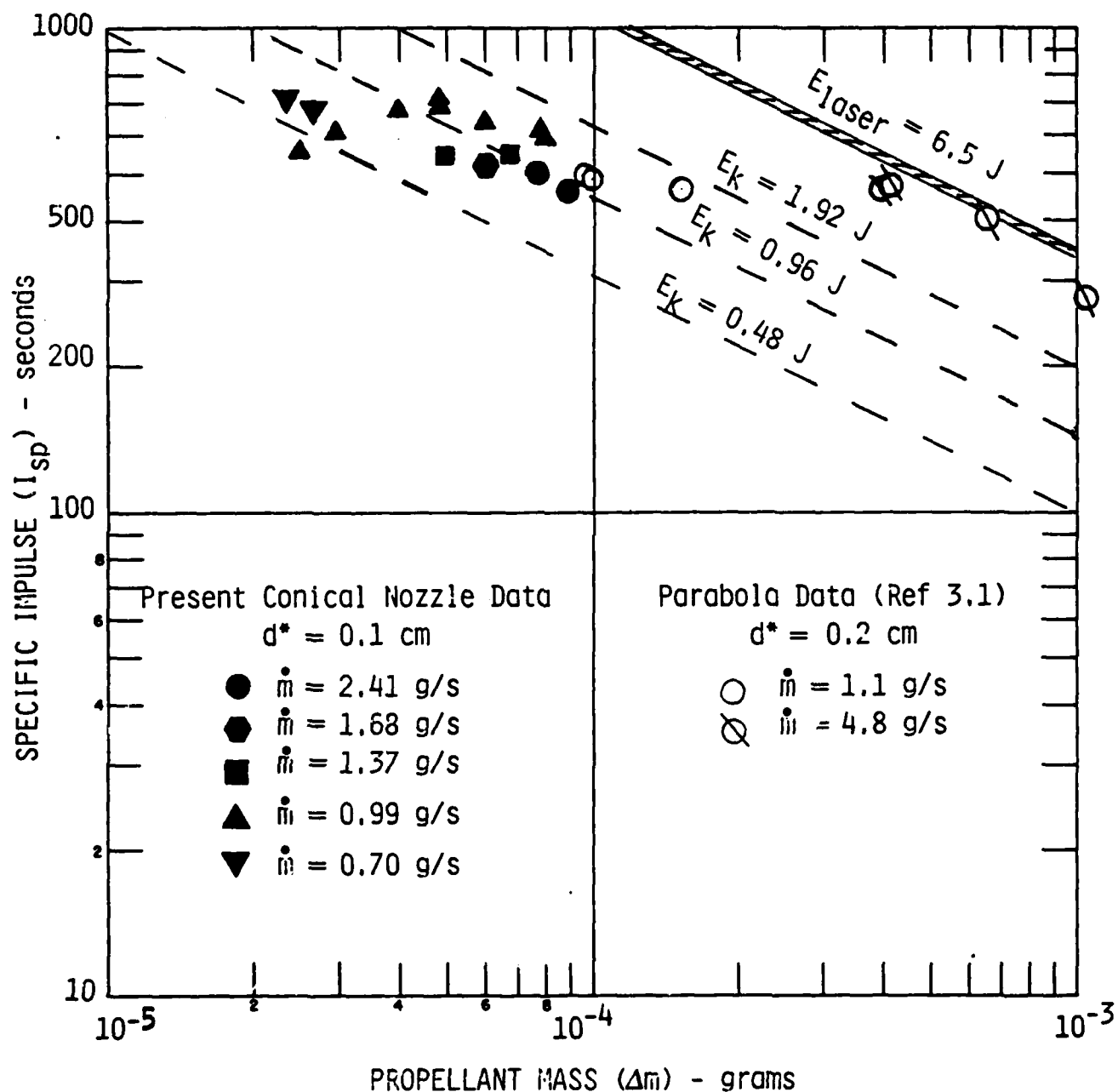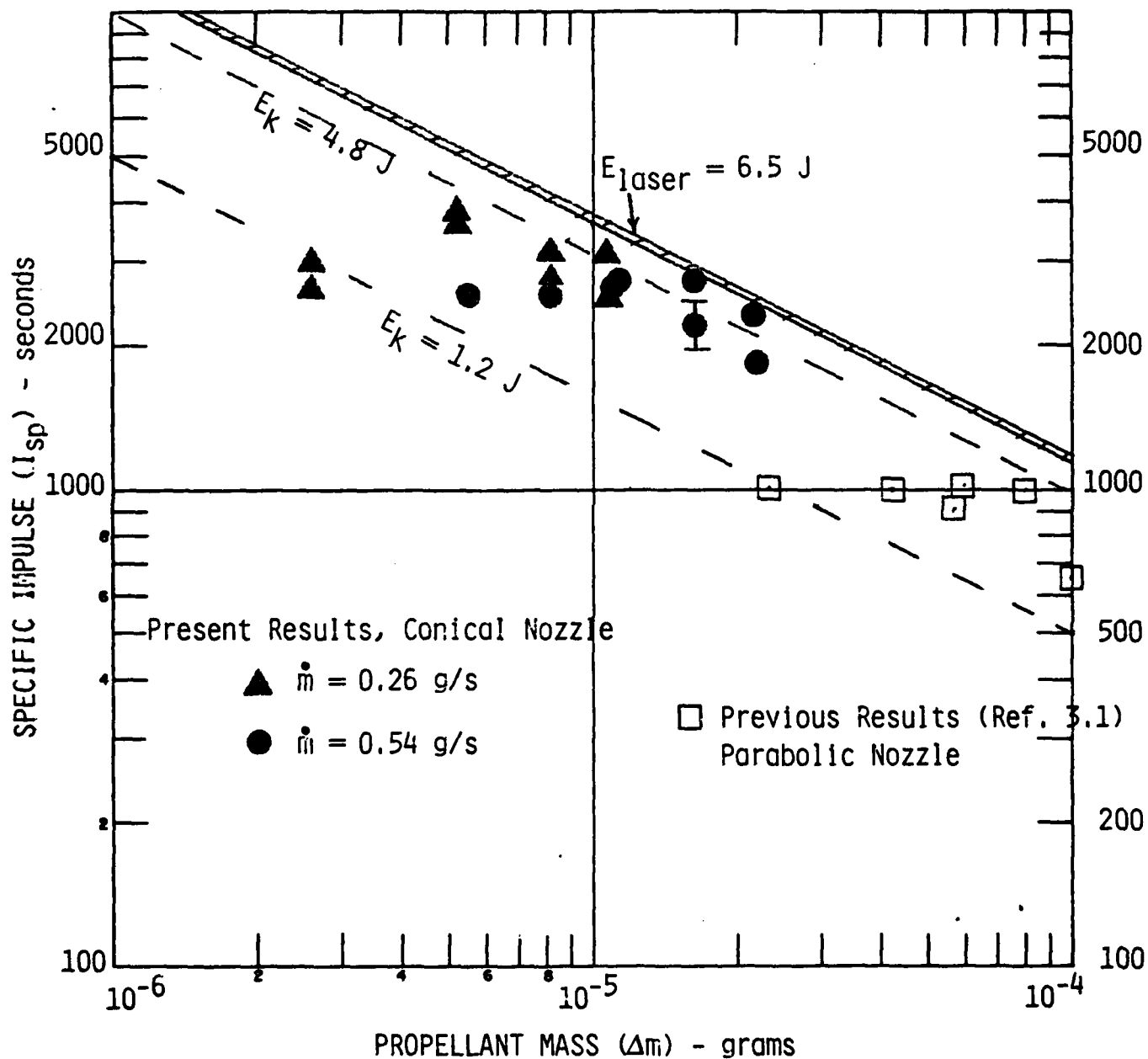Fig. 3.15 Specific impulse data obtained for hydrogen propellant heated by two CO_2 TEA laser pulses. Specific impulse is determined from transit time measurements of pressure wave induced by second laser pulse. Dashed lines are loci of constant propellant kinetic energy ($\frac{1}{2} \Delta m(g\ I_{sp})^2$). Δm is the mass expelled through throat between first and second laser pulses.

As was pointed out with the argon results, the present results for hydrogen using the conical thruster exhibit a significant improvement in performance over the previous results obtained with the parabolic nozzle.[3.1] In the latter experiments, the best performance obtained with hydrogen propellant was a specific impulse of 1000 seconds at a conversion efficiency of laser to exhaust kinetic energy of $\approx$ 40%. We believe the better performance achieved in the present investigations, i.e., 3000 seconds with conversion efficiencies up to $\approx$ 70%, is primarily the result of more efficient laser energy absorption in the conical thurster. In the previous parabolic thruster, the initial nozzle divergence was so large that attempts to increase specific impulse by reducing the amount of propellant mass heated led to nozzle gas densities that were too low to support efficient laser absorption.

3.5   Summary of Results and Conclusions

The results of the present thruster performance experiments can be summarized as follows:

(1) Using a conical nozzle of 10° half angle and external focusing optics the following rocket performance parameters have been achieved:

- Laser to blast wave energy conversion efficiencies in argon propellant of ~ 40 to 60%. Such energy deposition efficiencies were achieved using either a CO_2 TEA laser (λ = 10.6 μm, τ_p $\approx$ 3 μs, E_p $\approx$ 6.5 J) or a xenon fluoride excimer laser (λ = 0.35 μm, τ_p $\approx$ 0.6 μs, E_p = 2.7 J).

- Specific impulse in argon of 500 s using the XeF laser (E_p $\approx$ 2.7 J) and 700 s using the CO_2 laser (E_p $\approx$ 6.5 J). These specific impulses were achieved with corresponding conversion efficiences of laser energy to exhaust kinetic energy of up to 40% $\pm$ 10% and 19% $\pm$ 5%, respectively.

- A maximum specific impulse in hydrogen propellant (using the CO_2 laser as the heating source) of ~ 3000 seconds. This specific impulse was achieved with a conversion efficiency of laser to exhaust kinetic energy of up to ~ 70%.

For all the above experiments, specific impulse was determined from transit time measurements of the pressure wave induced by the second laser pulse in a two pulse heating sequence. Typical interpulse times were 20 to 100 μs.

(2) Performance obtained with the conical nozzle and CO_2 TEA laser pulses represents a significant improvement over similar experiments performed previously[3.1] using a parabolic nozzle. Previously the maximum specific impulse that could be obtained was 500 s in argon and 1000 s in hydrogen. This is to be compared to the present results of 700 s and 3000 s, respectively. The improvement is believed to result from better laser energy absorption that occurs in the conical nozzle when operating at low mass flow rates.

Based upon the experimental results described above, the following conclusions can be made:

(1) There appears to be no fundamental reason why pulsed laser-heated thrusters can not be operated efficiently at visible/UV laser wavelengths. The present results indicate conversion efficiencies of laser energy to propellant energy at $\lambda = 0.35$ μm that are comparable to those obtained for $\lambda = 10.6$ μm. The only significant question that remains with respect to wavelength scaling is whether, if a self-focusing nozzle is to be used, sufficient focusing can be achieved at the short wavelengths to achieve rapid laser-induced breakdown. Optical design considerations for a self-focusing nozzle are discussed in Sec. 4.

(2) It appears that the values of specific impulse that were obtained previously using a parabolic nozzle,[3.1] i.e., 500 seconds in argon and 1000 seconds in hydrogen, were limited by poor laser energy deposition at low propellant masses. Apparently, the very rapid initial divergence of that nozzle created downstream gas densities that were too low to efficiently absorb the incident laser radiation. In contrast, the present conical nozzle, with its 10° half angle divergence, eliminates this problem by maintaining higher gas density downstream of the throat. The most dramatic improvement is seen in the case of hydrogen for which the achievable specific impulse increased from 1000 seconds to some 3000 seconds. To achieve similarly high specific impulse in the parabolic nozzle will probably require operating at higher mass flow rates and with significantly larger laser pulse energies. Thus, for full scale operation, parabolic nozzles will probably not present a limitation to rocket performance.

(3) Finally, it is worth noting the similarity between the rocket performance parameters we have obtained for a pulsed laser-heated thruster and those typical of an arc-heated rocket engine. According to Refs. 3.2 and 3.3, arc-heated rocket engines typically operate with a specific impulse in the range of 400 to 2000 seconds and a maximum propellant temperature of $\sim$ 5500°C. The typical working fluid is hydrogen. The internal efficiency of such engines, i.e., fraction of electrical input energy converted to kinetic energy of ejected mass, is typically 15 to 20 percent, (but can probably be increased to some 50 to 60 percent if the propellant is used as a regenerative coolant). The similar performance observed for a pulsed laser-heated thruster is not surprising in light of the similarity of the propellant heating process, i.e., gas breakdown and plasma formation followed by a thermodynamic nozzle expansion.

3.6   Recommendations for Future Studies

Perhaps the most significant result of the present studies is the experimental evidence for achieving a specific impulse of some 2500 to 3000 seconds with hydrogen propellant. Unfortunately, because this result depends on a theoretical interpretation of the laser-induced pressure waves measured in the nozzle, its value is in question. For verification, additional experiments are required in which a more direct, reliable measurement of specific impulse is carried out. Ideally, a diagnostic technique is needed that can provide a measurement of exhaust gas velocity.

One approach which appears feasible (particularly for exhaust gas velocities in excess of 10^6 cm/s, i.e., $I_{sp} > 1000$ seconds) is to measure the Doppler shift of spectral line emissions emanating from the exhaust. In hydrogen, a good spectral line to monitor might be the well-known red line, Hα, of the atomic hydrogen Balmer spectrum. For particle velocities of 3×10^6 cm/s ($I_{sp} \approx 3000$ seconds), the Doppler shift would be $^Vp/c$ or 1 part in 10^4. High resolution spectrometers are readily available which can resolve 1 part in 10^5.

More reliable measurements of rocket performance would also be made possible by performing longer duration laser tests. Sufficient test time

could enable the use of standard rocket diagnostic instrumentation such as
load cells, thrust stands, strain gauges, ballistic pendula, etc. Of course,
to obtain specific impulse from measurements of thrust and total impulse re-
quires that the propellant mass flow rate and total expelled mass be known ac-
curately.

Finally, independent of performing any new experiments, the existing
experimental data should be analyzed in greater detail through use of the com-
puter simulation code described in Section 2. Using the multiple pulse code
with time dependent laser absorption and real gas thermodynamics, calculations
should be carried out for the repetitively-pulsed performance of the conical
nozzle operating with argon and hydrogen propellants heated by laser pulse en-
ergies and with laser interpulse times that simulate the experiments. It will
also be extremely valuable to incorporate into the computer code a subroutine
that calculates plasma radiation losses.

REFERENCES FOR SECTION 3

3.1 Rosen, D. I., Kemp, N. H., Weyl, G., Nebolsine, P. E., and Kothandaraman, G., " Final Technical Report - Pulsed Laser Propulsion Studies, Vol. I: Thruster Physics and Performance," PSI TR-184, Physical Sciences Inc. Andover, MA, October, 1982.

3.2 Sutton, G. P., "Rocket Propulsion Systems for Interplanetary Flight," Journal of the Aero/Space Sciences, Vol. 26, No. 10, October 1959, pp. 609-25.

3.3 Sutton, G. P., Rocket Propulsion Elements, John Wiley and Sons, Inc., New York, 1963, 3rd Edition, pp. 26-35.

4. OPTICAL DESIGN CONSIDERATIONS FOR A SELF-FOCUSING NOZZLE

We consider in this section the optical performance of a paraboloidal self-focusing nozzle of utility for laser propulsion. The primary conclusions are:

- The requirement for off-axis performance allows the surface to be of only very modest optical quality.

- For off-axis angles $\gtrsim 10^\circ$, only modest magnifications ($\lesssim 25$) can be anticipated.

- Optimum optical and fluid dynamic performance appear to be mutually exclusive, consequently a compromise is required.

- The impact of off-axis focusing and breakdown on thruster performance and surface erosion should be evaluated.

Details of the analyses are given in the following paragraphs.

4.1 Aberration Characterization

Two general classes of aberrations can be distinguished: deterministic and random. The former are those defects in the image caused by the departure of the actual wavefront from a spherical wave for a mathematically perfect reflective or refractive surface. The latter are caused by departures of the actual surface from the desired mathematical surface which are random because they are associated with manufacturing tolerances. For analysis purposes, it is convenient to consider each type separately because of the difference in their basic character.

4.1.1 Random Aberrations

Consider the simple optical system shown in Fig. 4.1 which consists of a lens of aperture D and focal length Z. The image of a point object at infinity is given by

$$I(\underset{\sim}{x}) = (\lambda z)^{-2} \left| \int d\underset{\sim}{y} w(\underset{\sim}{y}) U(\underset{\sim}{y}) \exp\left[-\frac{2\pi i}{\lambda z} \underset{\sim}{x} \cdot \underset{\sim}{y} \right] \right|^2 , \tag{4.1}$$

where λ is wavelength, $U(\underset{\sim}{y})$ is the complex wave in the aperture plane and $W(\underset{\sim}{y})$ is a simple aperture function ($=1$ inside and 0 outside the aperture). We now
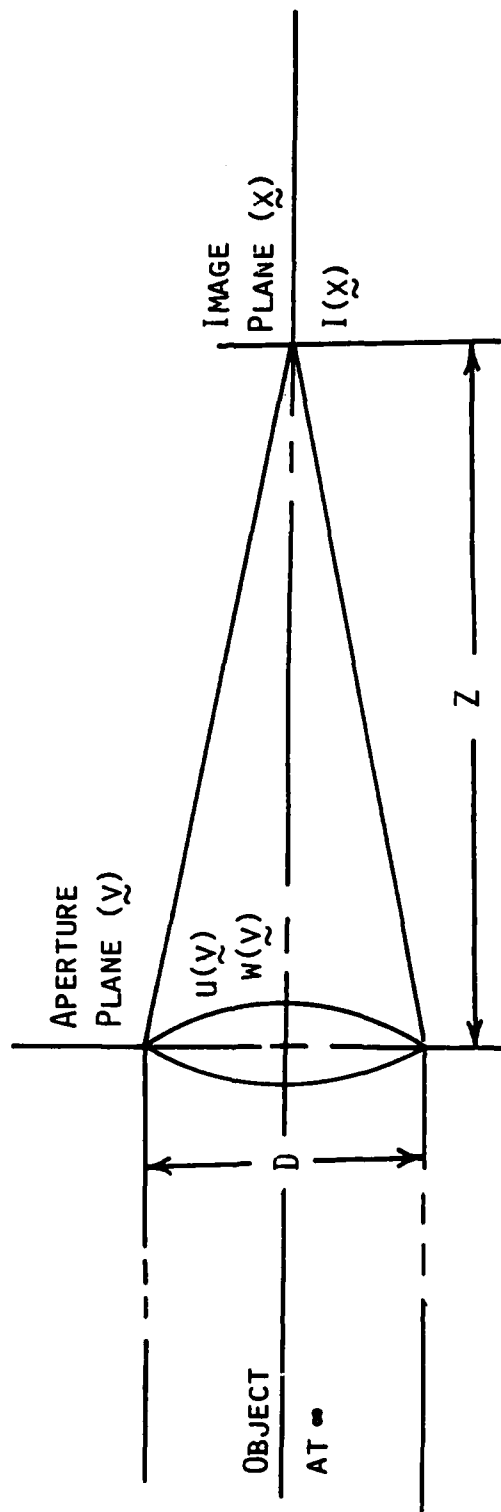
Fig. 4.1 Imaging geometry.

assume that $U(\underset{\sim}{y})$ is characterized by the product of a deterministic portion (constant for a perfect aperture) and a random phase distortion ($= \exp i\phi(\underset{\sim}{y})$). The average image plane intensity can be shown to be equal to

$$\langle I(\underset{\sim}{x})\rangle = \rho(\infty)I_D(\underset{\sim}{x}) + \frac{E}{(\lambda z)^2}\left[1-\rho(\infty)\right]\int d\underset{\sim}{\Delta}\,\tau_D(\underset{\sim}{\Delta})\rho_N(\underset{\sim}{\Delta})e^{\frac{2\pi i}{\lambda z}\underset{\sim}{x}\cdot\underset{\sim}{\Delta}} \qquad (4.2)$$

where $\langle\ldots\rangle$ represents a statistical average, I_D is the deterministic image, and E is the energy collected by the aperture. τ_D is the optical transfer function of the deterministic image (normalized Fourier Transform of I_D) and ρ_D is the correlation function of the random component of the field.

$$\rho(\underset{\sim}{\Delta}) = \langle\exp i[\phi(\underset{\sim}{y}) - \phi(\underset{\sim}{y}-\underset{\sim}{\Delta})]\rangle$$

$$\rho_N(\underset{\sim}{\Delta}) = \left[\frac{\rho(\underset{\sim}{\Delta})-\rho(\infty)}{1-\rho(\infty)}\right] \qquad (4.3)$$

$$\rho(\infty) = \left|\langle\exp i\phi(\underset{\sim}{y})\rangle\right|^2 \equiv \left|\Phi(1)\right|^2,$$

where $\Phi(1)$ is the first order characteristic function of the random variable $\phi(\underset{\sim}{y})$.

In many cases of interest, the correlation function is much narrower than the deterministic transfer function leading to the approximate result.

$$\langle I(x)\rangle = \frac{AE}{(\lambda z)^2}\left\{|\Phi(1)|^2\,P(\underset{\sim}{x}) + \frac{1}{A}\left[1-|\Phi(1)|^2\right]S\left(\frac{\underset{\sim}{x}}{z}\right)\right\} , \qquad (4.4)$$

when $P(\underset{\sim}{x})$ is the normalized point spread function of the deterministic image and S is the spectrum of the random field (Fourier Transform of ρ_N).

From this result, we note that energy is conserved (i.e., integral of $\langle I(x)\rangle$ over $\underset{\sim}{x}$ is equal to E). Furthermore, the energy in each term is given by

$$(E_D/E) = |\Phi(1)|^2 \qquad (4.5)$$

$$(E_R/E) = 1-|\Phi(1)|^2 ,$$

67

where E_D and E_R are the energies of the deterministic (first term of Eq. 4.4) and random (second term of Eq. 4.4) components of the field, respectively. The on-axis intensity is given by:

$$\langle I(\underset{\sim}{\varrho}) \rangle = \frac{AE}{(\lambda z)^2} \left\{ |\Phi(1)|^2 + \left[1-|\Phi(1)|^2\right](\Lambda/D)^2 \right\} \ , \tag{4.6}$$

where Λ is the correlation scale of the random component $\left(\int d\underset{\sim}{\Delta}\rho = \left(\frac{\pi}{4}\right)\Lambda^2 \right)$.

These general characteristics of the image are shown in Fig. 4.2. These results indicate that, in principle, a deterministic image is always present (of size $\lambda z/D$ if unaberrated). However, its energy is attenuated by the presence of the random component of the field. The random component of the field results in an average intensity which appears as though it were generated by a lens of aperture Λ, the correlation scale of the random field.

The characteristic function depends on the type of statistics involved and the rms phase distortion (σ_ϕ). Values for several common cases are shown in Table 4.1. As can be seen, one wave (2π) of random aberration substantially eliminates the deterministic component in all cases. For normal statistics, a quarter and (1/20) wave of aberration results in a 92% and 9% reduction in energy, respectively. Consequently, high quality optical systems are usually specified at ($\lambda/20$) or better.

4.1.2 Deterministic Aberrations

Except for diffraction, the on-axis performance of a mathematical paraboloidal mirror is perfect based on third order aberration theory. For off-axis cases (i.e., direction of object not parallel to axis of rotation) Coma and Astigmatism occur (Spherical Aberration is always zero). The angular diameters of the blur circles associated with these effects are given by:

$$\text{Coma:} \quad \beta_C = \frac{\theta}{16F^2} \tag{4.7}$$

68

$$I(\underline{x})$$
$$I(0) = \frac{AE}{(\lambda z)^2} \left\{ |\Phi(1)|^2 + [1-|\Phi(1)|^2](\frac{A}{D})^2 \right\}$$

$$\frac{AE}{(\lambda z)^2} |\Phi(1)|^2$$

$$\frac{AE}{(\lambda z)^2} [1-|\Phi(1)|^2] \left(\frac{A}{D}\right)^2$$

RANDOM IMAGE

DETERMINISTIC IMAGE

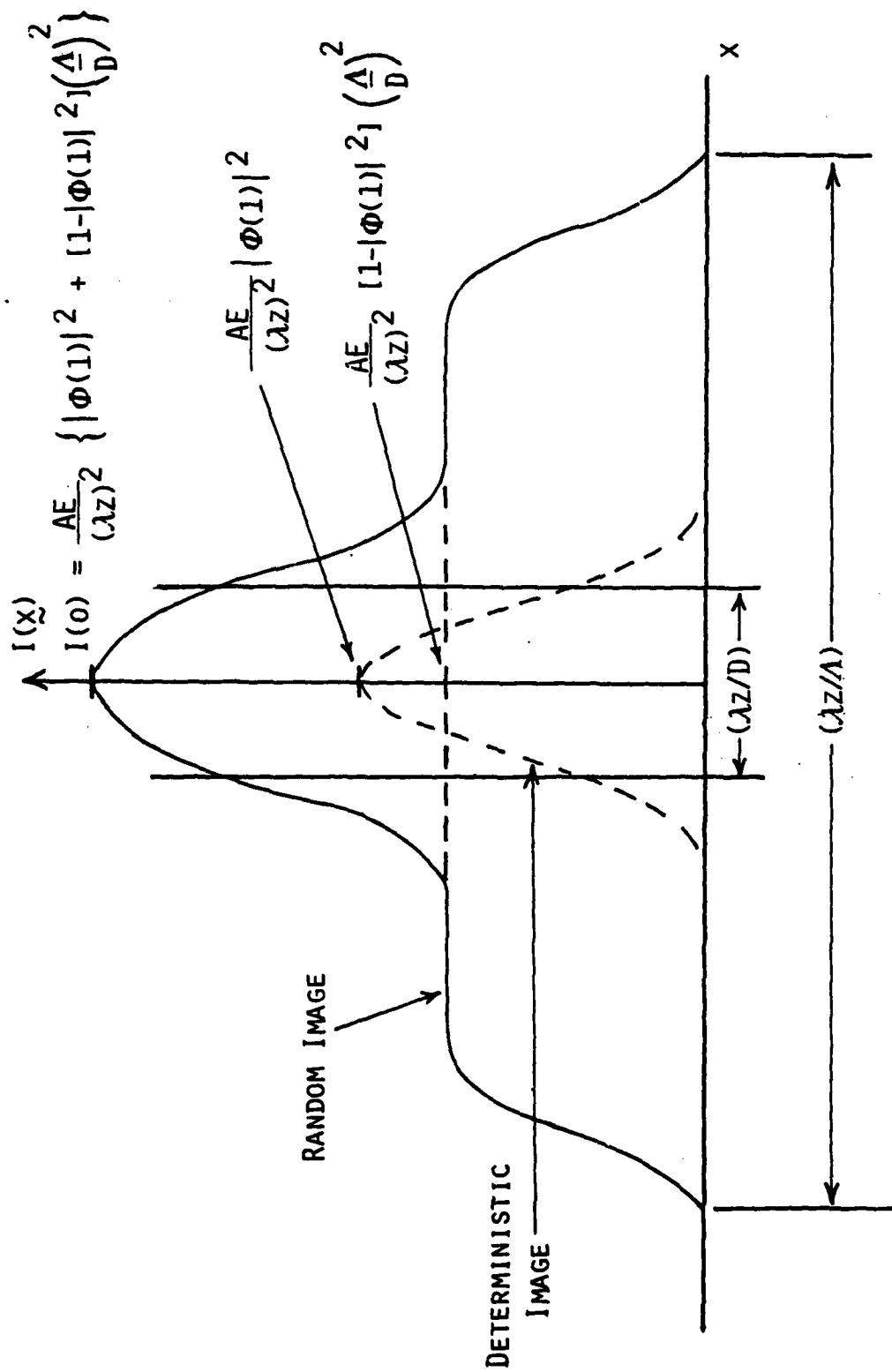$(\lambda z/D)$

$(\lambda z/A)$

X

Fig. 4.2 Image characteristics.

TABLE 4.1 First-order characteristic functions for
various distributions.

Distribution	Characteristic function		
	$\|\Phi(1)\|^2$	Value at σ_ϕ	
		2π	4π
normal	$\exp(-\sigma_\phi^2)$	10^{-17}	10^{-69}
uniform[a]	$\mathrm{sinc}^2[(3)^{1/2}\sigma_\phi]$	8×10^{-3}	10^{-4}
Simpson	$\mathrm{sinc}^4[(3/2)^{1/2}\sigma_\phi]$	2×10^{-4}	2×10^{-7}
exponential	$(1-\sigma_\phi^2)^{-1}$	2×10^{-2}	6×10^{-3}
Laplace	$(1-\sigma_\phi^2/2)^{-2}$	2×10^{-3}	10^{-4}
gamma	$2^{-\sigma_\phi^2}$	10^{-12}	10^{-48}
Rayleigh[b]	$_1F_1^2[1;1/2;-\sigma_\phi^2/(4-\pi)]$ $+[\pi\sigma_\phi^2/(4-\pi)\exp-\sigma_\phi^2/(4-\pi)]$	10^{-15}	10^{-77}

[a] $\mathrm{sinc}\chi \equiv (\sin\chi/\chi)$.

[b] $_1F_1(\alpha; \beta; \pm\lambda) =$ confluent hypergeometric function

$$= \sum_{n=0} (\alpha)_n(\pm\lambda)^n/(\beta)_n n! \text{ where}$$

$$(\alpha)_n=(\alpha+1)\cdots(\alpha+n-1), \ (\alpha)_0=1.$$

Astigmatism: $\beta_A = \dfrac{(L-z)\theta^2}{2z\ F}$,

where θ is the off-axis angle, F is the F-number of the system, z is the distance from the paraboloid apex to the focal point and L is the distance to the aperture stop (see Fig. 4.3).

For the case of interest here, a physical aperture stop is not likely to be used. Consequently L is defined by the physical extent of the mirror or the beam size. In this case, the blur circle diameter due to Astigmatism is given by

$$\beta_A = \frac{\theta^2}{2F}\left(\frac{1}{16F^2} - 1\right) .$$

(4.8)

The expressions given above are reliable for modest apertures or fields, however, they break down at larger values. A very conservative estimate of the resultant blur due to both effects is given by the sum. We will use a root sum square which is perhaps more realistic.

Inspection of the above forms lead to the obvious conclusion that for off-axis performance, a larger F-number is desirable. Paraboloids of various F-number and fixed diameter are shown in Fig. 4.4. As the F/No. increases with a fixed entrance diameter, the paraboloid becomes shallower and the focal point moves farther away from the apex. Above some critical value, the resulting paraboloid will no longer function adequately as a rocket nozzle. The gas flow will separate from the walls and/or the gas expansion rate will not be appropriate. Furthermore, for values in excess of F/0.25, the focal point will lie outside the entrance aperture. Unless some type of mechanical extension is used, this will likely yield an inefficient motor because the thrust will not be vectored within a small enough angle. Consequently, nozzle design should be based on a trade-off between the conflicting requirements for optical vs. fluid dynamic performance.

The parabolic rocket used in laboratory experiments (Fig. 4.5) corresponds to approximately F/0.05. Ray traces for this thruster at $\theta = 0°$ and $15°$ are given in Figs. 4.6 and 4.7, respectively. As can be seen, the beam
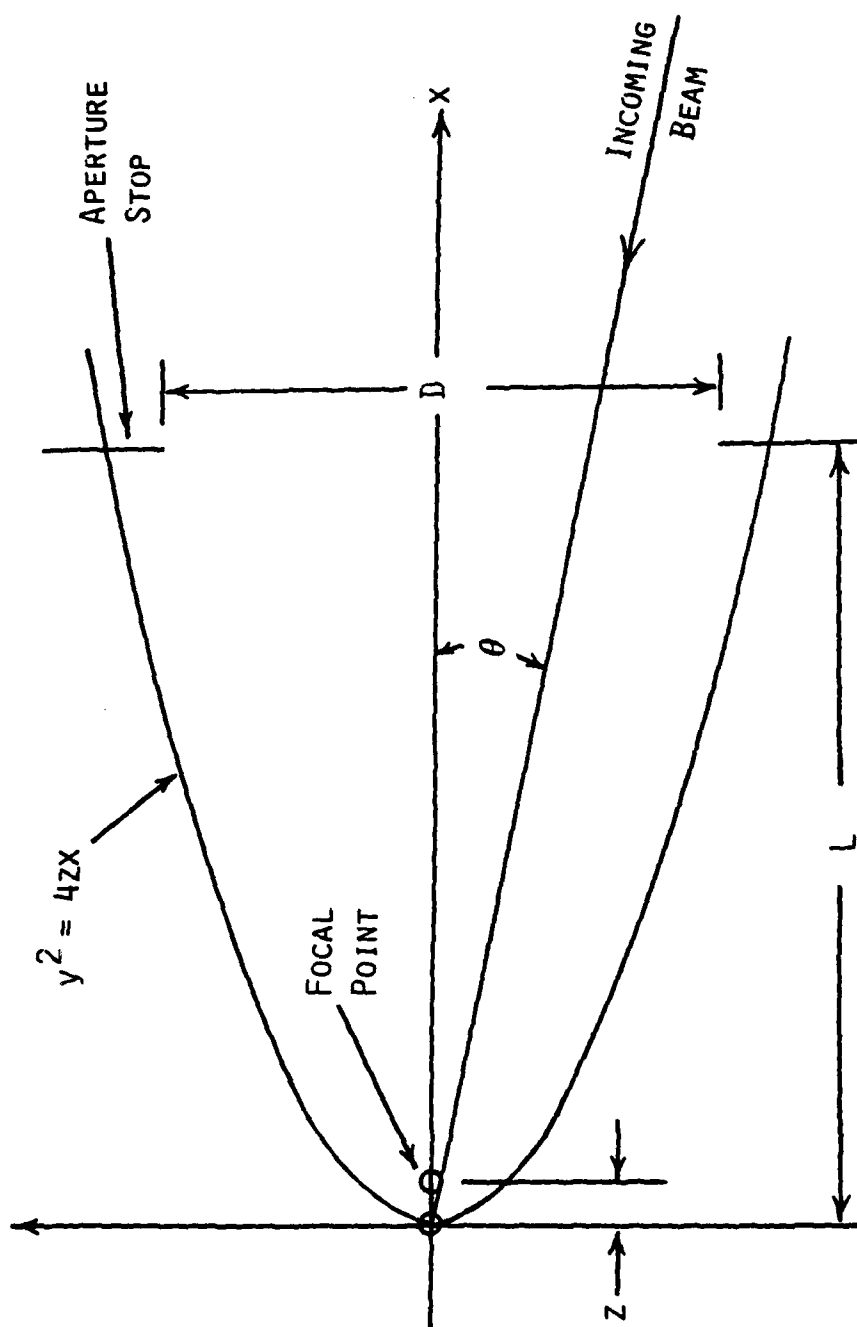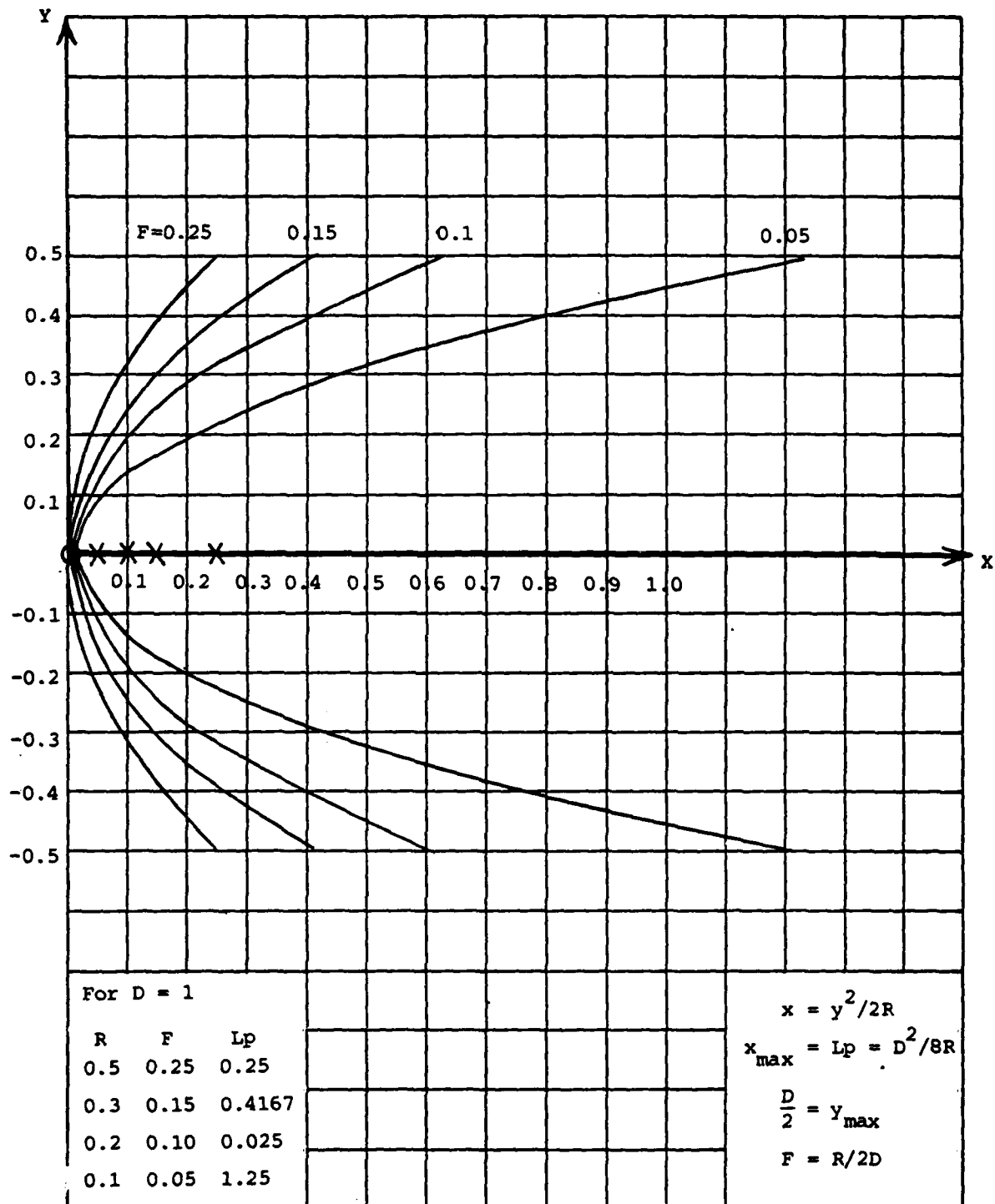
Fig. 4.3 Parabolodial mirror.

APERTURE STOP

INCOMING BEAM

X

D

θ

$y^2 = 4zx$

FOCAL POINT

L

Z

Fig. 4.4 Paraboloids of various F/number and fixed aperture.

For the chart:

F=0.25   0.15   0.1   0.05

For D = 1

R	F	Lp
0.5	0.25	0.25
0.3	0.15	0.4167
0.2	0.10	0.025
0.1	0.05	1.25

$x = y^2/2R$

$x_{max} = Lp = D^2/8R$

$\frac{D}{2} = Y_{max}$

$F = R/2D$

73
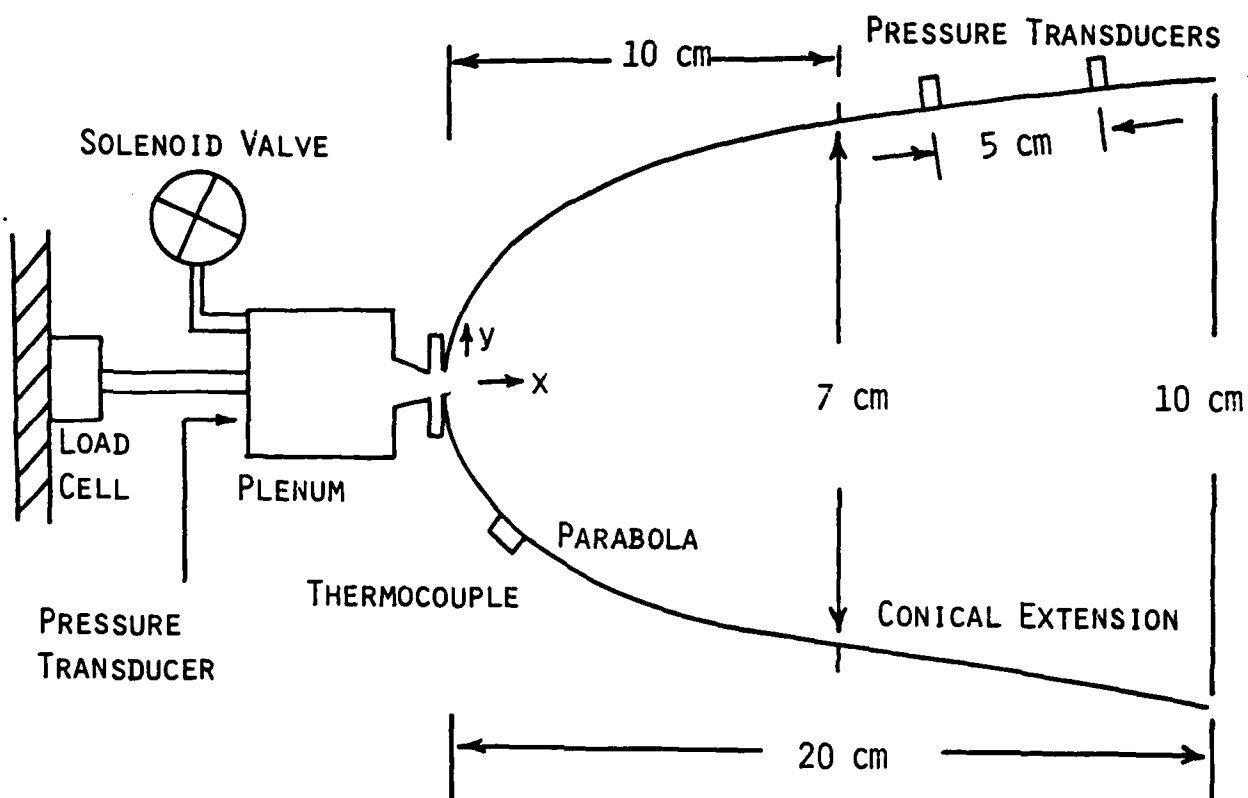
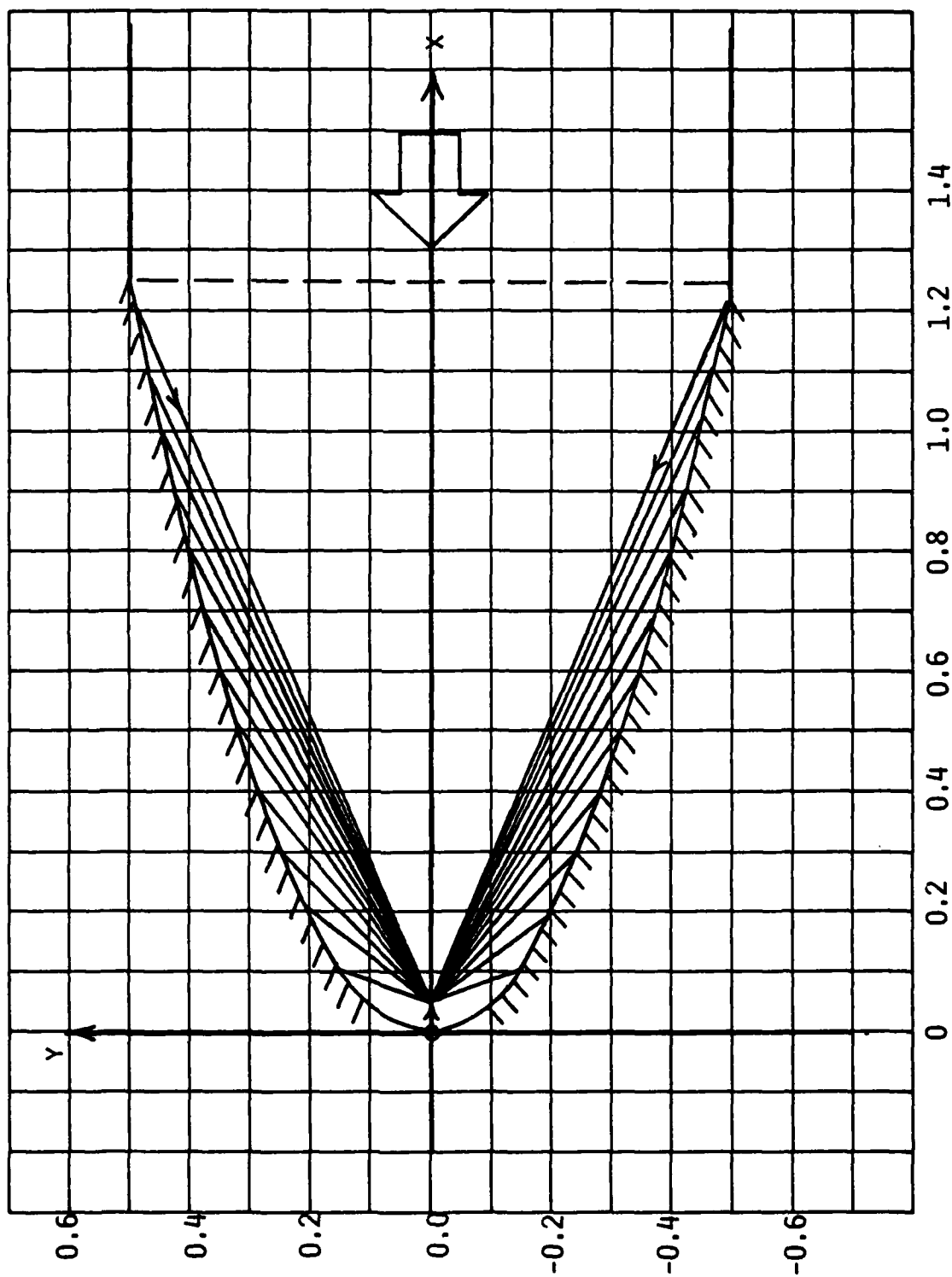Fig. 4.5   Parabolic rocket configuration used in laboratory experiment.

Fig. 4.6 Ray trace for F/0.05 paraboloid with θ = 0°.
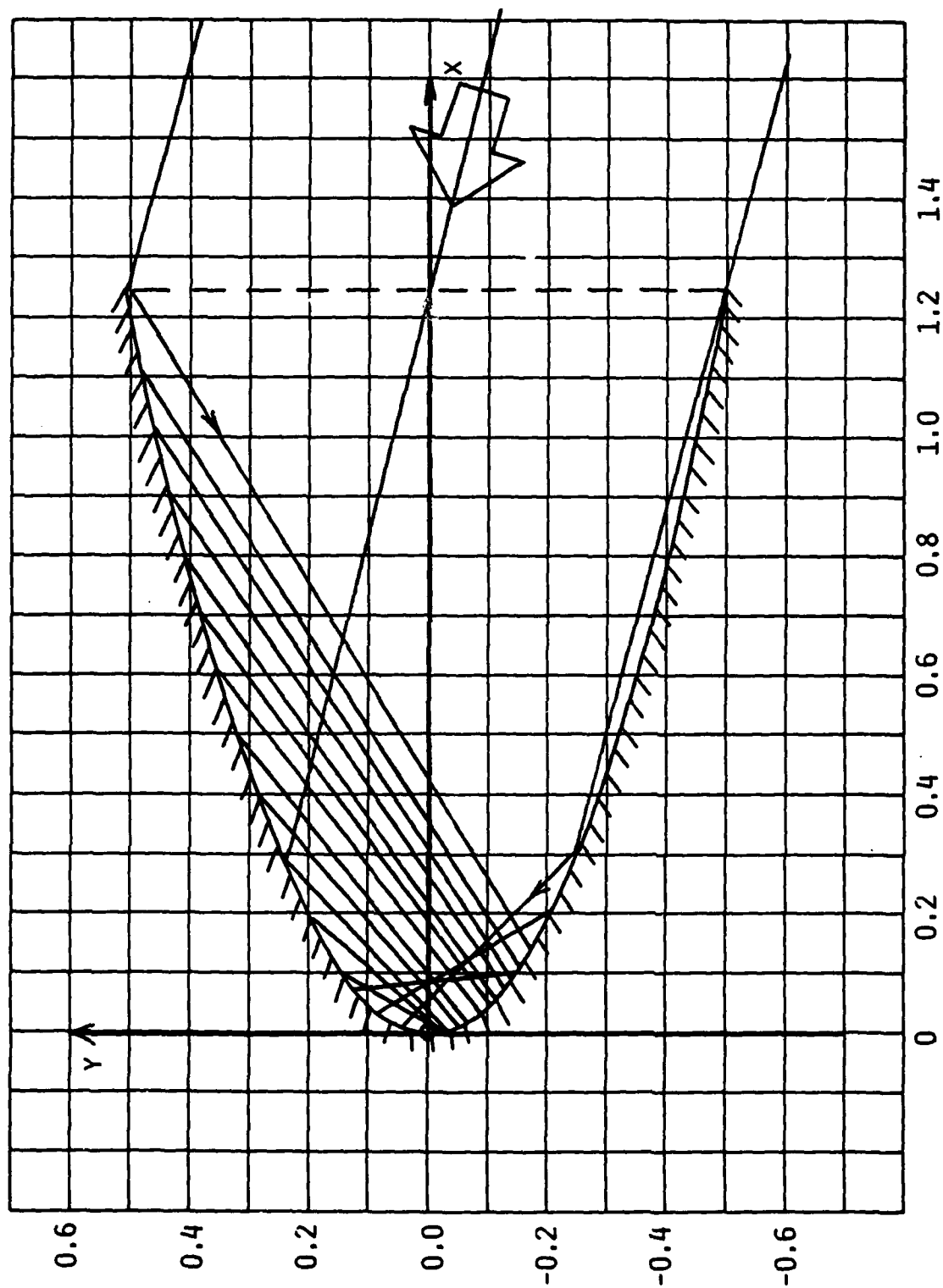
Fig. 4.7 Ray trace for F/0.05 paraboloid with $\theta = 15^\circ$.

does not focus to any great degree at $\theta = 15^\circ$. Ray traces for an F/0.1 system are shown in Fig. 4.8.

An approximate upper limit to off-axis performance can be obtained by the ad-hoc criterion that the aberrated beam (rhs of Eq. 4.7 and 4.8 converted to spatial size) must be smaller than the physical dimension of the parabola, i.e.,

$$\left\{\left[\frac{\theta}{16F^2}\right]^2 + \left[\frac{\theta^2}{2F}\left(\frac{1}{16F^2} - 1\right)\right]^2\right\}^{1/2} < 4 \quad . \tag{4.9}$$

The limiting angle defined by this expression is given in Fig. 4.9 as a function of F-number. The magnification associated with this spot size is also given in Fig. 4.9.

The results of Fig. 4.9 indicate that for low F-number systems (< 0.1), the laser beam will not focus for off-axis angles greater than a few degrees. Optical performance at larger angles can only be determined by a detailed ray trace which considers multiple reflections or via experiment. Restricting the system to small angles has significant implications in terms of overall mission configurations.
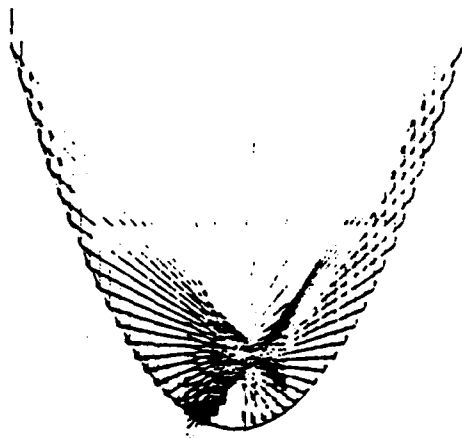
4.2   Discussion

The analysis given in the prior section indicates that because of fluid-dynamic considerations, a low F/No paraboloid will be required. This will result in relatively large off-axis deterministic aberrations which will produce a large focal spot size at any angle above a very modest value. This, in turn, reduces the magnification dramatically. Consequently, any detailed system study should include the requirement that the energy density of the input laser beam be within roughly a factor of (10-25) of that required for propellant breakdown.
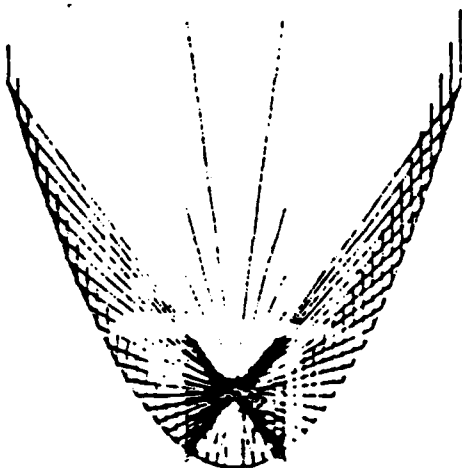
When coupled with a maximum off-axis angle of 10° or less, these two requirements would seem to be rather restrictive in terms of mission configurations. Obviously, these requirements can be relaxed by implementing a larger F-number system. As mentioned previously, this has an effect on performance as a thruster.

77

INCIDENT BEAM 0 deg OFF-AXIS

INCIDENT BEAM 2.5 deg OFF-AXIS

INCIDENT BEAM 5 deg OFF-AXIS

f/NUMBER = 0.10

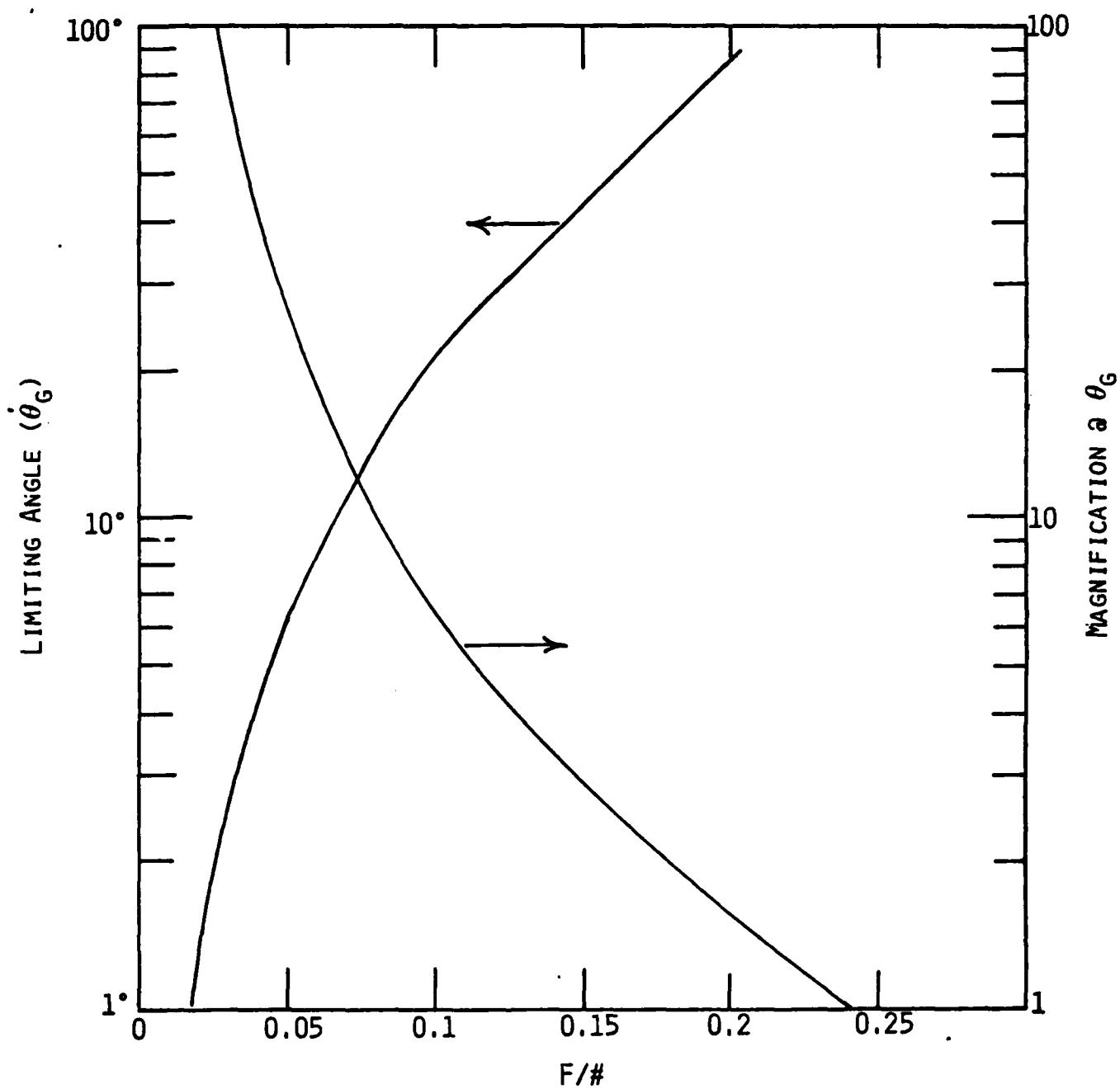Fig. 4.8   Off-axis behavior of a parabolic mirror.

Fig. 4.9 Limiting off axis angle and corresponding magnification for various F/# paraboloids.

To establish a complete map of allowed operational parameters will require a determination of the limiting F-number imposed by the fluid dynamics.

While the large spot size implied by off-axis performance limits the achievable magnification, there is one advantage in terms of optical quality. Referring to Fig. 4.3, we see that the random image size is given approximately by $(\lambda z/\Lambda)$ where Λ is the correlation scale of the surface. Provided this dimension is smaller than the spot size associated with the deterministic off-axis performance, there is no reason to require a high optical surface quality corresponding to a substantial fraction of energy in the diffraction image $(\lambda/10$ or better). Data from one vendor of paraboloidal mirrors suggests that this scale is of order 0.1 mm which is consistent with other data relative to surface (non-optical) finishes. For a one meter, F/0.05 thruster, this value yields a random image size of less than 1 mm at a wavelength of 0.35 μ which is much smaller than the 20 cm nozzle size at nominal focus (for a one meter aperture). Consequently, several waves of random aberration could be tolerated without serious impact on performance. To determine the actual amount allowed would require an alternate analysis which takes into account surface slope (i.e., σ_ϕ/Λ), and shadowing effects which can become important for low incidence angles on a surface with steep slopes. The analysis of Section 4.1 does not adequately account for these effects, i.e., it is appropriate for a moderately good surface. This alternate analysis is available in several standard texts but it is probably not necessary to pursue this issue in detail.

One effect which has not been evaluated is the impact of off-axis focusing and breakdown on thruster performance. As the beam moves off-axis, the focal point also moves off-axis. This may be important. However, as indicated in the prior results, the beam quickly becomes large and so it may not be appropriate to conceptualize the situation in terms of breakdown occurring at a small point which is located at a substantial distance from the axis.

A related issue is surface erosion which may occur as the focus and breakdown region moves close to the walls. Again, however, it is probably inappropriate to consider the problem in this fashion. Rather a more conservative approach would be to determine the effect on the surface when the breakdown occurs in a large volume which has a dimension of order of the nozzle in

the vicinity of nominal focus. It seems reasonable that this assumption would lead to a reasonable estimate of surface erosion effects.

In summary, it appears that the allowed off-axis angle is significantly limited by the low F-numbers which probably are required for suitable fluid dynamic performance. This has the further effect of yielding large spot sizes which limit the achievable magnification. This does have benefit in that only very modest optical surface quality is required. To establish a complete map of allowed operational conditions will require the evaluation of the maximum allowed F-number which is controlled by the fluid mechanics. Off-axis focusing could be a problem, and a conservative approach to evaluating surface erosion would be to assume that breakdown occurs in a volume with dimension of order of the nozzle size in the vicinity of nominal focus. It should be noted that these conclusions are based on a rather simple analysis. Depending on the input beam profile, adequate energy densities which will lead to gas breakdown may exist in a small region even for large angles and nominal spot sizes. This effect could be significant and hence, a detailed ray trace which includes beam profiles should be implemented to provide a complete assessment of these issues.